PROBING CHANGES IN THE SOLID ELECTROLYTE INTERPHASE IN LI-ION CELLS

by

Alison S. Keefe

Submitted in partial fulfilment of the requirements
for the degree of Master of Applied Science

at

Dalhousie University
Halifax, Nova Scotia
December 2019

Table of Contents

List of Tables

List of Figures

Abstract

In Li-ion cells, a passivating film called the solid electrolyte interphase (SEI) develops at the interface between the electrolyte and the electrode particles. The SEI is essential to the functionality of the cell, but the SEI can also have detrimental effects on the cell. The SEI impacts the internal cell impedance and capacity retention over the lifetime of the cell. Despite being a vital part of Li-ion cells, the properties of the SEI are not well known or understood. This thesis studies several properties of the SEI through a variety of techniques. Cells containing different electrolyte additives were studied using electrochemical impedance spectroscopy (EIS) and X-ray photoelectron spectroscopy (XPS) after formation and after long-term cycling. Positive and negative electrodes were examined separately to study the SEI at each electrode. EIS measurements were taken versus temperature, and activation energies (E_a) related to Li+ transport through the SEI were calculated. E_a values for the negative electrode SEI varied depending on the choice of electrolyte additive, but values did not vary substantially for the positive electrode SEI. After cycling, the E_a differed depending on electrolyte additive, electrode type, and voltage limits. Charge transfer resistance was also compared after formation and cycling and did not always correlate with E_a trends, suggesting that multiple factors influence SEI properties. XPS was used to study the chemical composition and thickness of the SEI. Electrolyte additives affected the quantity of inorganic materials in the SEI, and more inorganic material appears to correlate with lower E_a values. Cells containing lithium difluorophosphate electrolyte additive had the best lifetime of the cells studied in this work. These cells also showed the lowest SEI activation energy values, lowest charge transfer resistance, and most inorganic SEI composition after cycling.

List of Abbreviations and Symbols Used

A	proportionality constant in Arrhenius equation
A	surface area of active material in capacitance equation
AC	alternating current
AG	artificial graphite
BE	binding energy
BMF	polypropylene blown microfiber
c	cycles
C	capacitance
C_{dl}	double layer capacitance
C_f	Faradaic capacitance
CCCV	constant current constant voltage
CMC	carboxymethyl cellulose
CPE	constant phase element
CPS	counts per second
DMC	dimethyl carbonate
e^-	electron
E_a	activation energy
E_v	vacuum energy of XPS sample
EC	ethylene carbonate
EIS	electrochemical impedance spectroscopy
f	frequency (Hz)
$h\upsilon$	X-ray energy
$i(\omega,t)$	frequency- and time-dependent current
I	current amplitude
IRC	irreversible capacity
j	$\sqrt{-1}$
k_B	Boltzmann constant
KE	kinetic energy
L	inductance
LFO	lithium difluorophosphate
NMC	$Li(Ni_{1-x-y}Mn_xCo_y)O_2$
OCV	open circuit voltage
PVDF	polyvinylidene fluoride
Q	cell capacity (mAh)
R	resistance
$R_{contact}$	contact resistance
R_{ct}	charge transfer resistance
R_{el}	electronic resistance
R_f	Faradaic resistance
R_{ion}	ionic resistance in pores
R_s	solution/series resistance
RC	resistor in parallel with capacitor

R-CPE	resistor in parallel with CPE
SEI	solid electrolyte interphase
SBR	styrene-butadiene rubber
SOC	state of charge
t	time
T	temperature
TM	transition metal
TOC	top of charge
UHV	ultra-high vacuum
$v(\omega,t)$	frequency- and time-dependent voltage
V	voltage amplitude
VB	valance band
VC	vinylene carbonate
W	Warburg circuit element
XPS	X-ray photoelectron spectroscopy
Z	impedance
ε	dielectric constant of SEI
ε_0	permittivity of free space
θ	phase difference
σ	Warburg coefficient
ϕ	constant phase exponent of CPE
ϕ_{sp}	work function of XPS analyzer
ω	angular frequency (rad/s)
(-/-)	negative symmetric cell
(+/+)	positive symmetric cell
(+/-)	full coin cell

Acknowledgements

I am very grateful for the support and guidance I have received throughout this master's degree. Firstly, I would like to thank my supervisor, Jeff Dahn, for his dedication and enthusiasm towards this important research. I have learned a great deal working in the Dahn lab and really appreciate the help and direction I have received from him with this project. I would also like to thank everyone in the Dahn lab for being so willing to help or discuss topics at a moment's notice. It has been a true pleasure working with this excellent group of people.

Special thanks go to Rochelle Weber for running many hours of XPS experiments for this project. Thanks also to Michel Johnson for helping set up the new automatic temperature controller and to Novonix for providing support and parts for this upgrade. Also, thanks to Novonix for fixing the temperature box that I broke several times.

Lastly, I would like to thank my friends and family for their love and support throughout my degree. Thanks especially for taking care of me when I was broken and could not walk.

Chapter 1: Introduction

1.1   Motivation and Scope

Lithium ion (Li-ion) batteries are widely used in a variety of products including portable electronics, medical devices, and power tools. These batteries are increasingly being used in electric vehicles and grid level energy storage. While different applications prioritize different battery specifications, the battery industry is constantly aiming to improve the lifetime, energy density, safety, and cost of Li-ion batteries.

Li-ion batteries experience capacity fade over their lifetime. Capacity fade is sometimes linked to impedance growth within the cell.[1–5] One main factor that contributes to cell impedance is the formation of the solid electrolyte interphase (SEI), a passivating film that forms at the interface between electrodes and the electrolyte.[5–7] The SEI is formed upon the initial charge ("formation") of the cell, consuming lithium and other materials in irreversible reactions. Further changes to the SEI occur during cycling and are associated with impedance growth and capacity fade.[3,8–10]

Figure 1.1 shows normalized capacity vs. cycle number for cells with three different electrolyte systems containing different additives. Figure 1.1 shows that electrolyte additives have a significant impact on capacity retention as the cell with control electrolyte loses capacity far more quickly than cells with added vinylene carbonate (VC) or lithium difluorophosphate (LFO). This correlation of capacity fade with the use of different electrolyte additives has been studied widely in the literature.[11–16] It is believed that this impact on cell capacity is due to additives affecting the composition and properties of the SEI.[6,17–20]
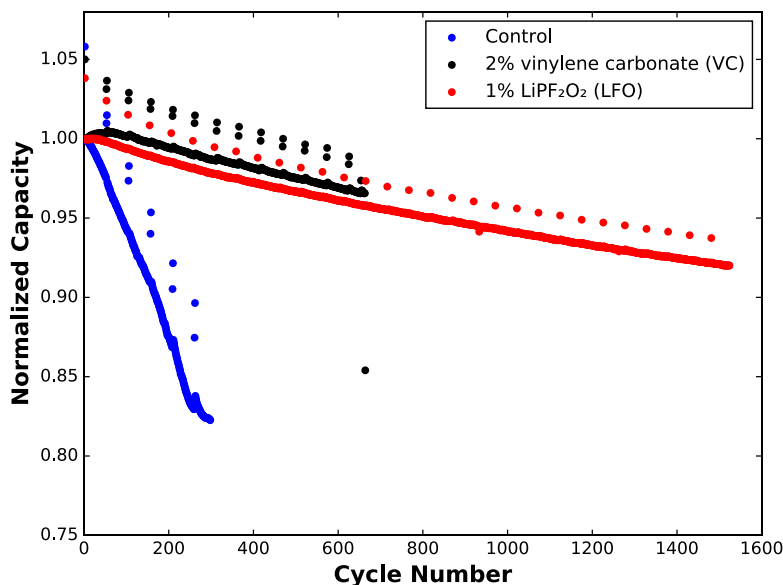
Figure 1.1: Normalized capacity vs. cycle number for Li-ion cells with Li(Ni$_{0.5}$Mn$_{0.3}$Co$_{0.2}$)/ artificial graphite electrodes cycled from 3.0 V to 4.3 V at C/3 and 40°C. Three cells are shown which contain a control electrolyte, control electrolyte with 2% vinylene carbonate additive (VC), and control electrolyte with 1% lithium difluorophosphate (LiPF$_2$O$_2$) additive. Data courtesy of Xiaowei Ma, Lin Ma, and Jamie Stark, Dalhousie University.

This thesis attempts to investigate the properties of the SEI in Li-ion cells containing different electrolyte additives. This is accomplished by means of impedance measurements, measurements of SEI composition, and charge-discharge cycling experiments. The remainder of this chapter will provide a brief introduction to Li-ion batteries, discuss the choice of electrolyte additives used in this thesis, and consider the SEI in more detail. Chapter 2 will detail the experimental methods used in these studies with a focus on the use of symmetric cells, electrochemical impedance spectroscopy (EIS), and x-ray photoelectron spectroscopy (XPS). Chapters 3, 4, and 5 show the main results of this thesis. Chapter 3 deals with the interpretation and validity of EIS results. Chapter 4 uses temperature dependent EIS studies and XPS measurements to study the SEI in cells after formation and after long term cycling. The capacity retention, impedance, and SEI

composition are studied in cells using different electrolyte additives. Chapter 5 shows the results of a study where positive symmetric cells were cycled, and impedance measured periodically. Chapter 6 presents the conclusions of the work in this thesis.

Portions of Chapters 2, 3, and 4 have been published in a peer-reviewed journal article: A. S. Keefe, Samuel Buteau, I. G. Hill, and J. R. Dahn, Temperature Dependent EIS Studies Separating Charge Transfer Impedance from Contact Impedance in Lithium-Ion Symmetric Cells, J. Electrochem. Soc., 166 (14) A3272-A3279 (2019). doi: 10.1149/2.0541914jes. Permission to reproduce this work has been granted and the documentation can be found in Appendix A.

1.2   Li-ion Batteries

Batteries are electrochemical devices that convert chemical energy into electrical energy. This conversion of energy happens through oxidation and reduction reactions (redox) in the active materials of the batteries. Li-ion batteries are a type of rechargeable (secondary) battery which allow for thousands of charge-discharge cycles through the repeated reversal of the highly reversible redox reactions based on intercalation of lithium. The electrochemical unit in which these reactions occur is called a Li-ion "cell", while a Li-ion battery is made of one or more cells connected in series or in parallel.

This section will cover some of the basics of Li-ion cells with a focus on aspects pertinent to the understanding of this thesis. Basic cell operation, materials used in this work, and a description of the SEI are presented here. More complete descriptions of Li-ion battery materials and operation can be found in a variety of sources including Dahn et al.,[6] Whittingham,[21] and Xu.[19]

1.2.1 Li-ion Cell

A Li-ion cell is made of three main parts: a negative electrode, a positive electrode, and an electrolyte, which are enclosed in a sealed container. There are a wide variety of electrode and electrolyte materials used in Li-ion cells, and the choice of these materials dictates the performance of the cell. Figure 1.2 shows the main components of a Li-ion cell and the movement of electrical and ionic charge during a cell charge cycle. The electrodes are often made of active materials that have a layered structure to allow for Li^+ intercalation. The negative electrode in a typical Li-ion cell consists of graphite adhered to a copper current collector and the positive electrode consists of a lithium transition metal oxide or phosphate adhered to an aluminum current collector. The electrodes are separated by a separator material, which allows Li^+ movement through its pores while preventing electrical contact, and the cell is filled with a liquid electrolyte that conducts Li^+. The electrodes are externally connected for charge and discharge of the cell. During cell charge, electrons move through the external circuit due to an externally supplied current, forcing the Li^+ in the cell to leave the positive electrode and intercalate into the negative electrode (arrows shown in Figure 1.2). During a cell discharge cycle, Li^+ and electrons both move in the opposite direction to that shown in Figure 1.2, providing current to power a connected electronic device.
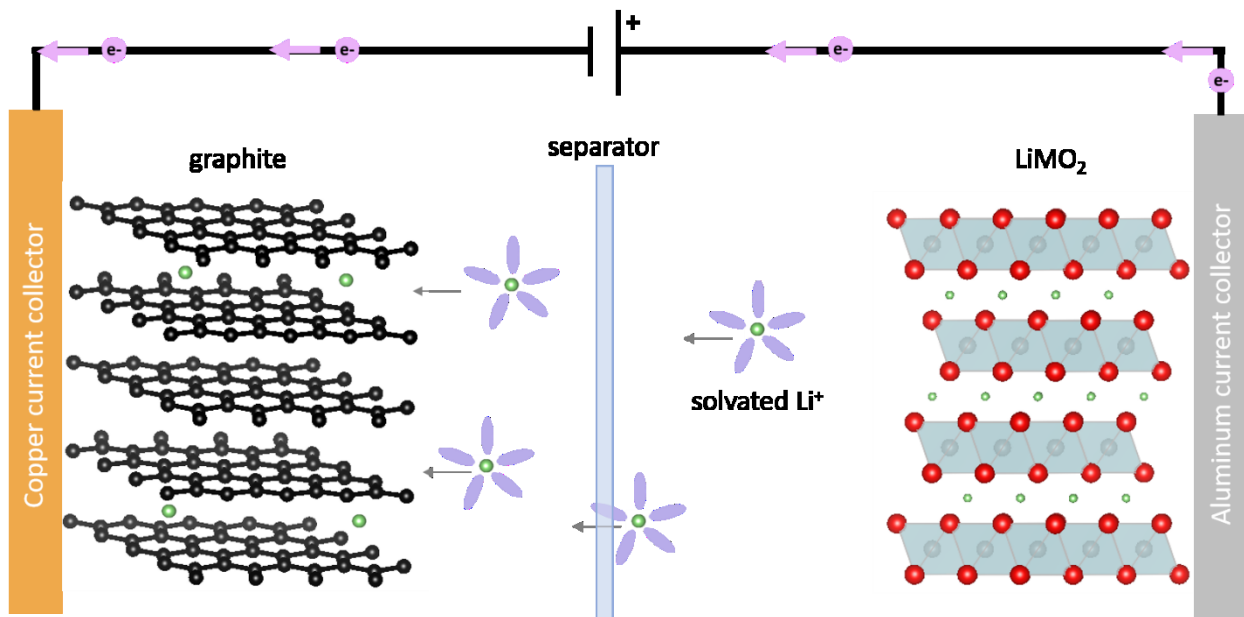
Figure 1.2: Schematic of Li-ion cell with a negative electrode made of graphite on a copper current collector and a positive electrode consisting of a lithium transition metal oxide on an aluminum current collector. Lithium ion (Li^+) and electron (e^-) movement are shown for the cell during charge.

1.2.2 Electrodes

Li-ion cells can contain a variety of active materials as electrode materials. These materials require the ability to reversibly intercalate Li^+ into their lattice structure, and therefore usually have either a layered or tunnel crystal structure. Typical Li-ion cells use a lithium transition metal oxide ($LiMO_2$) material for the positive electrode and graphite for the negative electrode. Many positive and negative electrode materials and their characteristics are described in detail in other works.[6,21,22] Only the materials used in this thesis are described here.

The positive electrodes used in this thesis consisted of single crystal $Li[Ni_{0.5}Mn_{0.3}Co_{0.2}]O_2$ (NMC532) with a TiO_2 coating as the active material (94 wt%) with polyvinylidene fluoride (PVDF) binder (2 wt%) and carbon black (2 wt%) and graphite (2 wt%) conductive additives.

Single crystal NMC532 materials are stable at high temperatures and high voltages and have good capacity retention, as described by Li et al.[23] and Harlow et al.[24] Figure 1.3 shows the O3 crystal structure of fully lithiated $Li[Ni_{1-x-y}Mn_xCo_y]O_2$. The structure contains transition metals—Ni, Mn, and Co in the case of NMC—surrounded by oxygen atoms and arranged in layers. Lithium ions reside in between these layers in the lithiated (discharged) state and deintercalate upon charge of the cell. The following reaction takes place in the positive electrode active material during charge:

$$Li[Ni_{0.5}Mn_{0.3}Co_{0.2}]O_2 \rightarrow Li_{1-x}[Ni_{0.5}Mn_{0.3}Co_{0.2}]O_2 + xLi^+ + xe^- \qquad (1.1)$$
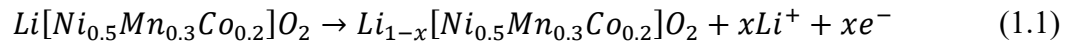
During this reaction, Li^+ is solvated by the liquid electrolyte and is free to move through the electrolyte to the negative electrode. The electrons generated through Equation 1.1 move through the electrode material and the external circuit.
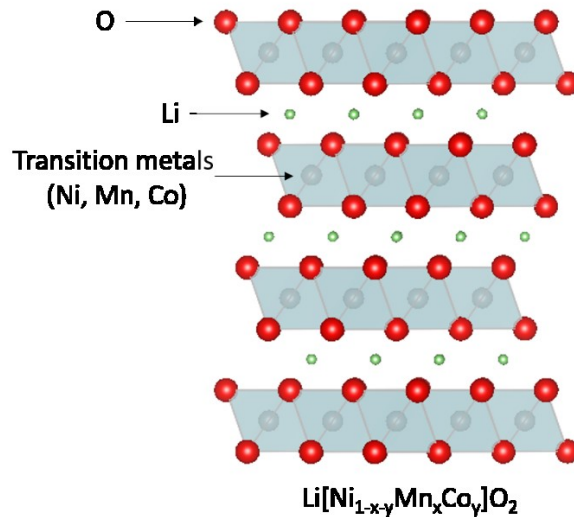
Figure 1.3: Crystal structure of $Li[Ni_{1-x-y}Mn_xCo_y]O_2$ in its fully lithiated state ([110] direction).

The electronic conductivity of NMC materials has been studied by Amin and Chiang,[25] and Seid et al.[26] who report semiconducting electronic conductivity values in the $\sim 10^{-7}$ S/cm to $\sim 10^{-2}$ S/cm range depending on temperature, lithiation state, and the composition of transition metals in the NMC material. Ionic conductivities of NMC materials were also reported by Amin and Chiang,[25] with values in the $\sim 10^{-9}$ S/cm to $\sim 10^{-8}$ S/cm range. Both electronic and ionic conductivities increase with decreasing lithium content.[25] Since the ionic conductivity is at least an order of magnitude lower than electronic conductivity, the authors note that chemical diffusion in the NMC materials is limited by Li^+ transport, and not by electronic conductivity.

The negative electrodes used in this thesis consisted of artificial graphite (AG) active material (95.4 wt%) with carboxymethyl cellulose (CMC) and styrene-butadiene rubber (SBR) binder materials as well as carbon black (2 wt%) conductive additive. Figure 1.4 shows the crystal structure of graphite in its delithiated (a-b) and lithiated (LiC_6) (c-d) states. The layers in graphite have a hexagonal close packed structure with ABAB stacking in the delithiated state, as seen in (b). Upon lithiation of the graphite (charging of the cell), graphite layers rearrange to accommodate the Li^+ and the layers line up in an AAAA structure, as seen in (d).
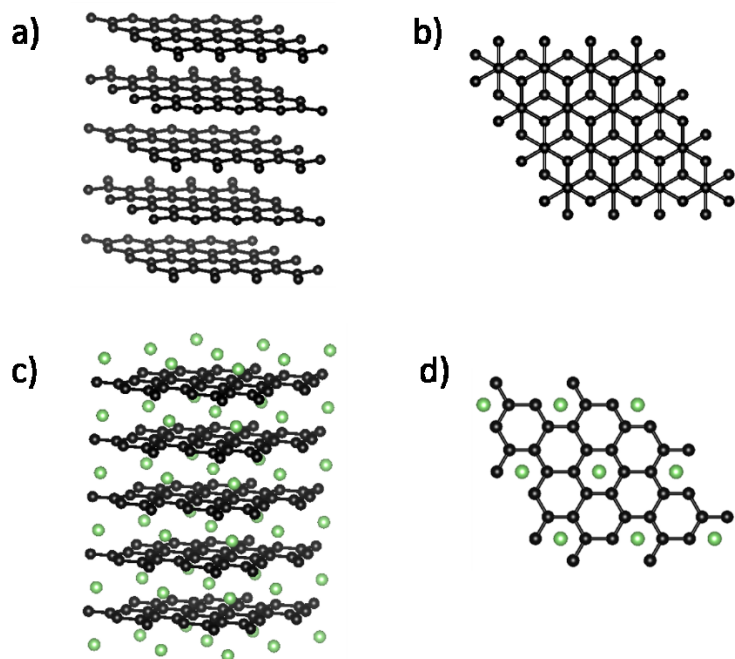
Figure 1.4: (a-b) Crystal structure of graphite. (c-d) Crystal structure of lithiated graphite, LiC$_6$. Figures (b) and (d) show the structures in the [001] direction to show layer stacking more clearly.

During charging of the cell, the graphite electrode reacts following the equation below:

$$xLi^+ + xe^- + C_6 \rightarrow Li_xC_6 \tag{1.2}$$

Equation 1.2 shows that, during cell charging, Li$^+$ (from the electrolyte) combines with electrons (from the external circuit) in the graphite active material (C$_6$) to form lithiated graphite (Li$_x$C$_6$).

These electrode materials are common in Li-ion cells due to a number of characteristics, including their specific capacity, voltage range, and lifetime. The theoretical specific capacity of graphite is 372 mAh/g,[6] while the specific capacity of single crystal NMC532 is between 3.0 V and 4.4 V.[23] The electrodes allow for high voltage cells since graphite has a low average voltage (vs. Li/Li$^+$) and NMC532 is stable up to high voltages (vs. Li/Li$^+$). For example, during a cell charge, AG can

8

go to 0.07 V vs. Li/Li$^+$ while NMC532 goes to 4.47 V vs. Li/Li$^+$ giving an overall cell voltage of 4.4 V. NMC532/AG cells can be cycled with excellent capacity retention for very long periods of time, as demonstrated by Harlow et al.[24]

1.2.3   Electrolytes

The electrolyte is a key part of the cell that allows for the transfer of charge within the cell through Li$^+$ conduction. Some features of a good electrolyte include: high ionic conductivity; good electronic insulation; stability in the electrochemical window of the cell; ability to operate in a wide range of temperatures; and compatibility with the electrode materials.

Li-ion cells can operate using many types of electrolytes; however, only the nonaqueous liquid electrolytes used in this work will be discussed. The liquid electrolytes used in this thesis consist of a lithium salt dissolved in organic solvents with different additives to enhance cell performance. A wide variety of solvents and additives have been studied, and comprehensive reviews of the evolving work on electrolytes for Li-ion cells have been written by Kang Xu.[19,27]

Three electrolyte compositions were used in the main body of this work. The first electrolyte, used as "control" in these studies, consisted of lithium hexafluorophosphate salt (LiPF$_6$) dissolved in an ethylene carbonate (EC) and dimethyl carbonate (DMC) solvent blend. Figure 1.5 shows the chemical structure of these three components of the control electrolyte. The other two electrolytes contained the same control electrolyte mix with the addition of either vinylene carbonate (VC) or lithium difluorophosphate (LFO). Figure 1.6 shows the chemical structure of the VC and LFO electrolyte additives.
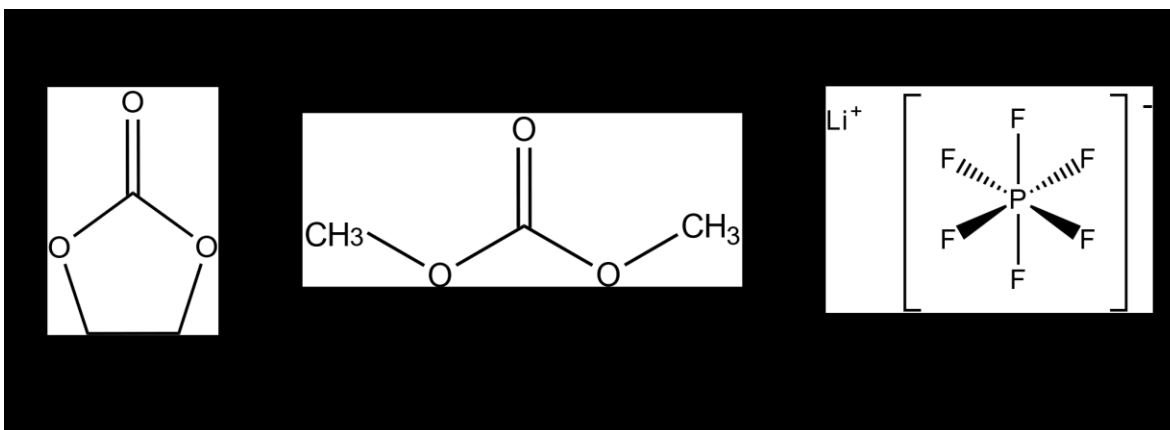
Figure 1.5: Chemical structure of components of the electrolytes used in this work. The solvents ethylene carbonate (EC) and dimethyl carbonate (DMC) are shown in (a) and (b), while (c) shows the structure of $LiPF_6$ salt.
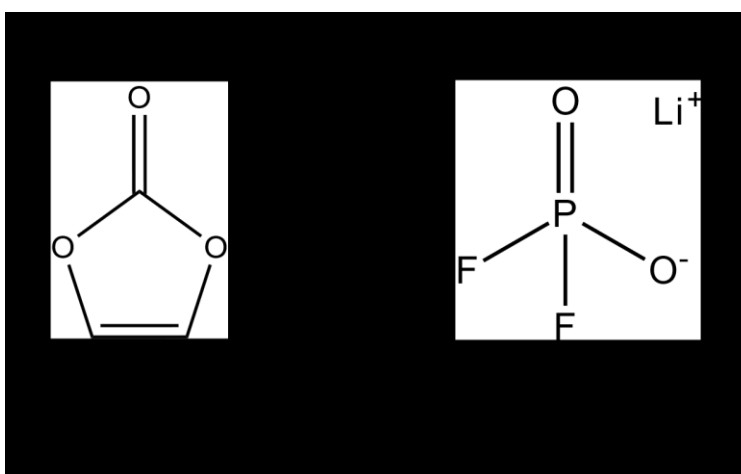
Figure 1.6: Chemical structure of electrolyte additives (a) vinylene carbonate (VC), and (b) lithium difluorophosphate (LFO).

These two additives (VC and LFO) were chosen for this study for several reasons. As demonstrated in Figure 1.1, cells containing these additives demonstrate good capacity retention over many cycles. VC is often used alone or in combination with other electrolyte additives to improve the lifetime and reduce impedance in Li-ion cells.[24,28–30] Burns et al.[31] studied different concentrations of VC additive and showed that it provides cycle life benefits and reduces cell impedance up to a

concentration of ~2%. Aurbach et al.[32] also demonstrated that VC reduces irreversible capacity loss and improves SEI stability on the negative electrode. The authors proposed that flexible polymeric species create part of the SEI when VC is present, enhancing SEI properties.[32] The reduction of VC to form a more beneficial SEI has been studied by other groups since this proposition.[10,33–35]

Ma et al.[36] have shown that LFO is another excellent electrolyte additive for NMC532/graphite cells. Similarly to VC, LFO also improves cycle life, decreases impedance, and suppresses parasitic reactions in the cell.[36] The effects of LFO on the SEI have been studied by Qian et al.[35] who suggest that this additive also promotes the formation of a good quality SEI.

1.2.4   Separator

The separator in a Li-ion cell is a microporous material that separates the positive and negative electrodes. It has the function of providing electronic insulation between the electrodes while also allowing for easy movement of Li^+ through its pores. The separator material must allow for operation over a wide temperature range and not react with the electrodes or electrolyte. Typically, separators in Li-ion cells are made from polyethylene or polypropylene materials.

1.2.5   Solid Electrolyte Interphase (SEI)

First proposed by Peled in 1979,[37] the SEI is a passivating film that forms at the interface between the electrolyte and electrode active material in Li-ion cells. In typical Li-ion cells, the electrolytes used are not electrochemically stable at the potential of the negative electrode.[19,38] Thus, at the negative electrode, electrolyte solvents and salts undergo reduction reactions, forming insoluble

solid species that adhere to the active material.[19] Similarly, oxidation reactions at the positive electrode form an analogous passivating film.[19] The SEI is essential to the function of Li-ion cells as it provides stability to the electrochemical system. The ideal SEI should be ionically conductive, electronically insulating, flexible, insoluble in the electrolyte, should adhere to the electrode material, and should consume minimal lithium.[17,19,39] However, it is exceedingly difficult to create such a perfect SEI, and this topic is heavily studied in the battery community.

Initial SEI formation occurs during the first charge of the cell. The process consumes lithium from the electrolyte, inherently reducing the capacity of the cell—this capacity loss is called irreversible capacity (IRC).[6,40] However, after initial formation, the SEI acts as a protective layer between the active material and the electrolyte, hindering further reactions and further electrolyte consumption. In reality, evidence shows that the SEI continues to grow and change over the cycle life of the cell, contributing to IRC and cell impedance growth.[17]

As suggested by Peled,[37] it is believed that several chemical species form the SEI in a 'mosaic-like' structure. The chemical composition of the SEI depends on the electrolyte and electrolyte additives,[10,17,19] however the composition and formation mechanisms are still not well understood.[27,38] Xu states that: "[SEI films] are difficult to characterize because of their sensitive chemical nature, elusive manner of formation, and the lack of reliable *in situ* characterization tools."[27] He goes on to adapt an old Greek proverb, saying: "the more we learn about SEI, the more we know how little we understand it."[27]

The left of Figure 1.7 depicts an electrode with SEI surrounding the layered graphite particles, while the blow up on the right shows the mosaic-like structure of the SEI, proposed by Peled.[37]

12

The different letters represent different chemical components of the SEI. As shown, the Li ions (purple circles) can still intercalate into the active material since the SEI is ionically conductive.
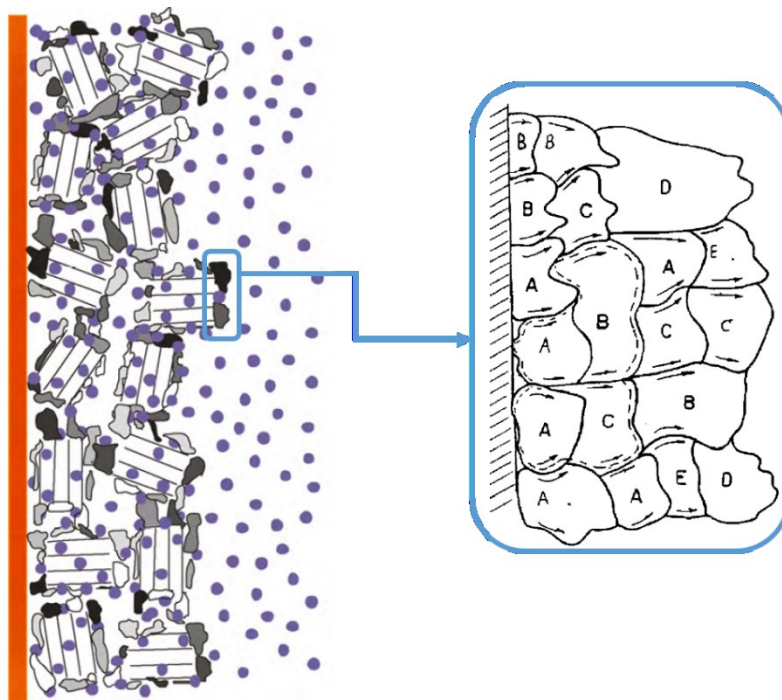
Figure 1.7: (Left) Graphite electrode showing electrode particles surrounded by SEI. Li ions (purple) are intercalated into the graphite particles and in the surrounding electrolyte. (Right) Blow up of mosaic-like SEI. Figure adapted from Verma et al.[18] and K. Xu.[19]

Lots of work has been done to try and quantify the thickness and composition of the SEI in Li-ion cells.[9,10,35,36,41–45] Madec et al.[10] used XPS analysis to determine chemical components of the SEI in NMC/graphite cells containing 2% VC. Figure 1.8 schematically illustrates the composition and thickness of the SEI on the graphite electrode after formation and after cycling, as shown by the authors.[10]
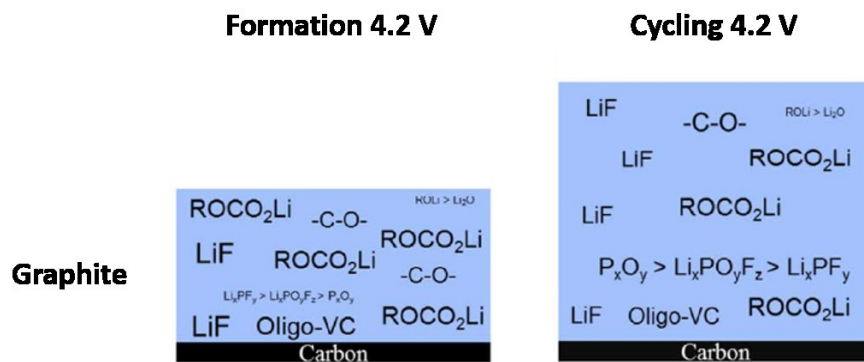
Figure 1.8: Schematic representation of the thickness and composition of SEI films on lithiated graphite after formation and after 25 cycles for cells containing 2% VC. The blue rectangle represents the SEI on a graphite electrode. The thickness of the SEI film is proportional to the height of the rectangle, and the components of the SEI are labeled within the rectangle. The font size and number of times a species appears is proportional to the amount found in the SEI. Figure adapted from Madec et al.[10]

The work in this thesis attempts to learn about properties of the SEI on NMC532 and graphite electrodes through the use of impedance spectroscopy and XPS. The studies involve the three electrolytes discussed in Section 1.2.3, therefore Table 1.1 was constructed to summarize the components of the SEI expected in these cells. The information in this table is based on interpretations of XPS data from Madec et al.,[9,10] Qian et al.,[35] and Ma et. al.[36]

Table 1.1: Chemical components of the SEI on a graphite negative electrode and a NMC532 positive electrode in cells cycled with control electrolyte, and control electrolyte with 2% VC or 1% LFO.[9,10,35,36]

Electrode/ Additive	Control	2% VC	1% LFO
Graphite negative	• Lithium containing carbonates • LiF • Li_2O • $LiPO_xF_y$, Li_xPF_y	• Lithium containing carbonates • LiF • Oligo-VC • ROLi, Li_2O • $LiPO_xF_y$, Li_xPF_y	• More LiF • Fewer carbonates
NMC532 positive	• Lithium containing carbonates • LiF	• LiF • Lithium containing carbonates • Oligo-VC	• More LiF • Fewer carbonates

Chapter 2: Experimental Methods

2.1   Cell Preparation

2.1.1   Pouch Cells

Single crystal NMC532/AG 402035-size wound pouch cells (40 mm x 20 mm x 3.5 mm jelly roll) with a capacity of 210 mAh at 4.2 V were used in these experiments. Dry (no electrolyte), vacuum sealed cells were received from LiFun Technology (Xinma Industry Zone, Golden Dragon Road, Tianyuan District, Zhuzhou City, Hunan Province, PRC, 412000). The positive electrode loading was 21.1 mg/cm^2, the density was 3.5 g/cm^3, and the active weight fraction was 94%. The negative electrode loading was 11.5 mg/cm^2, the density was 1.55 g/cm^3, and the active weight fraction was 95.4%. The separator material in the cells was a microporous polyethylene film with an aluminum oxide coating adjacent to the cathode material. The pouch cells were cut open in an argon-filled glovebox and dried under vacuum in a 100°C oven for 14 hours to remove any moisture before filling with electrolyte. Approximately 0.85 mL (~1 g) of electrolyte was used to fill each cell. Pouch cells underwent a formation process on a Maccor 4000 series charger, which involved wetting the cells at 1.5 V for 24 hours, followed by a C/20 charge to 4.2 V or 4.4 V, and a hold at top of charge for one hour. Some cells were removed at top of charge (TOC) while others were discharged to ~50% state of charge (SOC), which was ~3.8 V for these cells. Pouch cells were either disassembled after formation, to make symmetric cells and coin cells, or were cycled for long term cycling tests as described later in this Chapter. Figure 2.1 shows a pouch cell, an unwound electrode from a pouch cell, electrodes punched from pouch cell electrodes for coin cell making, and a built coin cell.

a) Pouch cell

b) Un-rolled pouch cell negative electrode

c) Punched negative and positive electrodes and BMF separator
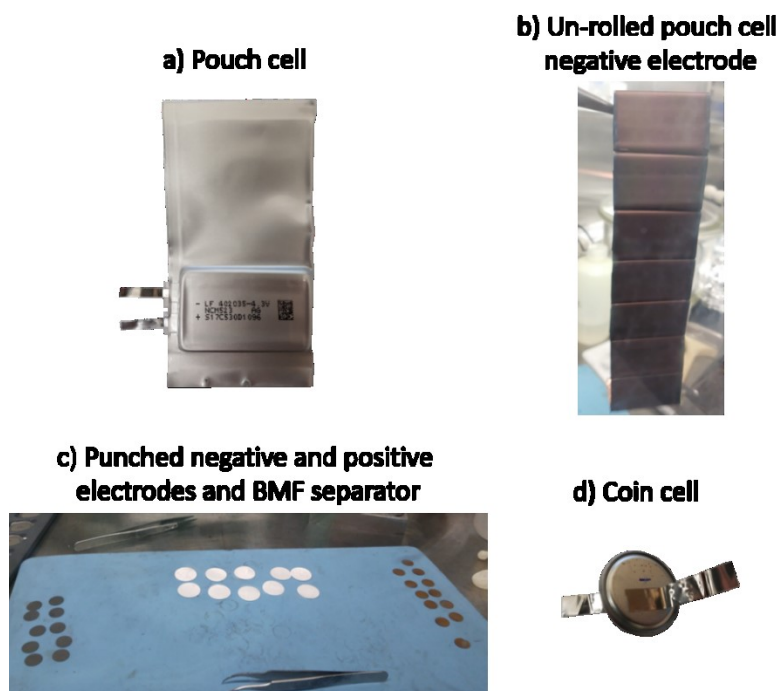
d) Coin cell

Figure 2.1: From pouch cell to coin cell. (a) A sealed 402035 size pouch cell, and (b) one of its electrodes un-rolled from the jelly roll. (c) NMC532 and graphite circular electrodes punched from pouch cell electrodes like the one shown in (b). (d) A coin cell made using circular electrodes as seen in (c).

2.1.2 Symmetric Cells and Coin Cells

Pouch cells were disassembled in an argon-filled glovebox for the construction of negative electrode symmetric cells (-/-), positive electrode symmetric cells (+/+), and full cell coin cells (+/-). In all experiments, two or three cells of the same type were fabricated to ensure repeatability. The same electrolyte that was used in the parent pouch cells was also used in the assembly of the symmetric cells and full coin cells. The electrodes punched for these cells had a surface area of 0.95 cm^2 and the separator used was a polypropylene blown microfiber separator (BMF – from 3M Co., 0.275 mm thickness, 3.2 mg/cm^2). Figure 2.2 shows the components of the coin cells for (-/-), (+/+), and (+/-) cells. The metal components of the cells (top casing, spring, spacer, and

bottom casing) were made of stainless steel. Aluminum sputtered metal components were also used in some studies.
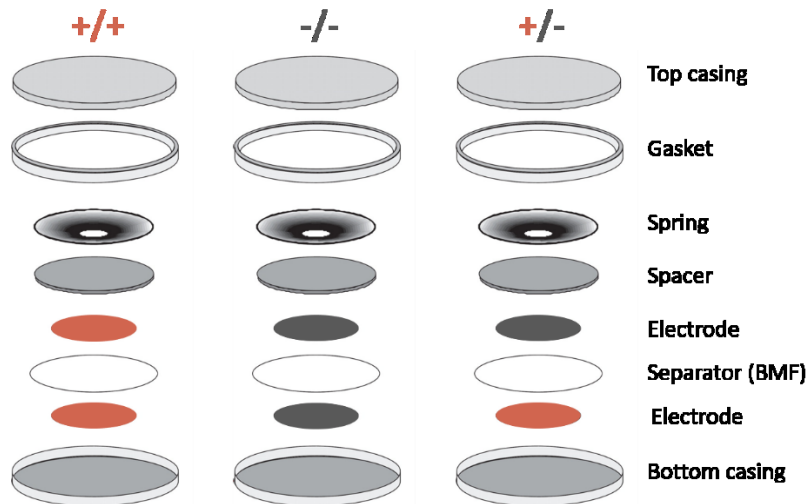
Figure 2.2: Expanded view of a positive symmetric cell (+/+), a negative symmetric cell (-/-), and a full coin cell (+/-). Red represents NMC532 positive electrodes and dark gray represents graphite electrodes. Figure adapted from Burns et al.[46]

The electrodes used in the symmetric cells and full coin cells were coated on both sides. Figure 2.3 compares the electrode stacks in (+/+), (-/-), and (+/-) cells to the electrode stack in a pouch cell. Figure 2.3 shows that there is an extra layer of electrode material (the coating on the back side of the electrode) between the foil current collector and the coin cell casing that is not present in the pouch cell. Chapter 3 will address the differences that arise in impedance spectra due to the additional layer of electrode material.

'Blocking' and 'non-blocking' cells were constructed for certain experiments in this thesis. Blocking cells were constructed using electrodes at 0% SOC obtained from dry pouch cells, and are termed 'blocking' because in uncharged electrodes, lithium ions are blocked from intercalating into the electrode material and therefore charge transfer due to Faradaic reactions is not possible.[47]

Non-blocking cells were constructed using electrodes at ~50% SOC or electrodes at TOC. Non-blocking electrodes are charged electrodes that allow for charge transfer of lithium into the active electrode material.
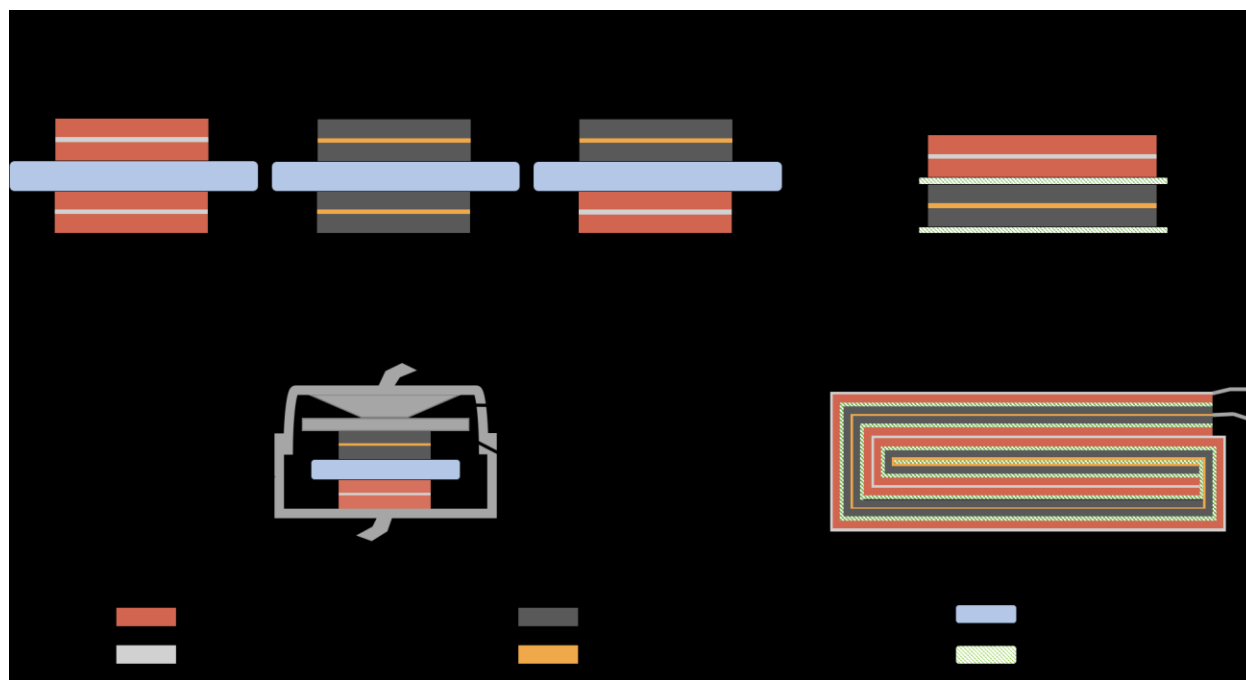
Figure 2.3: (a) Electrode stacks for (+/+), (-/-), and (-/+) coin cells each consisting of two double-sided electrodes and a BMF separator. (b) The electrode stack of a pouch cell containing double-sided positive and negative electrodes separated by a Celgard separator; electrodes for the coin cells were punched directly from pouch cell double-sided electrodes. (c) A cross-section of a coin cell containing an electrode stack, within a metal can and cap, with a metal spring and spacer to provide pressure. Note that the metal contacts are in contact with electrode material. (d) A schematic section of a pouch cell jelly roll (only 2 turns are shown) with the metal tabs connected directly to aluminum foil and copper foil current collectors.

2.2 Cycling Experiments

2.2.1 Electrolytes

The chemicals used were as follows: ethylene carbonate (EC), dimethyl carbonate (DMC), lithium hexafluorophosphate (LiPF$_6$), vinylene carbonate (VC), and lithium difluorophosphate (LiPO$_2$F$_2$

19

– called LFO here). All electrolytes were prepared in an argon-filled glove box using chemicals from BASF and Shenzhen Capchem (EC:DMC 3:7 (w:w) from BASF (purity > 99.9 %, water < 20 ppm), DMC from BASF (purity > 99.9 %, water < 10 ppm), $LiPF_6$ from Capchem (water < 20 ppm, HF < 5 ppm), VC from Capchem (purity > 99.9 % and water < 20 ppm), and LFO from Capchem). For all cells in this thesis, the control electrolyte mixture used was 1.2 M $LiPF_6$ in EC:DMC 3:7 (w:w). Other electrolytes used in the main studies in this thesis were the control electrolyte mixture with two percent by weight VC (called control + 2% VC) and the control electrolyte mixture with one percent by weight LFO (called control + 1% LFO). A study in Section 3.3 used electrolytes with low conductivity, which consisted of 0.3 M, 0.6 M, or 1.0 M $LiPF_6$ in DMC.

2.2.2   Pouch Cells

After formation, pouch cells destined for cycling experiments were degassed and re-sealed in an argon-filled glovebox. Cells were externally clamped to provide uniform pressure to the electrode stack while cycling. Pouch cells were cycled on a Neware battery tester (Shenzhen, China) at 40ºC. Cells were cycled between 3.0 V and either 4.2 V or 4.4 V at a charge/discharge rate of C/3 in constant current, constant voltage (CCCV) mode, with a cut-off current of C/20. One constant current C/20 cycle was done every 50 cycles.

2.2.3   Positive Symmetric Cells

The study discussed in Chapter 5 involved cycling (+/+) cells. Cycling was done on a Maccor 4000 series charger at 30ºC. Symmetric cells built for cycling experiments used aluminum coated metal components for reduced hardware corrosion,[48] and were sealed with an epoxy adhesive (Loctite EA 1C, Henkel Corp., Mississauga, ON) around the gasket to prevent possible electrolyte leaking.

Cells were cycled between -0.5 V and +0.5 V or between -0.9 V and +0.9 V. For the ±0.5 V protocol, the voltage limits correspond to one electrode cycling between 3.69 V and 4.13 V (vs. Li/Li$^+$) and the other electrode cycling between 4.30 V and 3.73 V (vs. Li/Li$^+$). For the ±0.9 V protocol, the voltage limits correspond to one electrode cycling between 2.78 V and 4.47 V (vs. Li/Li$^+$) and the other electrode cycling between 4.60 V and 3.64 V (vs. Li/Li$^+$). In both protocols, cells were cycled with a 90 µA constant current for two cycles, followed by 180 µA constant current cycling. The 90 µA current corresponds to a C-rate of about C/45 for ±0.9 V cells and C/25 for ±0.5 V cells. The 180 µA current corresponds to a C-rate of about C/20 for ±0.9 V cells and C/12 for ±0.5 V cells. Cells were removed from cycling for impedance measurements after the first two cycles, and then every 10 cycles thereafter.

2.3   Electrochemical Impedance Spectroscopy (EIS)

2.3.1   Introduction to Impedance Spectroscopy

EIS is an *in situ* technique used to obtain detailed impedance information about an electrochemical system. In EIS, the impedance of the system is measured at a range of frequencies. The most common method of implementation involves applying a sinusoidal voltage signal to the system at one frequency and measuring the resulting current at that frequency.[49] This measurement is repeated for all frequencies of interest. Figure 2.4 shows an example of an input voltage signal (top) with an amplitude of ±10 mV, and the corresponding output current signal (bottom) shifted by θ relative to the input signal. The input voltage signal is centered around the open circuit voltage (OCV) of the cell and must be kept small—on the order of a few mV—to remain in the electrically linear region of the system.
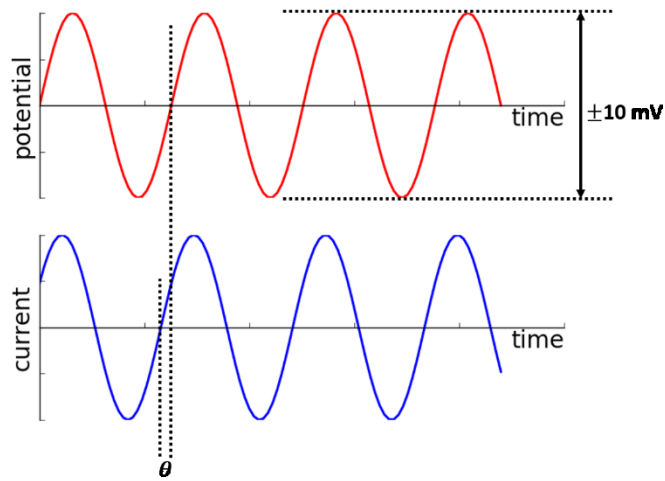
Figure 2.4: (Top) AC input voltage of ±10 mV and (bottom) AC output current with a phase shift, θ.

$$v(\omega, t) = V\cos(\omega t) \tag{2.1}$$

$$i(\omega, t) = I\cos(\omega t + \theta) \tag{2.2}$$

Equations 2.1 and 2.2 show the voltage and current signal as functions of frequency and time, where V is the amplitude of the voltage signal, I is the amplitude of the current signal, ω is the frequency ($\omega=2\pi f$, where f is in Hz), and θ is the phase difference. The impedance, at one frequency is then defined as:

$$Z(\omega) = \frac{v(\omega, t)}{i(\omega, t)} = \frac{V\cos(\omega t)}{I\cos(\omega t + \theta)} \tag{2.3}$$

Using Euler's equation, the voltage and current signals maybe be represented as a complex exponential, and the impedance can be written as a complex number as follows:

22

$$Z(\omega) = \frac{Ve^{j(\omega t)}}{Ie^{j(\omega t+\theta)}} = |Z|e^{-j\theta} = |Z|\cos(\theta) - |Z|j\sin(\theta) \tag{2.4}$$

The real and imaginary parts of impedance are:

$$Re(Z) = |Z|\cos(\theta) \tag{2.5}$$

$$Im(Z) = -|Z|\sin(\theta) \tag{2.6}$$

Impedance in an electrical system originates from resistive, capacitive, and inductive passive elements. Using complex numbers, is it possible to derive the impedance of these passive electric circuit elements. Starting with $v(\omega, t) = Ve^{j\omega t}$ as the input signal, Ohm's Law can be used to find the impedance for a resistor:[50]

$$i(\omega, t) = \frac{v(\omega, t)}{R} = \frac{Ve^{j\omega t}}{R} = Ie^{j\omega t} \tag{2.7}$$

$$Z_r(\omega, t) = \frac{v(\omega, t)}{i(\omega, t)} = \frac{Ve^{j\omega t}}{Ie^{j\omega t}} \tag{2.8}$$

$$\boxed{Z_r = R} \tag{2.9}$$

Starting with the same input voltage signal, the impedance for a capacitor can be calculated as follows:[50]

$$i(\omega, t) = C\frac{dv(\omega, t)}{dt} = C\frac{dVe^{j\omega t}}{dt} = Cj\omega Ve^{j\omega t} \tag{2.10}$$

$$Z_C(\omega, t) = \frac{v(\omega, t)}{i(\omega, t)} = \frac{Ve^{j\omega t}}{j\omega CVe^{j\omega t}} \tag{2.11}$$

$$Z_C(\omega) = \frac{1}{j\omega C} \qquad (2.12)$$

For an inductor, it is easier to start with a $i(\omega, t) = Ie^{j\omega t}$ current signal, to eliminate the need for integration. The impedance can be solved as follows:[50]

$$v(\omega, t) = L\frac{di(\omega, t)}{dt} = L\frac{dIe^{j\omega t}}{dt} = Lj\omega Ie^{j\omega t} \qquad (2.13)$$

$$Z_L(\omega, t) = \frac{v(\omega, t)}{i(\omega, t)} = \frac{j\omega LIe^{j\omega t}}{Ie^{j\omega t}} \qquad (2.14)$$

$$Z_L(\omega) = j\omega L \qquad (2.15)$$

Figure 2.5 summarizes the derived equations for a resistor, capacitor and inductor, and plots the frequency response for each element alone on a Nyquist plot. A Nyquist plot is a plot of negative imaginary impedance vs. real impedance, and each point represents one frequency measurement. Figure 2.5 (a) shows that a resistor manifests as a point on the real axis of a Nyquist plot as there is no imaginary part of the impedance equation and no variation with frequency. Figure 2.5 (b) shows that a capacitor alone has a negative imaginary response, which shows up as a vertical line in the Nyquist plot. Figure 2.5 (c) shows that an inductor has a positive imaginary response with frequency.

a)

$$Z_R = R$$

b)

$$Z_C = \frac{1}{j\omega C}$$

c)

$$Z_L = j\omega L$$
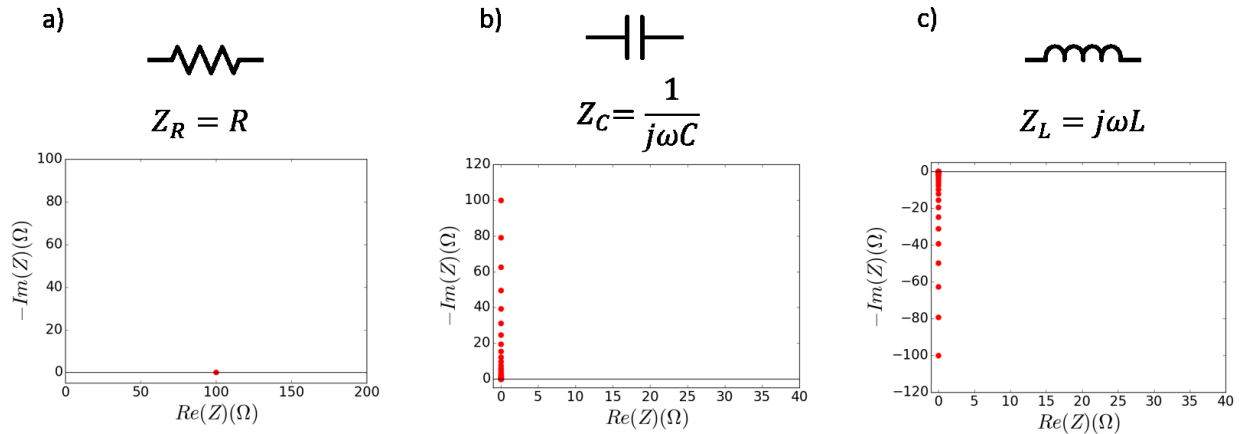
Figure 2.5: Electric circuit symbol, impedance equation, and Nyquist plot for (a) a resistor, (b) a capacitor, and (c) an inductor.

Figure 2.6 shows a typical Nyquist plot for a Li-ion cell. Each point is a measurement at a specific frequency, and the frequency increases from right to left. Here the frequency range is from 10 mHz to 100 kHz. The features of the spectrum can be modeled by equivalent electrical circuit models, which will be discussed in more detail in Section 2.3.2. Additional circuit elements pertinent to this discussion will be introduced here.
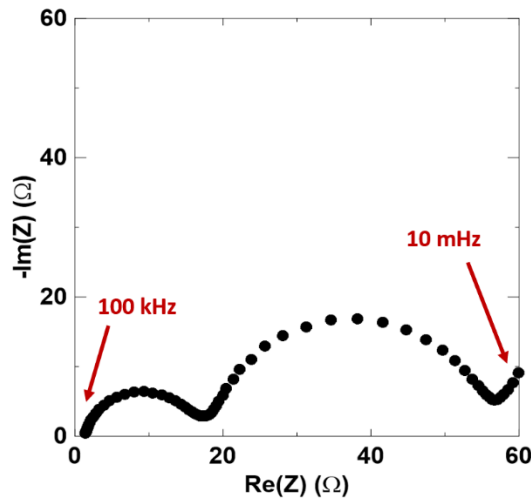
Figure 2.6: A basic Nyquist plot with the upper and lower frequency points labeled.

25

In electrochemical systems, constant phase elements (CPE) are often used in place of capacitors to model an electrical double layer. CPEs are 'distributed' elements that account for the observed frequency dispersion in real systems. The dispersion is attributed to surface roughness, and adsorption and diffusion at the surface.[51] The impedance of a CPE is:

$$Z_{CPE}(\omega) = \frac{1}{T(j\omega)^{\phi}}$$

(2.16)

In Equation 2.16, T is a constant with units $(Fs^{\phi-1})$ and ϕ is the constant phase exponent where $0 < \phi < 1$. Equation 2.16 reduces to the equation for a capacitor (Equation 2.12) when $\phi=1$. The angle of rotation of a CPE from a vertical (90º) capacitive element is $\alpha = 90°(1-\phi)$.[51]

Another distributed circuit element is the Warburg impedance, which represents diffusion of Li^+ in the active material. The Warburg impedance can be written as:

$$Z_W(\omega) = \frac{\sigma}{\omega^{1/2}} - j\frac{\sigma}{\omega^{1/2}}$$

(2.17)

In Equation 2.17, σ is a constant containing the diffusion coefficient.[52]

2.3.2   Model for Interpretation

Many electric circuit models have been presented in the literature to model EIS spectra from Li-ion cells. Circuit models are used to fit data and quantify impedance features and are typically composed of a combination of elements discussed here. Ionic diffusion in the electrolyte and electronic resistivity in active material are typically modeled by a simple resistor. Interfaces in an electrochemical system introduce a resistance and a double layer capacitance. Therefore, basic interfaces can be modeled by a RC circuit—a resistive and capacitive element in parallel. As
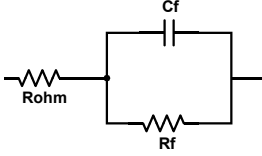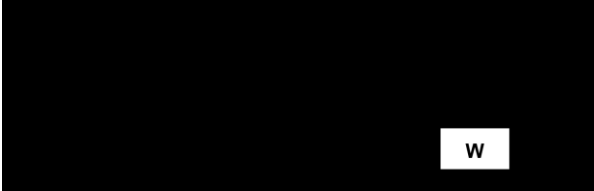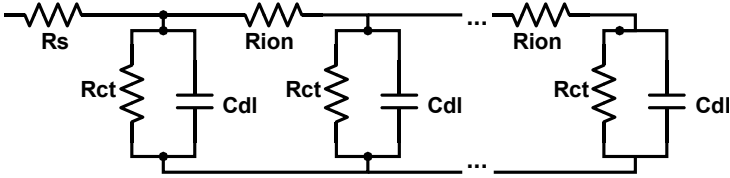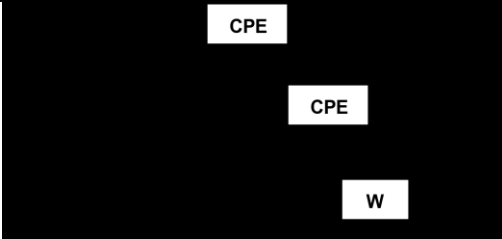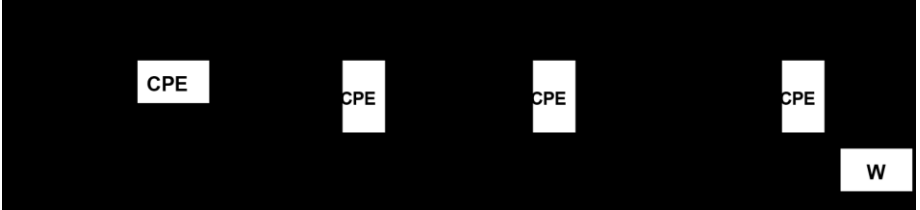
mentioned, Warburg impedance elements are used to model Li^+ diffusion in the active material. Ionic resistance in the pores of the active material is sometimes accounted for by additional elements.

Table 2.1 includes some equivalent circuit models from the literature. In Table 2.1, R_{ohm} represents ohmic resistances, which are sometimes broken down into R_s, solution resistance and R_{el}, electronic resistance. Contact resistance is denoted by R_{cont}, and charge transfer resistance is represented by R_{ct}, or R_f (Faradaic). C_f and C_{dl} represent Faradaic and double layer capacitance, while constant phase element representations of capacitance are shown as CPE. Finally, Warburg diffusion is shown as W.

The equivalent circuit models in Table 2.1 account for varying degrees of complexity. There is debate among battery scientists about the true interpretation of impedance spectra for Li-ion cells.[12,53–56] However, it should also be noted that conversion between circuit models is sometimes possible. Figure 2.7 shows several common ways to draw circuit diagrams. Buteau et al.[54] have shown that these models are equivalent; they produce the same impedance spectra, and it is possible to convert from one to the other.

Table 2.1: Equivalent circuit models to model Li-ion cell impedances found in the literature.

Reference	Equivalent circuit
1. Liaw et al.[57]	
2. Randles[58]	
3. Zhang et al.[20]	
4. Ogihara et al.[59]	
5. Nara et al.[60]	
6. Atebamba et al.[53]	
7. Landesfeind et al.[61]	

a) Voigt-type circuit

b) Ladder-type circuit

c) Maxwell-type circuit

d) Another way to draw ladder-type circuit
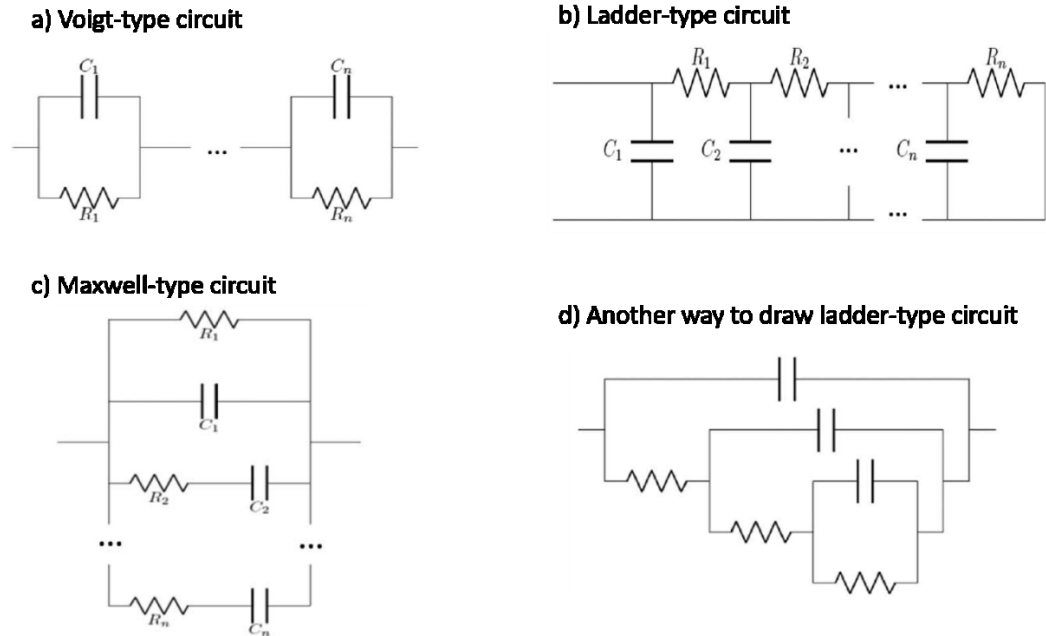
Figure 2.7: Examples of circuit model representations which are equivalent to each other, from Buteau et al.[54]

Figure 2.8 shows the equivalent circuit models used to fit the data in this thesis. The top circuit diagram was used to model impedance in (-/-) cells, while the bottom circuit was used to model impedance in (+/+) cells and (+/-) cells. Both models include a resistor, R-CPE components, and a Warburg element in series.
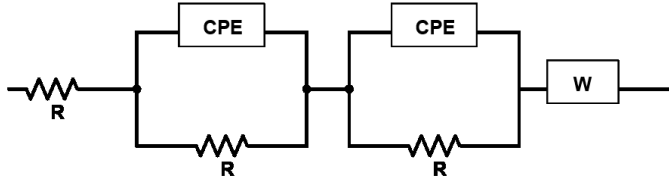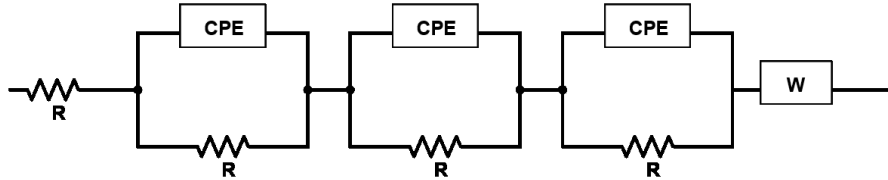
Figure 2.8: Circuit models used to fit (top) negative symmetric cell data, and (bottom) positive symmetric cell and full coin cell data.

Figure 2.9 shows how each circuit element in the equivalent circuit model relates to a feature in a Nyquist plot, and Figure 2.10 shows the origins of the elements in a physical cell model. As previously seen in Figure 2.5, a simple resistive element shifts the Nyquist spectra along the real axis. The horizontal shift on the x-axis represents the ionic and electronic resistance in the electrolyte and active material in this model. RC circuits with ideal capacitors appear on a Nyquist plot as a semicircle. R-CPE circuits appear as depressed semicircles; the value of ϕ in the CPE equation (Equation 2.16) determines the degree to which the semicircle is depressed. The width of the semicircle is the value of the resistive element in the R-CPE circuit. In Figure 2.9, the low frequency semicircle (right) represents charge transfer impedance, and the high frequency semicircle (left) represents contact impedance between electrode particles and the current collector. Warburg impedance appears in a Nyquist plot as a 45° 'tail' at low frequencies.

Figure 2.10 shows a simple cell model zooming into one active electrode particle in a cell. The electrolyte contributes to the series resistance and the diffusion of Li^+ in electrode particles is the source of the Warburg impedance. The electrode particle/current collector interface is the source

30

of the contact impedance, while the electrolyte/SEI/electrode particle interfaces are the source of the charge transfer impedance. In this model, R_{ct} includes the resistance to Li^+ desolvation at the electrode surface in addition to the resistance due to Li^+ passing through the SEI and into the surface of the active electrode particles. In this model of charge transfer impedance, negative charge from electrons in the electrode particles builds up at the electrode particle surface, and positive charge from Li^+ builds up at the outer Helmholtz plane. The Li^+ cannot get closer to the SEI before desolvation occurs. The SEI is electronically insulating, thus an electrical double layer is formed.
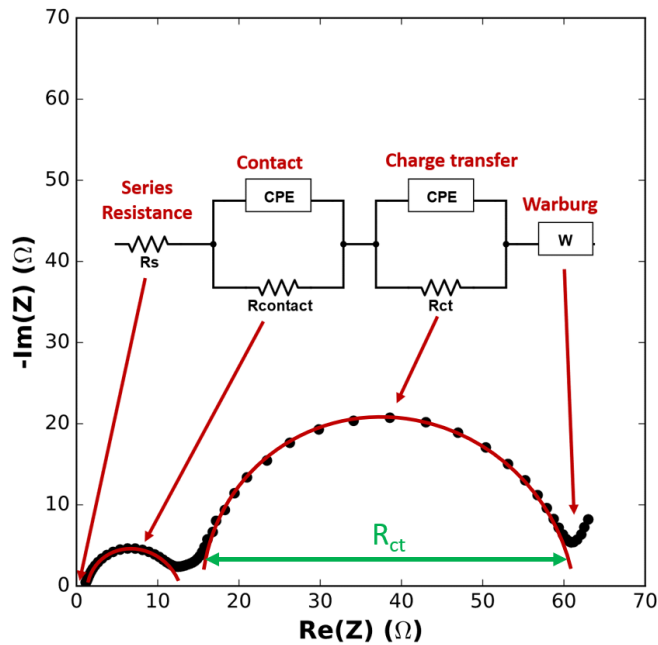
Figure 2.9: A Nyquist plot with an equivalent circuit showing which circuit component corresponds to each spectrum feature. The four components, from left to right are: (1) the series resistance; (2) the contact impedance; (3) the charge transfer impedance; (4) the Warburg impedance.

31
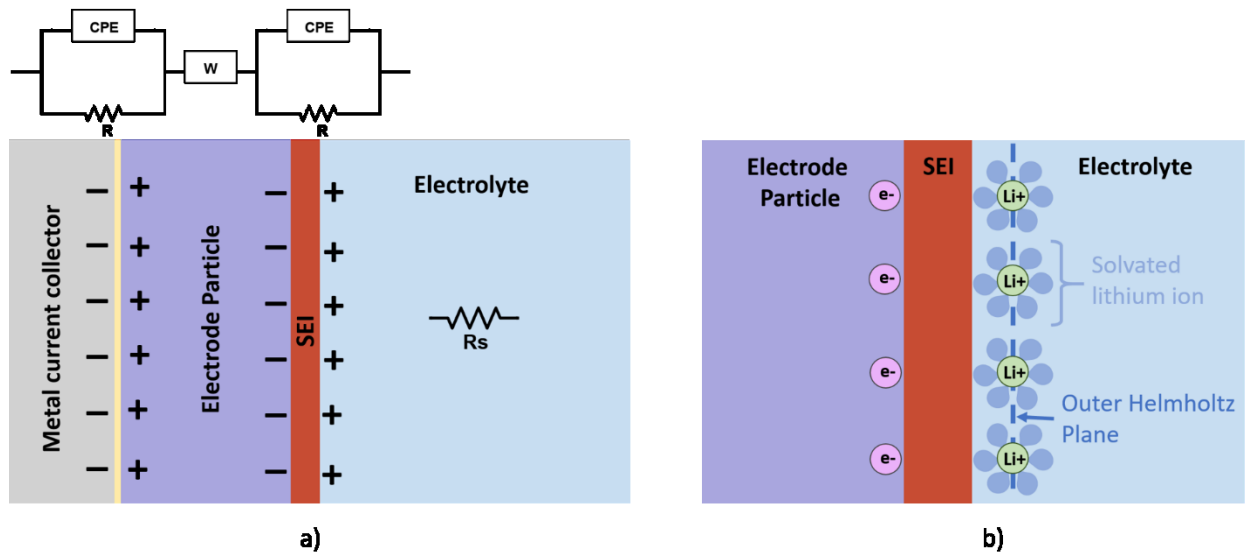
Figure 2.10: (a) Cell model showing contributors to impedance and the associated circuit element. (b) The electrode particle/SEI/electrolyte interface showing the build-up of charge at the outer Helmholz plane and in the active material, creating a double layer.

Spectra from (+/+) cells had a small additional feature in the spectra, at mid-frequencies between the contact impedance and charge transfer impedance semicircles. Therefore, an additional R-CPE circuit was added for improved fitting. This additional feature may be attributed to ionic resistance in the pores of the active material, as suggested by Landesfeind et al.,[47,61] Ogihara et al.,[59] and Nara et al.,[60] but has not been investigated in depth in this work.

The addition of the positive and negative symmetric cell data by frequency, as in a Bode plot, should give the full coin cell spectrum for cells from the same parent pouch cell.[62] Equation 2.18 shows this relation.

$$\frac{(+/+)\,(f)}{2} + \frac{(-/-)\,(f)}{2} = (+/-)(f) \tag{2.18}$$

In (+/-) cells, several R-CPE components can be justified as there are many different interfaces from the positive and negative electrodes. A good fit can be achieved with three R-CPE

components in the cells tested in this work. However, it becomes difficult to determine exactly what each component physically represents because of the superposition of positive and negative symmetric cell spectra described in Equation 2.18. In this thesis, (+/+) and (-/-) cells are investigated to facilitate the separation of impedance contributions from positive and negative electrodes. Full cells are primarily used as a check that the symmetric cells are representative of the parts of a full cell. Figure 2.11 shows an example of a (-/-) cell Nyquist plot fit with the equivalent circuit model in Figure 2.8 (top).
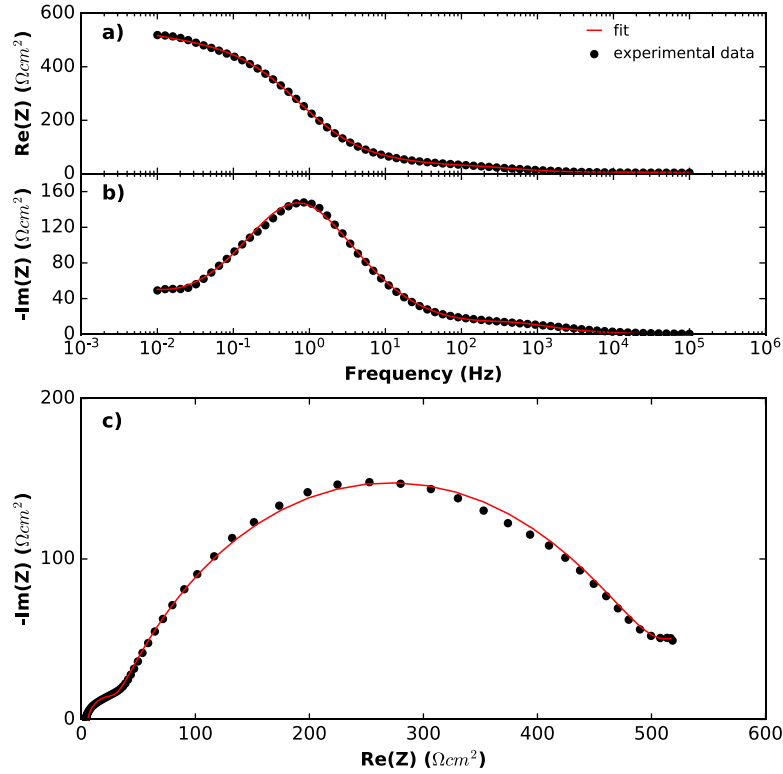
Figure 2.11: Nyquist and Bode plots for a (-/-) cell with EC:DMC 3:7 (w:w) + 1.2 M LiPF$_6$ electrolyte. Experimental EIS data is shown in black and the fitting results for the data in red. The real component of impedance versus the logarithm of frequency is shown in (a); the negative imaginary component of impedance versus the logarithm of frequency is shown in (b), and Nyquist plot is shown in (c). Fits were completed using RelaxIS 3 - Impedance Data Analysis (rhd instruments GmbH & Co. KG, Germany).

2.3.3   Activation Energy and Double Layer Capacitance

In a simple model, it is expected that R$_{ct}$ follows the Arrhenius equation:[63,64]

$$\frac{1}{R_{ct}} = Ae^{-\frac{E_a}{k_BT}} \tag{2.19}$$

In Equation 2.19, R$_{ct}$ is the resistance to Li$^+$ motion through the electrode/electrolyte interface, E$_a$ is the activation energy associated with Li$^+$ hopping through sites in the SEI material, k$_B$ is the

Boltzmann constant, T is the temperature, and A is a proportionality constant. In these studies, EIS was performed at temperatures ranging from -10°C to 40°C. By plotting the logarithm of the charge transfer resistance versus the inverse of temperature, extraction of the activation energies associated with transport of Li^+ through the negative electrode SEI and the positive electrode SEI was possible. It is therefore believed that the activation energy is related to SEI composition.

The capacitance associated with a CPE may be calculated experimentally using the following equation:[65]

$$C = \frac{1}{\omega_{max} R_{ct}}$$
(2.20)

where ω_{max} is the frequency at which the imaginary part of impedance has a maximum, and R_{ct} is the charge transfer resistance. This capacitance may represent the double layer capacitance across the electrolyte/SEI/electrode interfaces. The formula for the capacitance of a parallel plate capacitor is:

$$C = \frac{\epsilon \epsilon_0 A}{d}$$
(2.21)

where ϵ is the dielectric constant of the material between the plates, ϵ_0 is the permittivity of free space, A is the plate area and d is the spacing between the plates.[66] Equation 2.21, is sometimes used to discuss SEI thickness, where C is calculated with Equation 2.20 using parameters measured using EIS, A is the surface area of the active material, and d is the SEI thickness.[56,67]

2.3.4 Experimental Setup

A BioLogic VMP3 was used to measure EIS of pouch cells, symmetric cells, and full coin cells. The spectra were collected over a frequency range of 100 kHz to 10 mHz with ten points per decade and a perturbation amplitude of 10 mV. For temperature dependent tests, spectra were collected sequentially at -10°C, 0°C, 10°C, 20°C, 30°C, and 40°C. Measurements were taken at 10°C at the beginning, middle, and end of the experiments to ensure repeatability. For (+/+) cycling experiments, EIS was done only at 10°C due to time constraints. All Nyquist plots in this work show area specific impedances calculated based on the surface area of the electrodes. Negative and positive symmetric cell impedances were divided by two in order to only account for one of the two electrodes, as described in Equation 2.18. Fitting of EIS data was completed using RelaxIS 3 - Impedance Data Analysis (rhd instruments GmbH & Co. KG, Germany).

2.4 ΔV

The effect of internal cell resistance on the cell can also be quantified using charge and discharge curves. Figure 2.12 shows an example of a charge and discharge curve on a voltage vs. capacity plot. The difference between the two curves arises from the internal resistance, shown in the circuit on the graph. During charge, the measured average voltage is increased by the voltage across the resistor (IR), and during discharge, the measured average voltage is decreased by the same amount (IR). Equation 2.22 shows that the difference between the average charge voltage and the average discharge voltage, ΔV, is equal to 2IR. ΔV is a useful metric for estimating internal resistance changes in cycling cells.

$$\Delta V = V_{avg,charge} - V_{avg,discharge} = 2IR \tag{2.22}$$
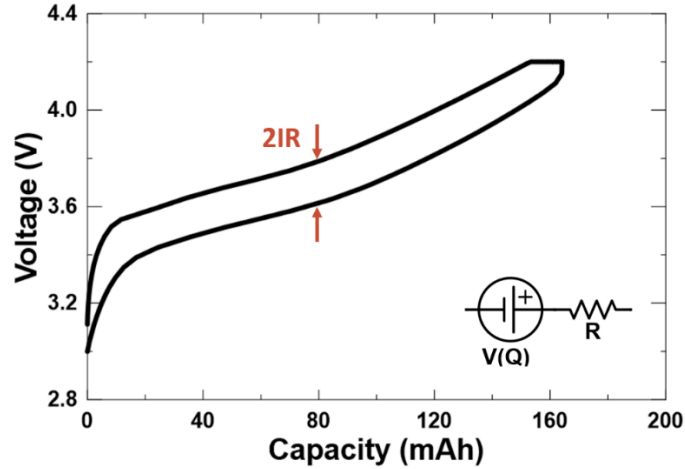
Figure 2.12: Voltage vs. capacity for a charge and discharge cycle of a Li-ion cell. The circuit in the bottom right shows a power source with a resistor, representing the internal resistance of the cell. Internal resistance manifests as a 2IR voltage shift between charge and discharge curves.

2.5   X-Ray Photoelectron Spectroscopy (XPS)

XPS is a technique used to study the chemical composition of surfaces. It has been used in this thesis to probe the composition of the SEI. During XPS, X-rays irradiate the surface of a sample, interacting with core electrons in the surface atoms of the sample. If the energy of the incident X-ray is high enough, it can eject an electron from the atom in a process known as the photoelectric effect. In the XPS apparatus, the ejected photoelectrons are collected in an analyzer and separated based on kinetic energy (KE).[68] Figure 2.13 shows an example of a photon with energy hυ ejecting an electron from the 2p orbital of an atom. The binding energy of the ejected electron can be calculated using the following equation:[68]

$$BE^F = h\nu - KE - \phi_{sp} \qquad (2.23)$$

In Equation 2.23, BE^F is the binding energy of the electron with respect to the Fermi energy, KE is the measured kinetic energy, $h\nu$ is the x-ray energy, and ϕ_{sp} is the work function of the analyzer. For the experiment, the sample and analyzer are in electrical contact, making their Fermi energies the same. Because the KE is the energy measured by the analyzer, the work function subtracted from the photon energy must be the work function of the analyzer.
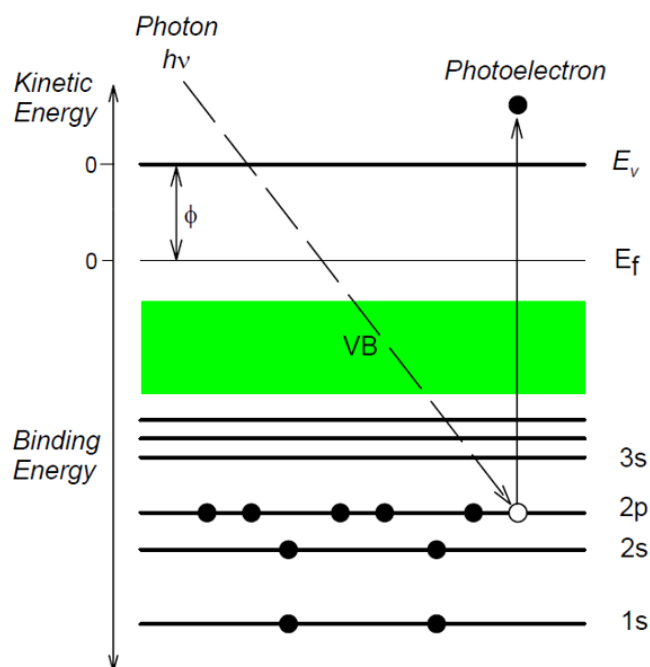
Figure 2.13: Depiction of the photoelectric effect showing an incident photon ejecting a photoelectron from the 2p orbital of an atom. VB is the valence band; E_v is the vacuum energy of the sample; ϕ is the work function of the sample; and E_f is the Fermi level. The work function of the spectrometer, ϕ_{sp}, cannot be shown on this diagram as the diagram only represents energy levels in the sample. Reproduced from Smart et al.[69]

The BE varies depending on the type of atom or molecule from which the electron was emitted, therefore XPS can detect different chemicals based on BE. For example, in a C-F bond, valence electrons are pulled toward the more electronegative fluorine atom. This causes an increase in the

38

binding energy of the core electrons in the carbon atom relative to the binding energy of the core electrons in carbon atoms from a C-C bond. Correspondingly, a C-F bond causes a decrease in the binding energy for the core electrons in the fluorine atom. Spectra are typically plotted as counts per second (CPS) vs. BE, and resulting peaks are analyzed to learn about the composition of the sample. The number of electrons collected by the analyzer (CPS) is proportional to the concentration of that element in the sample.[68]

2.5.1 Experimental Procedure

Square samples (1 cm^2) were cut from double sided electrodes in an argon-filled glovebox and rinsed three times in DMC solvent to remove residual EC and $LiPF_6$ salt. Once dry, samples were mounted on sample holders using copper tape (3M). To ensure that samples never came in contact with air, samples were transferred to the XPS apparatus using a custom-made transfer suitcase built at Dalhousie University.[9] The analysis chamber was under ultra-high vacuum (UHV) (< 2 x 10^{-9} mbar) for data acquisition. XPS was done using a SPECS spectrometer with a PHOIBOS 150 hemispherical energy analyzer. Samples were irradiated with a Mg Kα source (hυ = 1253.5 eV). See ref. [9] for more details about the experimental procedure. All XPS experiments in this thesis were run by Rochelle Weber (many thanks).

2.5.2 Data Analysis

Data analysis was performed using CasaXPS software (version 2.3.12). For all spectra, calibration of BE was done using the 284.8 eV C-C peak. A Shirley-type background was fit around the regions of interest and the background was subtracted from the data. Peaks were fit in CasaXPS and assigned to different SEI and electrode material components based on BE. It was often difficult

to resolve peaks since many peaks associated with SEI components may overlap each other. Figure 2.14 (a) shows a typical C 1s spectrum from a graphite electrode after formation. This spectrum illustrates the difficulty in resolving peaks with similar BE. The C 1s spectrum of graphite shows a peak associated with the lithiated graphite that composes the active electrode material (LiC_6—dark gray). This peak may be monitored over cycle life to gauge the negative SEI thickness. Figure 2.14 (b) shows a typical O 1s spectrum from an NMC electrode after formation. This spectrum contains a peak (light gray) associated with the lattice oxygen in the NMC transition metal oxide material. This peak may be monitored over cycle life to gauge positive SEI thickness.
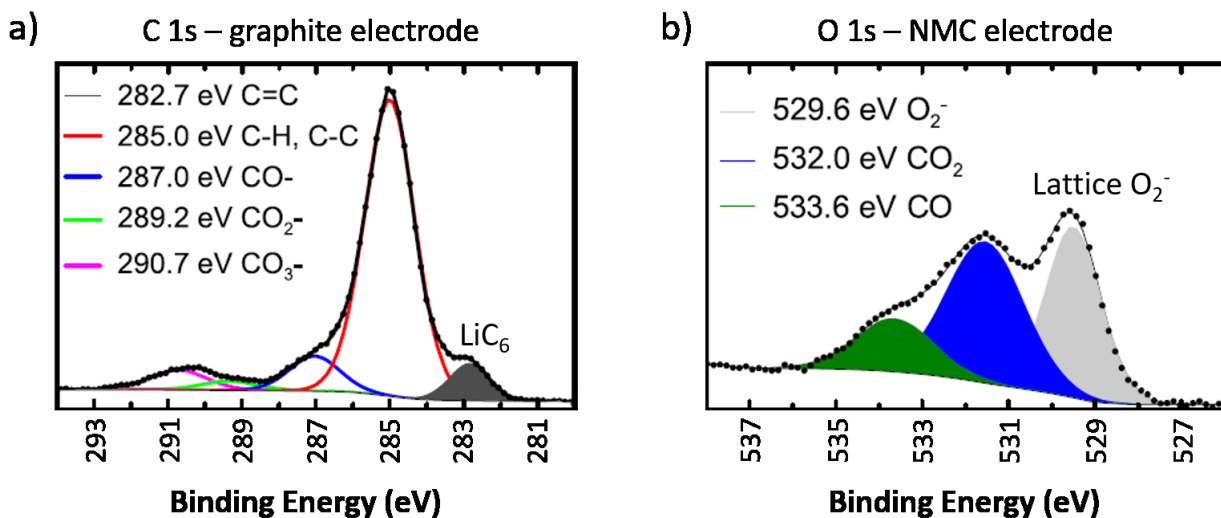
Figure 2.14: Typical XPS spectra for Li-ion cell electrodes. (a) C 1s peak for a graphite electrode highlighting the lithiated graphite (LiC_6) peak. (b) O 1s peak for an NMC electrode showing the lattice oxygen peak. Adapted from Xia et al.[70]

A table of peak BEs associated with SEI components and active electrode materials can be found in Table 2.2. BE values were collected from many references.[9,10,42,43,70–75]

Table 2.2: Binding energies of peaks commonly found in Li-ion cell electrodes.

Peak	Binding energy (eV)	Species
F 1s	688.1	C-F
	687	P-F
	685	LiF
O 1s	534.5	polymerized VC
	533	C-O
	531.5 - 532	C=O
	529.5	NMC lattice oxygen
C 1s	290 - 291	CO_3
	290.8 – 291.1	C-F
	~289	C=O
	288 – 289	CO_2
	288.5	O-C=O
	286.7	C-O
	286.2 – 286.6	C-H
	284.8	C-C
	~283	lithiated graphite
P 2p	~137	P-F
	134	P-O
Ti 2p	~464	TiO_2 (2p1/2)
	458.3	TiO_2 (2p 3/2)
TM + Li	~66	Ni (3p)
	~60	Co (3p)
	~54 - 55	Li (1s)
	~47 - 49	Mn (3p)

2.6   dV/dQ Analysis

Differential voltage analysis is used to quantify parameters of cell degradation over cycle life.[76]

The voltage curve of a full Li-ion cell can be calculated by taking the difference between the

positive and negative electrode half cell voltage curves. Half cells are typically made with a lithium metal reference electrode. Both the positive and negative electrode half cells have features in their voltage (vs. Li/Li$^+$) vs. capacity curves. While it is difficult to see clear features on a voltage vs. capacity plot, taking the derivative of voltage with respect to capacity (dV/dQ) and plotting vs. capacity (Q) amplifies the features and makes them easier to fit accurately. Figure 2.15 (a) and (b) show dV/dQ vs. capacity curves of a NMC532 electrode half cell and a graphite electrode half cell, respectively. The dV/dQ curve of a full NMC532/graphite cell can be fit by taking the difference of the half cell dV/dQ curves, as shown in the following equation.[76]

$$\frac{dV_{full}}{dQ} = \frac{dV_+}{dQ} - \frac{dV_-}{dQ} \qquad (2.24)$$

The positive and negative half cell curves are multiplied by a mass factor and a capacity shift is applied in order to fit the full cell dV/dQ vs. capacity curve. The four parameters—masses of the positive and negative electrodes and relative slippages of the positive and negative electrodes— are useful for studying cell degradation. Figure 2.15 (c) shows a measured dV/dQ curve from a full cell, and the fit obtained by applying Equation 2.24 to the half cell curves in (a) and (b) that have been adjusted by mass and slippage parameters.
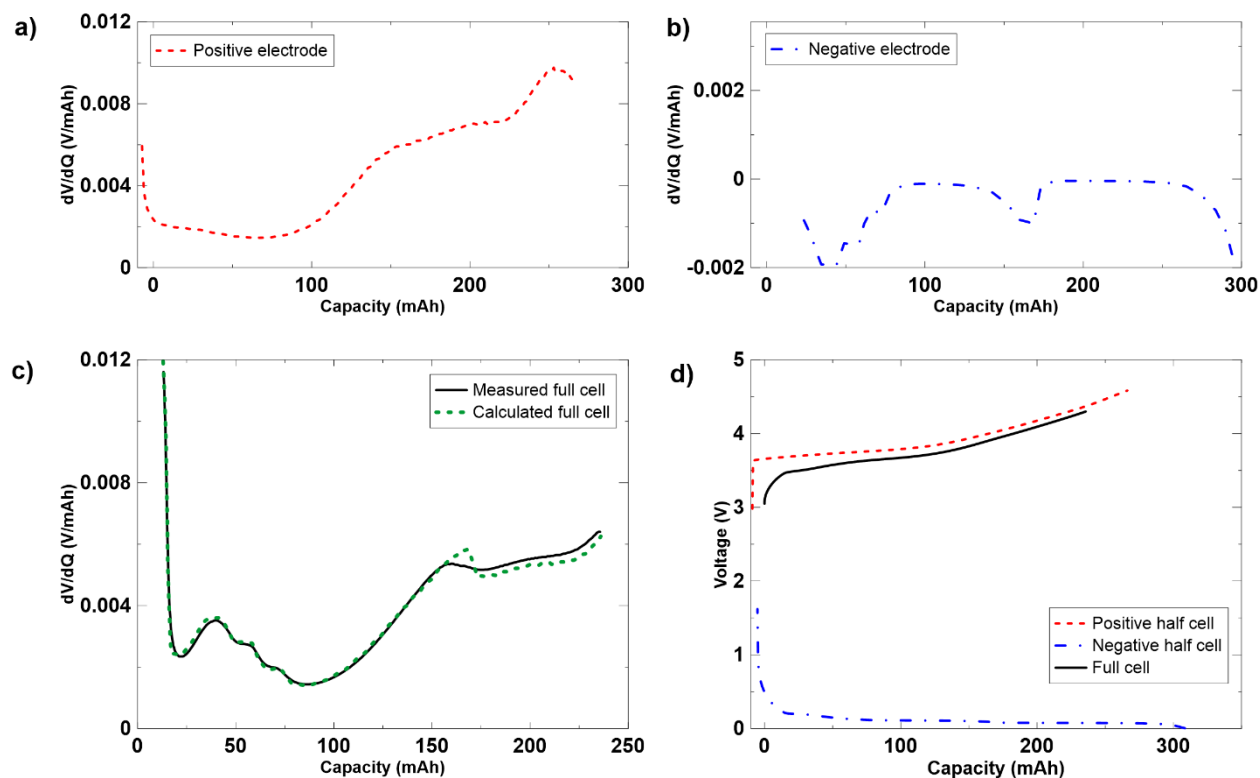
Figure 2.15: (a) dV/dQ vs. capacity of a NMC532/Li metal half cell. (b) dV/dQ vs. capacity of a graphite/Li metal half cell. (c) dV/dQ vs. capacity of a full NMC532/graphite cell with the fit obtained using (a) and (b) reference curves. (d) Voltage vs. capacity of the positive half cell, negative half cell, and full pouch cell.

If there is a difference in mass between a fit for an initial full cell voltage curve and a voltage curve after cycling, then it can be concluded that some mass of active electrode material was electrically disconnected, contributing to capacity fade. If there is a larger relative slippage after cycling, then it can be concluded that capacity has been reduced through loss of Li^+ inventory. This Li^+ inventory loss is attributed to lithium being consumed by negative electrode SEI growth. In NMC532/AG cells, there is typically very little mass loss observed over many cycles, and capacity fade is mainly attributed to slippage from the consumption of Li^+ inventory by the negative electrode SEI.[24,77]

Figure 2.15 (d) shows the half cell voltage curves and full cell voltage curve after fitting. Relative slippage can be seen on this plot. The voltage of each electrode vs. Li/Li^+ can be obtained from

43

this graph for any full cell potential. The software used to do dV/dQ fitting was developed in the

Dahn lab.[76]

Chapter 3: Interpreting EIS Spectra in Li-ion Symmetric Cells

EIS is a characterization tool frequently used in Li-ion cell research, however the interpretation of spectra is debated in the literature.[12,53–56] The interpretation of several aspects of the Nyquist spectra will be addressed in this chapter. The presentation of Nyquist plots is also a point of consideration. Figure 3.1 shows data plotted on equal axes and unequal axes. Spectra are sometimes presented on equal axes to check semicircular features and 45º angle Warburg tails, however, unequal axes amplify features allowing for easier identification of impedance components. Therefore, unequal axes will be used for Nyquist plots in the remainder of this thesis.

To justify the use of double-side coated electrodes, Section 3.1 presents a comparison of EIS spectra from cells made with single-sided and double-sided electrodes, as well as a comparison of full coin cells and pouch cells. Section 3.2 investigates the high frequency semicircle of Nyquist plot spectra using cells with blocking electrodes. This section also highlights the importance of measuring EIS at low temperatures. Finally, the effect of varying electrolyte conductivity is examined in Section 3.3.
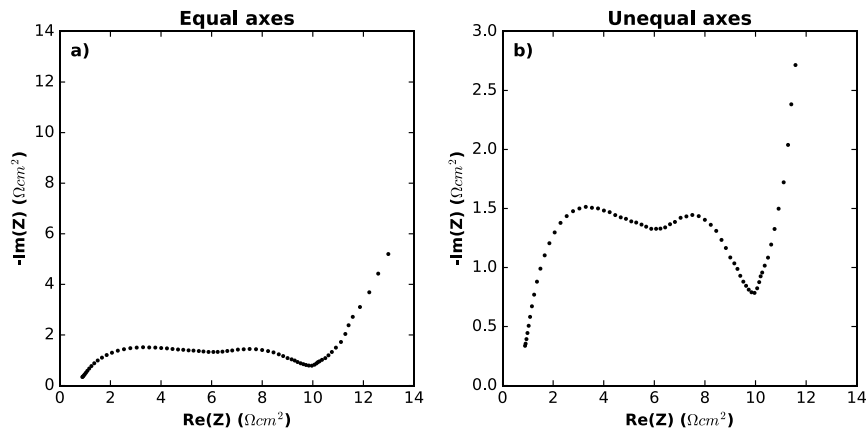
Figure 3.1: Area specific Nyquist plots of AG (-/-) cells disassembled at 3.8 V and measured at 40ºC. (a) The axes are equal magnitudes; (b) the axes are unequal and show features more clearly.

3.1   Symmetric Cell Verification

For all studies in this thesis, two or three identical symmetric cells and full coin cells were made to ensure repeatability. Figure 3.2 shows data for pairs of (-/-), (+/+), and (+/-) cells, demonstrating good agreement between duplicate measurements.
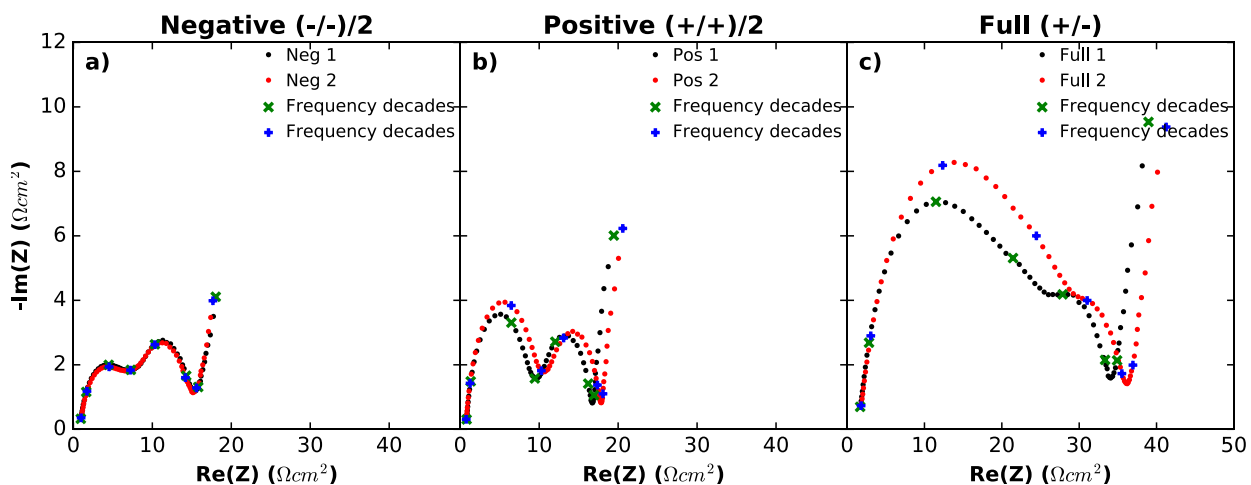
Figure 3.2: Area specific Nyquist spectra for (a) NMC532 (+/+) cells, (b) AG (-/-) cells, and (c) NMC532/AG (+/-) cells measured at 30°C showing the repeatability of duplicate cells. The NMC532/AG pouch cell from which the electrodes originated was formed to 4.2V and disassembled at 4.2V and contained control electrolyte.

46

As described in Chapter 2, electrodes for symmetric cells and full coin cells were punched from pouch cell electrodes with active material coated on both sides of the foil current collector. The additional coating on the backside of the electrodes could lead to concern about the validity of studying these cells as representative of the performance of their parent pouch cells. There is a small section at the end of pouch cell electrodes on which the active material is only coated on one side. This section is fragile and only large enough to punch electrodes for a single coin cell; therefore, making single-sided duplicate and triplicate cells is not a viable option. The single-sided section was used to make the single-sided symmetric cells presented below.

Figure 3.3 (a) and (b) compare (+/+) and (-/-) cells made with single- and double-sided electrodes. Frequency decades are marked. Figure 3.3 (a) demonstrates the similarity in the charge transfer impedance semicircle (mid-low frequency) between the two cells, while the contact impedance semicircle (high frequency) is larger in the double-sided cells. This suggests that the additional electrode material in the (+/+) double-sided cells amplifies the contact impedance but does not impact the charge transfer process. Figure 3.3 (b) shows that the single- and double-sided (-/-) cells have almost identical Nyquist spectra. Since lithiated graphite is a good conductor, the additional backside of the electrode has no effect on the contact impedance. Figure 3.3 (c) compares data from a double-sided full coin cell with its parent pouch cell. Charge transfer resistance is similar, while the major differences occur in the high frequency contact impedance portion of the spectrum. Overall, Figure 3.3 (a-c) show evidence that double-sided electrode cells provide accurate charge transfer impedance results. The contact impedance is amplified relative to the contact impedance measured in pouch cells; however, this amplification allows for the contact impedance to be studied more easily.

Figure 3.3 (d) shows the effect of using different metal hardware components in the construction of coin cells. The data shown in black were measured from a (+/+) cell that used a stainless steel spring, spacer, and top and bottom casings (see Figure 2.2 for symmetric cell expanded view). The data in red were measured from a (+/+) cell that used aluminum coated top and bottom casings, and two aluminum coated spacers. Electrodes in the two cells were from the same parent pouch cell. The charge transfer impedance semicircle is very similar in the two cells, while the high frequency semicircle is larger in the cell that used stainless steel hardware. This suggests that the high frequency semicircle is due to contact impedance, which will be further investigated below.
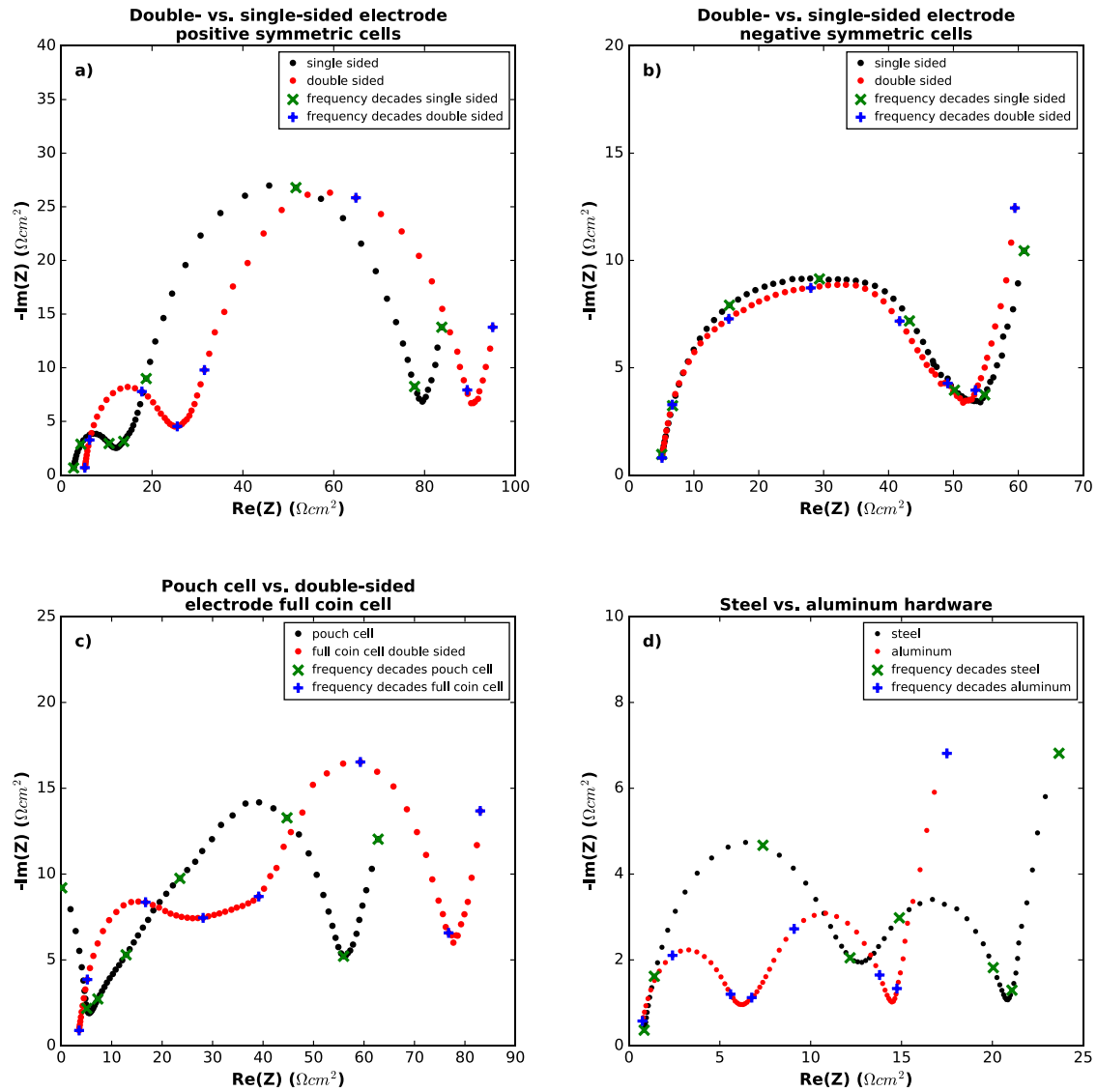
Figure 3.3: Nyquist spectra for (a) NMC532 (+/+) cells, and (b) AG (-/-) cells with single- and double-sided electrodes. (c) Nyquist spectra for a NMC532/AG pouch cell and a (+/-) cell assembled using double-sided electrodes from the same pouch cell. Spectra in (a-c) were measured at 10°C, and used electrodes from cells formed to 4.4V and disassembled at 3.8V that contained control + 1% LFO electrolyte. (d) Nyquist spectra for NMC532 (+/+) cells using steel hardware and aluminum coated hardware. Spectra in (d) were measured at 30°C and used electrodes from cells formed to and disassembled at 4.4V that contained control electrolyte. Frequency decades are labeled on all spectra.

3.2 High Frequency Semicircle

The high frequency semicircle that appears in EIS spectra of Li-ion cells has been debated in the literature. It has been interpreted as impedance due to Li^+ movement through the SEI,[78–81] and also as impedance originating at the interface between electrode particles and the metal current collector.[53,55,61,82] In this section, evidence is provided for the later interpretation, which will be called contact impedance.

Figure 3.4 shows a Nyquist plot of blocking and non-blocking full coin cells measured at 20°C with frequency decades indicated. The non-blocking cell did formation, therefore charge transfer is possible and SEI formation has occurred on the electrodes. The electrodes in the blocking cell did not undergo formation and electrodes were at 0% SOC, therefore lithium intercalation leading to charge transfer is suppressed. Figure 3.4 shows that the high frequency semicircular portion of the Nyquist plot is almost identical for the blocking and non-blocking cells with the indicated frequencies lining up well. The non-blocking cell has an additional lower frequency semicircular feature which does not exist in the blocking cell. This feature is associated with the charge transfer, which exists in the non-blocking cell, but does not exist in the blocking cell.
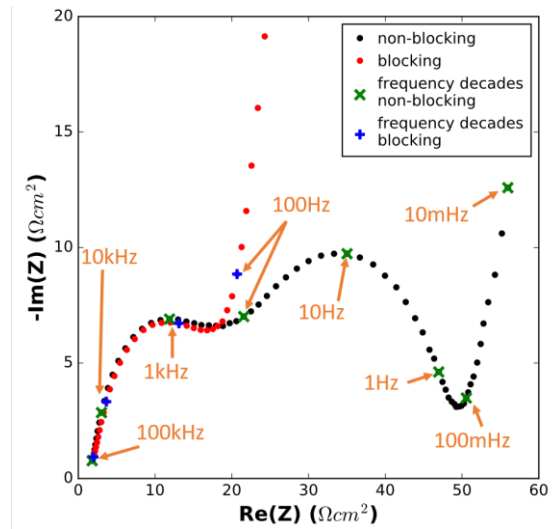
Figure 3.4: Area specific Nyquist plots of blocking and non-blocking (+/-) cells measured at 20°C with frequency decades labeled. Cells contain a NMC532 positive electrode and an AG negative electrode with control electrolyte. The non-blocking full coin cell was constructed using electrodes from a pouch cell at 3.8 V that had been formed to 4.2 V.

Figure 3.5 and Figure 3.6 show Nyquist plots of negative symmetric cells, positive symmetric cells, and full coin cells made from blocking and non-blocking electrodes. Figure 3.5 shows spectra measured at -10°C, 0°C, and 10°C, while Figure 3.6 shows spectra measured at 20°C, 30°C, and 40°C. The high frequency semicircle of the blocking and non-blocking cells matches very well at all temperatures. Bode plots showing the real component of impedance versus the logarithm of frequency, and the negative imaginary component of impedance versus the logarithm of frequency can be seen in Appendix B.1.
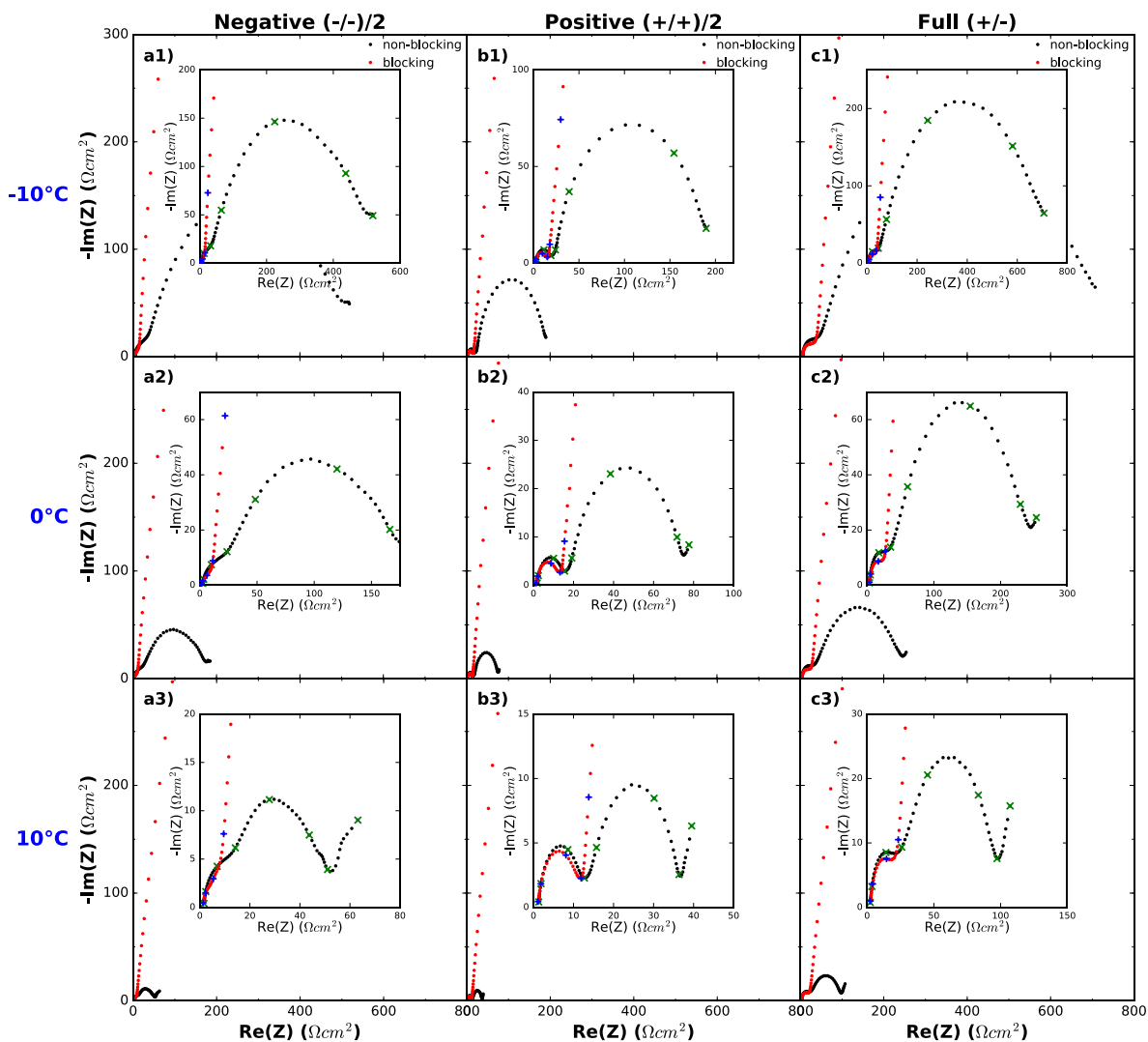
Figure 3.5: Area specific Nyquist plots of blocking and non-blocking (a1-a3) (-/-) cells, (b1-b3) (+/+) cells, and (c1-c3) (+/-) cells. Cells used a NMC532 positive electrode and an AG negative electrode with control electrolyte. The non-blocking cells were constructed using electrodes from a pouch cell at 3.8 V that had been formed to 4.2 V. (a1), (b1), and (c1) were measured at -10°C; (a2), (b2), and (c2) were measured at 0°C; and (a3), (b3), and (c3) were measured at 10°C. Frequency decades are indicated with blue + symbols for blocking data and with green x symbols for non-blocking data.
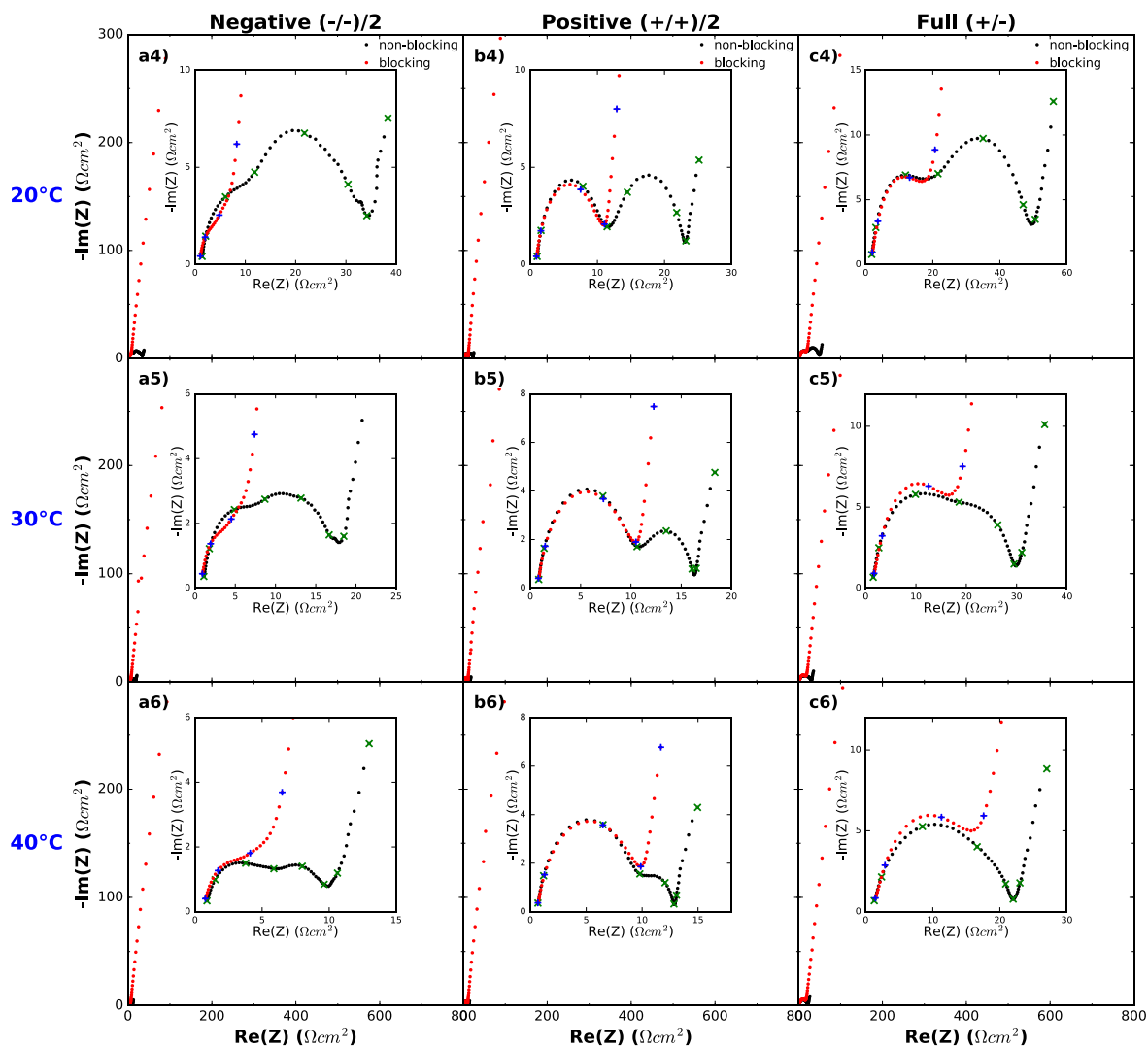
Figure 3.6: Area specific Nyquist plots of blocking and non-blocking (a4-a6) (-/-) cells, (b4-b6) (+/+) cells, and (c4-c6) (+/-) cells. Cells used a NMC532 positive electrode and an AG negative electrode with control electrolyte. The non-blocking cells were constructed using electrodes from a pouch cell at 3.8 V that had been formed to 4.2 V. (a4), (b5), and (c6) were measured at 20°C; (a4), (b5), and (c6) were measured at 30°C; and (a4), (b5), and (c6) were measured at 40°C. Frequency decades are indicated with blue + symbols for blocking data and with green x symbols for non-blocking data.

Figure 3.7 shows the contact impedance (high frequency semicircle) as a function of temperature for blocking electrode cells. The contact impedance increases slightly with decreasing temperature for (+/+), (-/-), and (+/-) cells. In contrast, the charge transfer impedance (low frequency

semicircle) increases dramatically with decreasing temperature as indicated in Figure 3.5 and Figure 3.6. At high temperatures, separation of the contact impedance and the charge transfer impedance becomes difficult because the scale of the two features is similar and the characteristic frequencies of the two semicircles are closer together. At low temperatures, separation of the features becomes much easier. This data shows the utility of measuring EIS at low temperatures in situations where the charge transfer component of impedance is of interest.
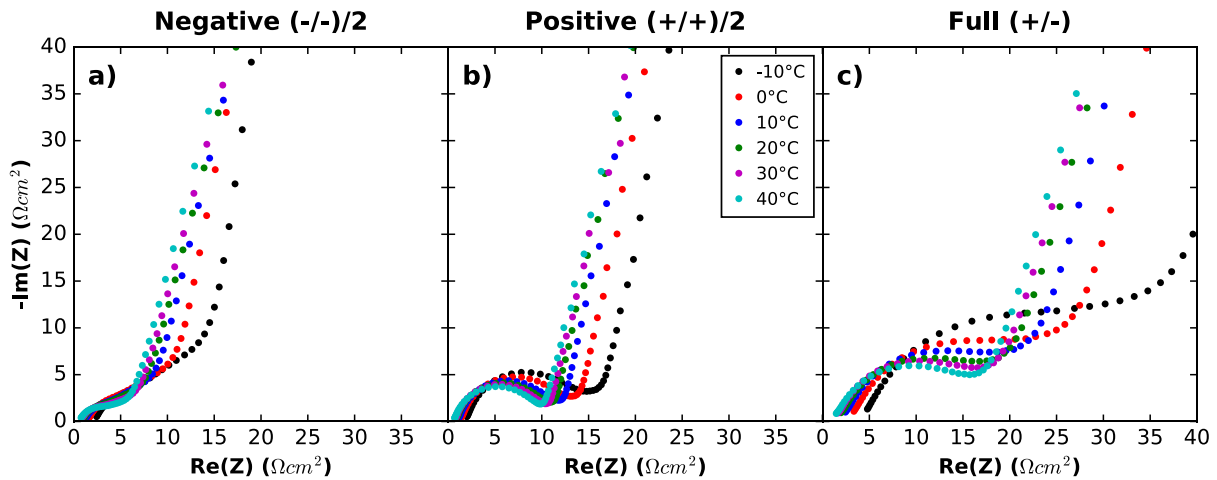
Figure 3.7: Area specific Nyquist plots of (a) (-/-) blocking electrode cells, (b) (+/+) blocking electrode cells, and (c) (+/-) blocking electrode cells. Plots (a-c) show spectra obtained at -10°C, 0°C, 10°C, 20°C, 30°C, 40°C.

3.3   Conductivity Effects

In interpreting EIS data for Li-ion cells with porous electrodes, ionic resistance in the pores is often stated as a contributing factor to cell impedance. Theoretical resistance in cylindrical pores can be calculated as suggested by Lasia,[51] and by Orazem and Tribollet,[50] resulting in a ~45° angle straight line impedance feature at high frequencies on a Nyquist plot. Additional calculation by Lasia show that the angle and shape of the impedance feature can differ considerably based on pore shape and

54

when taking into account the capacitance at the electrode surface.[51] Landesfeind et al. also showed that if the pore capacitance is imperfect and modeled with a CPE with $\phi < 1$, the angle of the impedance feature is less than 45º.[47] This ~45º angle line has been observed by various Li-ion cell researchers.[47,53,59,61,83] This feature is not typically obvious in spectra with NMC532/AG cells containing EC:DMC 3:7 (w:w) + 1.2 M LiPF$_6$ electrolyte. In the study presented here, electrolytes with low LiPF$_6$ concentrations, some having extremely low ionic conductivities, were used to try and expose the impedance feature resulting from ionic resistance in the pores.

Blocking electrode (+/+), (-/-), and (+/-) cells were constructed using NMC532 and AG electrodes obtained from dry pouch cells. Four electrolytes with different conductivities were used in the cells. These electrolytes were: 1) 1.2 M LiPF$_6$ in EC:DMC 3:7 (w:w), 2) 1 M LiPF$_6$ in DMC, 3) 0.6 M LiPF$_6$ in DMC, and 4) 0.3 M LiPF$_6$ in DMC. EIS was performed at 10ºC.

Figure 3.8 shows a plot of conductivity vs. molarity of LiPF$_6$ in DMC. Figure 3.8 (a) includes data at a wide range of molarities and temperatures, and illustrates that the electrolyte conductivity reaches a maximum near 2 M LiPF$_6$ in DMC. Conductivity also increases with temperature. Figure 3.8 (b) includes data in the range of LiPF$_6$ molarities used in this study and at the EIS measurement temperature (10ºC).
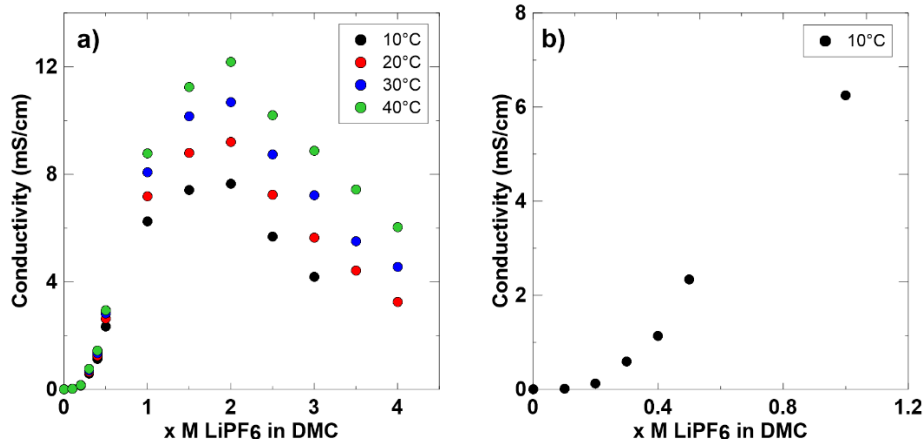
Figure 3.8: Conductivity vs. molarity of LiPF$_6$ in DMC solvent. Figure (a) contains a range of temperatures and molarities, while (b) contains LiPF$_6$ molarities between 0 M and 1.2 M at 10ºC only. Data courtesy of Eric Logan, Dalhousie University.

Figure 3.9 shows EIS spectra of (-/-), (+/+), and (+/-) blocking electrode cells containing electrolytes with varying conductivities. Figures (a2), (b2), and (c2) are blow ups of the corresponding plots above them. As LiPF$_6$ concentration decreases (and ionic conductivity decreases), the high frequency intercept shifts to the right. As described in Chapter 2, the shift along the x-axis is due to a series resistance and depends on the ionic resistivity of the electrolyte, therefore this result is expected. Another feature to consider is the appearance of an additional feature in the Nyquist plot in the mid-high frequency range. The feature, indicated by a circle in Figure 3.9 (b1) and (b2), appears to be a straight line at an angle less than 45º. This feature is most pronounced for positive symmetric cells with 0.3 M LiPF$_6$ (the electrolyte with the lowest conductivity) shown in Figure 3.9 (b1). Figure 3.9 (a2), (b2), and (c2) show that this feature becomes more dominant and obvious with decreasing ionic conductivity of the electrolyte. It appears that this feature overlaps with the contact impedance at high frequencies. Additionally, at very low salt concentrations (0.3 M LiPF$_6$), the contact impedance semicircle also appears to get very large. Xiong et al.[84] conducted EIS studies on symmetric cells in which LiPF$_6$ concentration

56

was varied in EMC-based electrolyte solutions. In these studies, charge transfer impedance increased dramatically with decreasing ionic conductivity of the electrolyte. Contact impedance was not studied explicitly but did appear to be affected by $LiPF_6$ concentration in certain cases.[84] The effect of ionic conductivity on the contact impedance has not been studied widely and could be an area for future investigation.

The appearance of a mid-high frequency < 45° angle straight line suggests that ionic resistance in the electrode pores is observed at low electrolyte conductivities and that the pores may be varied in shape and/or have imperfect capacitance which is more accurately modeled with a CPE. In the case of 1.2 M $LiPF_6$ in EC:DMC 3:7 (w:w) electrolyte, the ionic resistance in the pores is not significant compared to the other impedances.
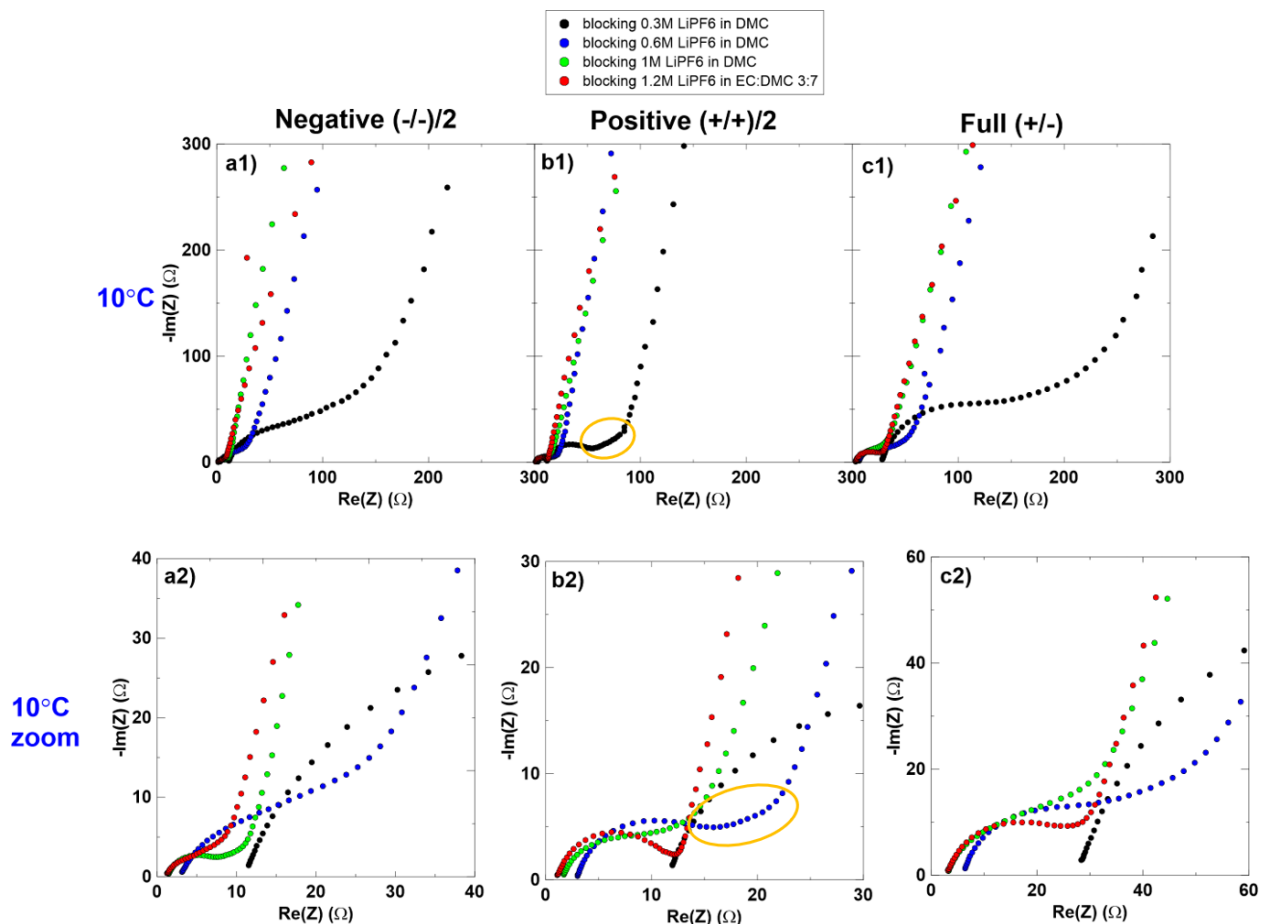
Figure 3.9: Nyquist plots for cells containing electrolytes of different LiPF$_6$ concentration in DMC or in EC:DMC 3:7 (w:w). (a1) and (a2) show spectra from (-/-) AG cells; (b1) and (b2) show spectra from (+/+) NMC532 cells; (c1) and (c2) show spectra from (+/-) NMC532/AG cells.

3.4   Conclusions

The reliability of data from double-sided electrode cells was established through the comparison of single- and double- sided electrode cells and the comparison of full coin cells and pouch cells. The repeatability of hand-assembled symmetric cells and coin cells was shown. Through the use of blocking electrode symmetric cells, it was demonstrated that the high frequency semicircle is due to non-Faradaic reactions and it was suggested that this semicircle includes contributions from the impedance at the interface between the metal current collector and the active electrode

particles. The conclusion that the high frequency semicircle is due to the interface between electrode particles and the metal current collector is also supported by the changes in this feature due to coin cell hardware and due to double-sided electrodes. It was also shown that measuring impedance spectra at low temperatures, ideally less than 10°C, allows for clear separation of the impedance contributions due to charge transfer and contact resistance. Ionic resistance in the electrode pores was observed for cells containing low conductivity electrolyte but is only a minor contributor to the impedance spectra in cells with higher conductivity, such as those used in the remainder of this thesis.

Chapter 4: Studies of the SEI in Li(Ni$_{0.5}$Mn$_{0.3}$Co$_{0.2}$)O$_2$/ Artificial Graphite Cells After Formation and After Cycling

The purpose of this study was to probe properties of the SEI after cell formation and after long term cycling. It has been shown that cells containing different electrolyte additives have SEIs of different chemical composition.[9,10,35,36,41–43] Figure 1.1 showed that electrolyte additives have a major impact on capacity retention. The effect of electrolyte additives on Li-ion cells has been studied widely, and correlation between capacity fade and impedance growth has been demonstrated.[11–13,15,16,36] In this study, the positive and negative electrode SEIs were probed for cells containing three different electrolyte mixtures. SEI impedance, composition, and thickness were studied using two techniques: XPS analysis, and temperature dependent EIS. XPS was used to study the composition of the SEI, and to glean information about SEI thickening. EIS studies using symmetric cells allowed for examination of cell impedance from each electrode separately. Contact resistance, charge transfer resistance, and the capacitance associated with R$_{ct}$ were examined. Additionally, temperature dependent EIS allowed for the extraction of activation energy values using the Arrhenius equation (Equation 2.19).

As previously described, in this work, R$_{ct}$ includes the resistance to Li$^+$ desolvation at the electrode surface in addition to the resistance due to Li$^+$ passing through the SEI and into the surface of active electrode particles. For the electrolytes and interfaces studied here, we believe the contribution from desolvation is much smaller than that due to ion conduction through the SEI. This is because changes to the electrolyte involving only a few percent of electrolyte additive, which will not change desolvation at all, greatly impact R$_{ct}$, as will be shown later. Therefore, the contribution from desolvation is neglected in the discussion below. Other references which show

the strong impact of electrolyte additives on R_{ct} include Xia et. al,[70] who studied triallyl phosphate, Nelson et al,[14] who studied propene sultone, Petibon et al.[15] who studied vinylene carbonate and trimethoxyboroxine, Wang et al.[12] who studied p-Toluenesulfonyl isocyanate, Yang et al.[16] who studied lithium difluorophosphate, and Q.Q. Liu et al.[13] who studied vinylene carbonate, triallyl phosphate, and 2% propene sultone (PES), 1% ethylene sulfate (DTD) and 1% tris(-trimethylsilyl)-phosphite (TTSPi) (PES211).

The results and discussion section of this chapter is divided into several parts. Section 4.2.1 compares cells that were formed to different voltages and disassembled at different SOC. Section 4.2.2 compares cells formed and cycled to 4.2 V. Section 4.2.3 compares cells formed and cycled to 4.4 V. Section 4.2.4 summarizes the R_{ct} and $R_{contact}$ results for all cells in the previous two sections (Section 4.2.2 and Section 4.2.3). Finally, Section 4.2.5 presents XPS results for cells with control + 2% VC electrolyte.

4.1   Experimental

NMC532/AG pouch cells were used in this study. Pouch cells were filled with one of three electrolytes: control, control + 2% VC, or control + 1% LFO, as detailed in Section 2.1.3. NMC532/AG pouch cells in this study underwent formation to 4.2 V or to 4.4 V as described in Section 2.1.1. Two cells intended to do formation to 4.2 V did formation to 4.3 V instead. These cells are in the section which compares cells at different SOC. One batch of pouch cells was disassembled after formation, while a second batch was cycled for several months on a Neware charger before disassembly, as described in Section 2.2.1. Cells that only did formation were disassembled at TOC or at ~50% SOC (3.8 V), and cells that were cycled were disassembled at

3.8 V. At 3.8 V, the potential of the NMC532 electrodes was 3.90 V vs. Li/Li$^+$ and the potential of the AG electrodes was 0.10 V vs. Li/Li$^+$. At 4.2 V, the potentials were 4.28 V and 0.08 V (vs. Li/Li$^+$) for the NMC532 and AG electrodes respectively. At 4.4 V, the potentials were 4.47 V and 0.07 V (vs. Li/Li$^+$) for the NMC532 and AG electrodes respectively.

All pouch cells were disassembled and made into symmetric cells and full coin cells as described in Section 2.1.2. The symmetric cells and full coin cells did EIS at multiple temperatures in the following order: 10°C, 0°C, -10°C, 10°C, 20°C, 30°C, 40°C, 10°C. Measurements at 10°C were done at the beginning, middle, and end to ensure repeatability. EIS data was fit using electric circuit models as described in Section 2.3.2, and parameters including R_{ct}, $R_{contact}$, capacitance, and characteristic frequency were extracted from the fits. Some electrodes were also used to make XPS samples to probe the composition of the SEI. The XPS sample preparation process is described in Section 2.5.1.

Table 4.1 shows the matrix of formed and cycled pouch cells used in this study. Each row in the table corresponds to one pouch cell. The electrolyte additive, upper voltage limit, and voltage at disassembly are indicated for all cells. For cycled cells, the number of cycles and the capacity retention after cycling is indicated. Symmetric cells and full coin cells were made from all pouch cells in Table 4.1 and underwent temperature dependent EIS. Raw EIS data for (+/+), (-/-) and (+/-) cells at four of the eight measured temperatures can be found in Appendix B.4 for every cell in Table 4.1. Cells with a check mark in the 'XPS' column are cells whose electrodes also underwent XPS analysis. Tables summarizing the cells in each results section are shown at the beginning of the sections.

Table 4.1: Matrix of all formed and cycled pouch cells presented in this chapter.

Additive	Formed/Cycled	Formed/Cycled to (V)	Voltage at disassembly (V)	No. of cycles	Capacity retention	XPS
Control	formed	4.2	4.2	---	---	
			3.8	---	---	✓
		4.4	4.4	---	---	
			3.8	---	---	
2% VC		4.2	4.2	---	---	
			3.8	---	---	✓
		4.4	4.4	---	---	
			3.8	---	---	
1% LFO		4.2	4.2	---	---	
			3.8	---	---	✓
		4.4	4.4	---	---	
			3.8	---	---	
Control	cycled	4.2	3.8	722	80.6	✓
		4.4		322	80.9	
2% VC		4.2		392	99.1	
				677	97.4	✓
		4.4		385	97.8	✓
1% LFO		4.2		383	98.6	
				683	97.7	✓
		4.4		384	98.2	
				678	98.6	

4.2 Results and Discussion

4.2.1 Comparison of Cells After Formation

Table 4.2 shows the matrix of cells in this comparison. All cells were disassembled after formation. The upper voltage limit for the formation protocol, the final voltage of the formation protocol, and the actual voltage at disassembly are shown. The cells containing 2% VC and 1% LFO intended to do formation to 4.2 V and measurements at TOC were formed to 4.3 V instead, as shown in the Table.

Table 4.2: Matrix of formed pouch cells presented in this comparison.

Additive	Formed/Cycled	Formed to (V)	Final voltage (V)	Actual voltage at disassembly (V)
Control		4.2	4.2	4.13
			3.8	3.78
		4.4	4.4	4.30
			3.8	3.78
2% VC	formed	4.3	4.3	4.25
		4.2	3.8	3.80
		4.4	4.4	4.32
			3.8	3.79
1% LFO		4.3	4.3	4.24
		4.2	3.8	3.80
		4.4	4.4	4.32
			3.8	3.79

Figure 4.1 shows Nyquist plots measured at 10°C for (-/-) and (+/+) cells with all three electrolyte systems. Different colors indicate different cell formation protocols. Figure 4.1 (a-c) show that $R_{contact}$ is similar across all (-/-) cells, and Figure 4.1 (d-f) also do not show significant changes in $R_{contact}$ for (+/+) cells. Figure 4.1 (c) shows that the negative electrode R_{ct} is smaller for cells containing 1% LFO electrolyte additive. Figure 4.1 (a) and (b) are similar, suggesting that there is not a large difference in negative electrode R_{ct} after formation for cells with control electrolyte compared to control + 2% VC electrolyte. SOC had a minor impact on R_{ct} of (-/-) cells, with cells formed to 4.4 V and measured at TOC having the smallest R_{ct} and cells formed to 4.4 V and measured at 3.8 V having the largest R_{ct}.

Figure 4.1 (d) and (f) show similar R_{ct} for (+/+) cells with control electrolyte and control + 1% LFO electrolyte. SOC had a minor impact on R_{ct} in these cells. Figure 4.1 (e) shows the biggest

differences. Cells with control + 2% VC electrolyte formed to 4.3 V and measured at TOC and formed to 4.2 V and measured at 3.8 V have noticeably larger positive electrode R_{ct} than cells with the other electrolytes. In contrast, 2% VC cells formed to 4.4 V measured at TOC and at 3.8 V show similar R_{ct} to other electrolytes. R_{ct} and $R_{contact}$ values extracted from EIS fitting will be compared at multiple temperatures in future figures.
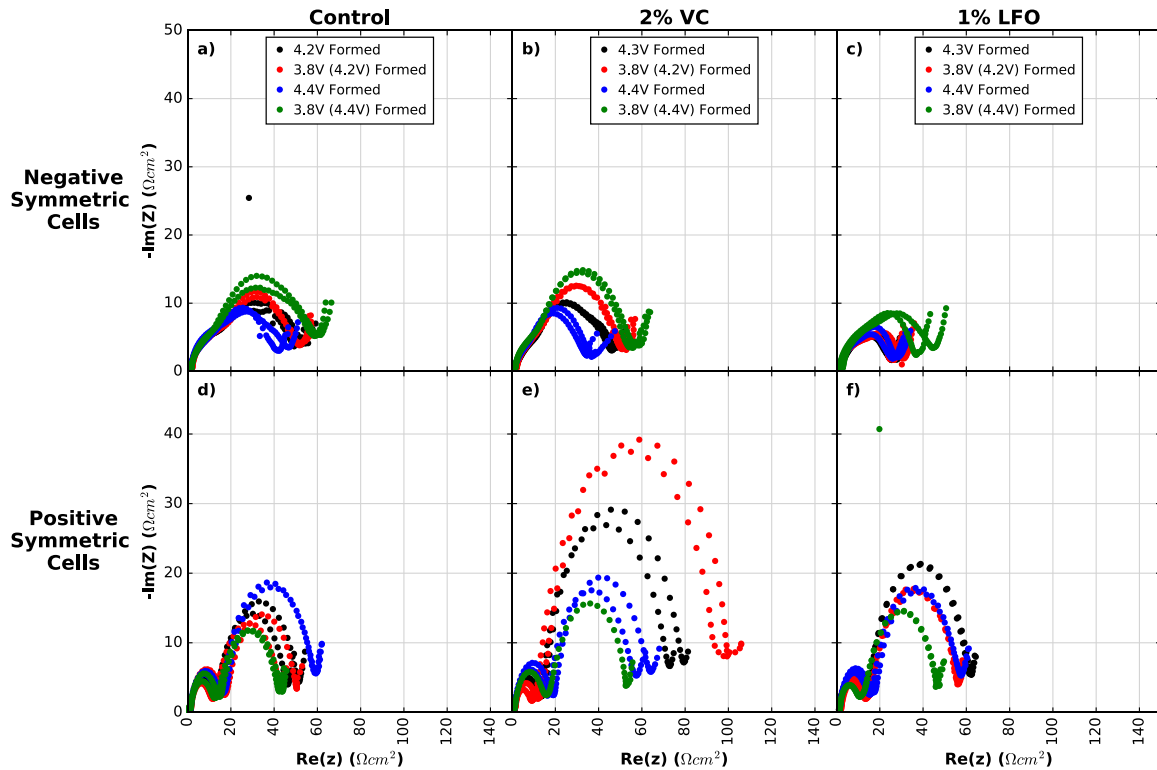
Figure 4.1: Nyquist plots of symmetric cells from formed pouch cells disassembled at different SOC and measured at 10°C. (a) and (d) show cells with control electrolyte; (b) and (e) show cells with control + 2% VC electrolyte; (c) and (f) show cells with control + 1% LFO electrolyte. (a-c) show (-/-) cells and (d-f) show (+/+) cells. Legends indicate the voltage at disassembly and indicate the TOC voltage in brackets if different than the voltage at disassembly. Duplicate cells are shown for every cell type except for '3.8 V (4.4 V) Formed' in (e).

Figure 4.2 shows the linear relationship between the logarithm of R_{ct} and the inverse of temperature for (-/-) and (+/+) cells made from pouch cells at different SOC after formation. R_{ct} increases exponentially with decreasing temperature following the Arrhenius equation (Equation 2.19).

Activation energy values and errors calculated from this data are indicated in the legends in Figure 4.2. Linear regression was used to fit the data and errors were calculated based on the standard deviation of the slope found by the fit. As discussed, E_a represents the barrier to lithium ions hopping from site to site through the negative or positive electrode SEI, which should be affected by SEI composition. E_a values range from 0.51 to 0.72 eV for the negative electrodes. Formation protocol does not appear to have a significant effect on E_a values; however, there are some noticeable differences between E_a values for the negative electrode with different electrolytes. Average E_a and standard deviation (in brackets) across all formation protocols for (-/-) cells were: 0.60 (0.01) eV, 0.67 (0.04) eV, and 0.54 (0.02) eV for control, control + 2% VC, and control + 1% LFO electrolytes, respectively. These numbers indicate that electrolyte additives do affect transport properties for the negative electrode SEI. This is consistent with reports in the literature showing that SEI composition is significantly altered by different electrolyte additives.[9,10,35,41–43] The (-/-) cells containing LFO have the lowest activation energy, suggesting that LFO-based negative electrode SEIs would have the best transport properties at low temperatures. This is consistent with the work of Liu et al. who found that 1% LFO reduced impedance in (-/-) cells after cycling.[85]

E_a values for all positive electrodes range from 0.60 to 0.72 eV. Again, different formation protocols did not significantly impact E_a. The mean and standard deviation of E_a over all formation protocols for the three electrolytes were: 0.65 (0.03) eV, 0.69 (0.03) eV, and 0.67 (0.04) eV for control, control + 2% VC, and control + 1% LFO electrolytes respectively. These values show no significant variation in positive electrode E_a between the three electrolytes. This suggests that Li^+

transport through the positive electrode SEI is not significantly affected by the electrolyte additives after formation.

An interesting case to consider is the comparison of (+/+) cells with control electrolyte and with control + 2% VC electrolyte that were formed to 4.2 V and measured at 3.8 V (red data in panels (d) and (e)). Figure 4.1 (d) and (e) showed on Nyquist plots that R_{ct} for the cells with 2% VC additive was about two times larger than the cells with control electrolyte. The SEI has been reported to be mostly lithium ethylene dicarbonate in the presence of EC,[38,86] while the addition of VC has been shown to create an SEI containing significant amounts of oligo-VC.[9,42,43] Apparently, this composition difference does not affect the activation energy for transport significantly (0.65 (0.03) eV for control, and 0.69 (0.03) eV for VC) even though there are changes in R_{ct} magnitude.

The literature reports that the composition of the SEI varies considerably between electrodes.[9,10,35,36,42] Significant differences were observed in E_a values between positive and negative electrodes for the cells containing LFO (0.53 (0.03) eV for the negative electrode and 0.67 (0.04) eV for the positive electrode). Some variation was also observed in the control cells (0.60 (0.01) eV for the negative electrode and 0.65 (0.03) eV for the positive electrode); however, cells containing VC had no significant variation between electrodes (0.67 (0.04) eV for the negative electrode and 0.69 (0.03) eV for the positive electrode). Perhaps the similarity between electrodes was related to the oligo-VC believed to be part of the SEI on both electrodes.[10,42,43]
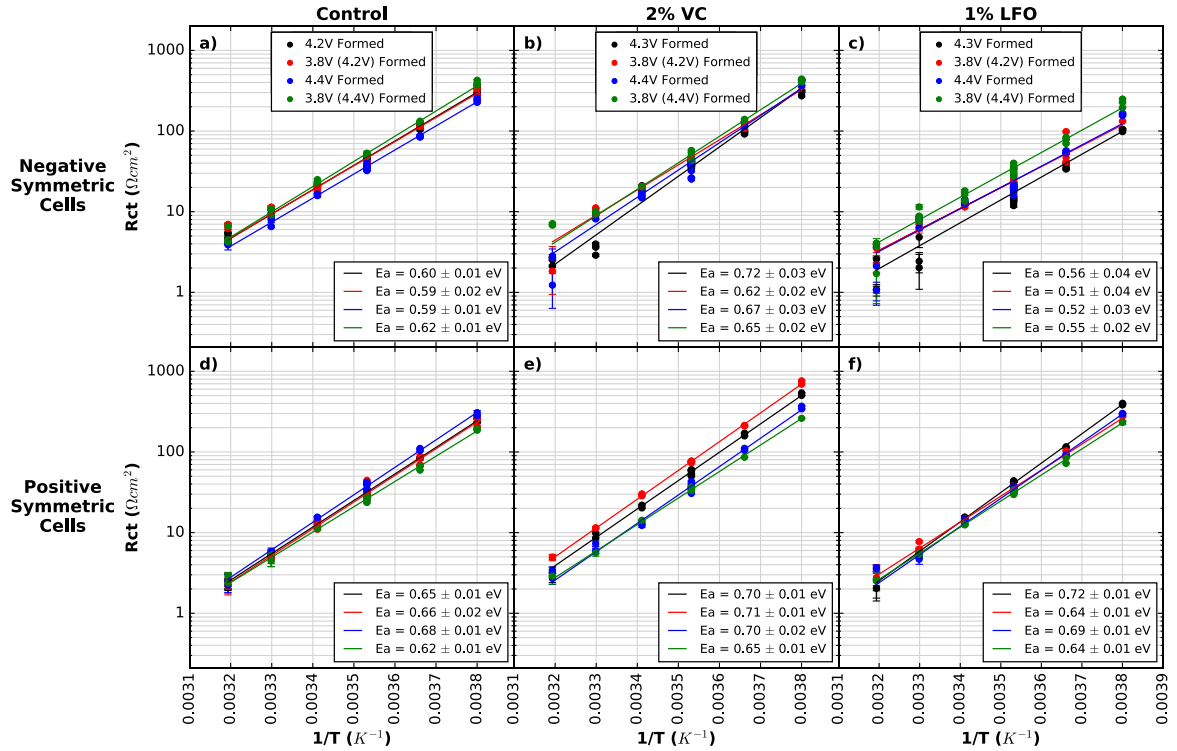
Figure 4.2: R_{ct} plotted on a logarithmic scale vs. the inverse of temperature for symmetric cells from formed pouch cells disassembled at different SOC. (a) and (d) show cells with control electrolyte; (b) and (e) show cells with control + 2% VC electrolyte; (c) and (f) show cells with control + 1% LFO electrolyte. (a-c) show (-/-) cells and (d-f) show (+/+) cells. Legends indicate the voltage at disassembly and indicate the TOC voltage in brackets if different than disassembly voltage. Duplicate and triplicate cell data is shown at each temperature, with additional points at 10ºC (0.0035 K^{-1}) due to repeat tests at that temperature. The error bars shown are the statistical error from the fitting results, however the true error in the measurement is larger than this. Points at 40ºC (0.0032 K^{-1}) were not used in the linear fit due to unreliability in EIS fitting at high temperature.

Figure 4.3 shows $R_{contact}$ vs. temperature. In contrast to R_{ct}, which varies exponentially with temperature, contact resistance is not significantly affected by temperature. Figure 4.3 (a-c) show good agreement between $R_{contact}$ values for all (-/-) cells at different SOC and with all electrolyte additives. Figure 4.3 (d-f) also show good agreement across all (+/+) cells.

68

Figure 4.3: $R_{contact}$ vs. temperature for symmetric cells from formed pouch cells disassembled at different SOC. Plot layout and comments are identical to Figure 4.2.

Figure 4.4 shows capacitance vs. temperature; the capacitance values in Figure 4.4 were calculated using Equation 2.20. The capacitance is believed to represent the capacitance of the double layer across the SEI, as described in Section 2.3.2. Using the parallel plate capacitor equation (Equation 2.21) to model SEI capacitance suggests that a strong temperature dependence is not expected since neither the area of the SEI (A), the thickness of the SEI (d), or the dielectric constant of the SEI (ε) should vary with temperature for a stable SEI film. As an example, the dielectric constant of PVDF remains approximately constant in the temperature range tested in this work.[87,88] Additionally, capacitance should decrease with increased SEI thickness.

Each panel in Figure 4.4 shows consistent capacitance values over temperature. However, deviations appear at high temperatures due to difficulty in fitting spectra because of the similar

charge transfer and contact impedance magnitudes and closer characteristic frequencies at increased temperatures. It should be noted that Figure 4.4 (a-c) are on a different y-axis scale than Figure 4.4 (d-f). The capacitance of the SEI layer on the positive electrode (d-f) is about an order of magnitude greater than that on the negative electrode (a-c), suggesting that the positive electrode SEI is much thinner, provided the dielectric constant is the same. This is consistent with reports in the literature by Y. Qian et al.[35]
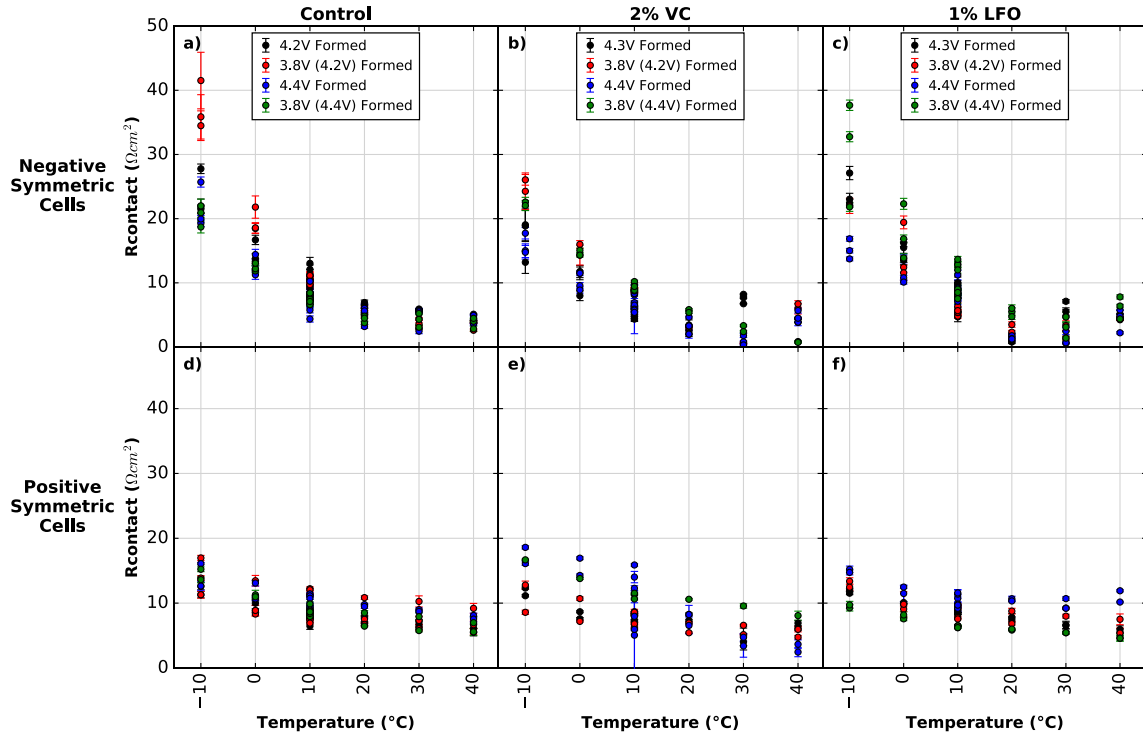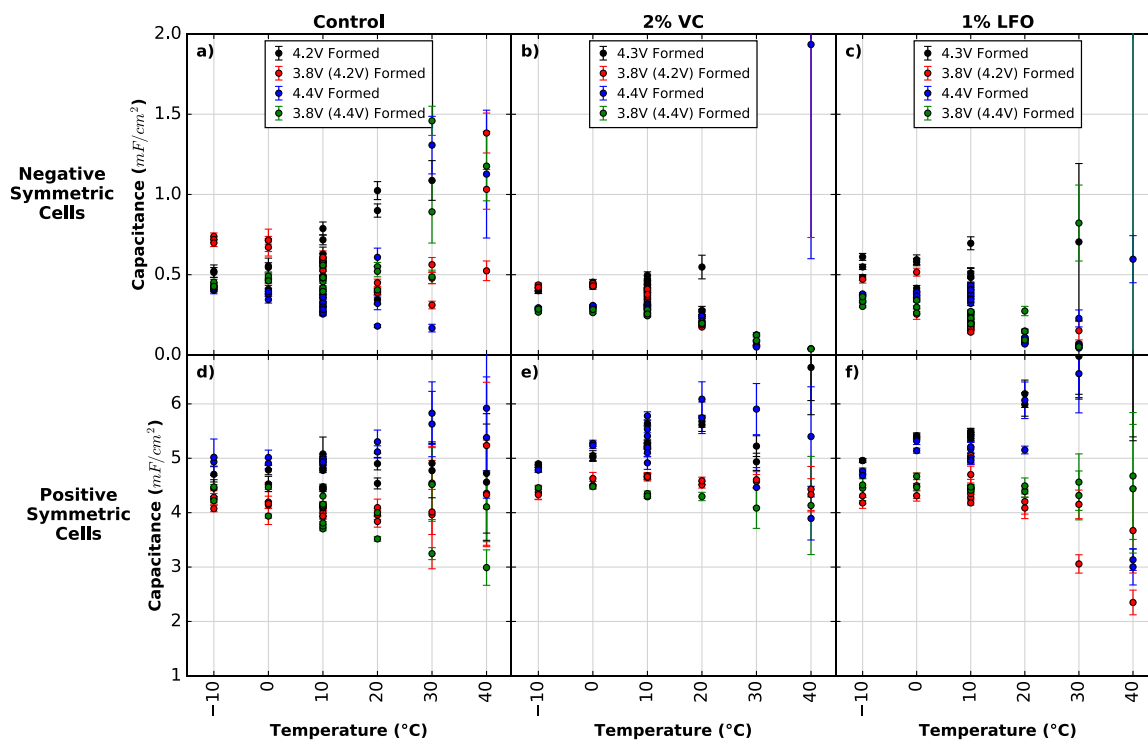

Figure 4.4: Capacitance vs. temperature for symmetric cells from formed pouch cells disassembled at different SOC. Plot layout and comments are identical to Figure 4.2. The characteristic frequencies of the charge transfer impedance semicircles that were used to calculate capacitance can be found in Appendix B.2.

4.2.2 Formed Cells vs. Cycled Cells to 4.2 V

Table 4.3 shows the matrix of cells in this comparison. All cells were formed or cycled to 4.2 V and disassembled at 3.8 V. The number of cycles and capacity retention are indicated in the Table. Cycled cells are labeled by approximate cycle number (~400c or ~700c) in future figures.

Table 4.3: Matrix of pouch cells formed and cycled to 4.2 V.

Additive	Formed/Cycled	Formed/Cycled to (V)	Voltage at disassembly (V)	No. of cycles	Capacity retention (%)
Control	formed		3.80	---	---
	cycled		3.78	722	80.6
2% VC	formed		3.78	---	---
	cycled	4.2	3.78	392	99.1
	cycled		3.83	677	97.4
1% LFO	formed		3.80	---	---
	cycled		3.77	383	98.6
	cycled		3.77	683	97.7

Figure 4.5 shows the capacity retention and ΔV growth for all cycled pouch cells in Table 4.3. Cells with the same electrolyte are shown in the same color, and pair cells show good reproducibility except for the control electrolyte cells. Only the control electrolyte cell that cycled longer was used in further tests. Figure 4.5 (a) shows that the cell with control electrolyte loses capacity much more quickly than cells with 2% VC and 1% LFO additives. Figure 4.5 (b) shows much larger ΔV growth in the cell with control electrolyte. ΔV provides an estimate of internal cell impedance, therefore this simultaneous capacity fade and ΔV growth in the control cell suggests that impedance growth significantly impacts capacity fade.
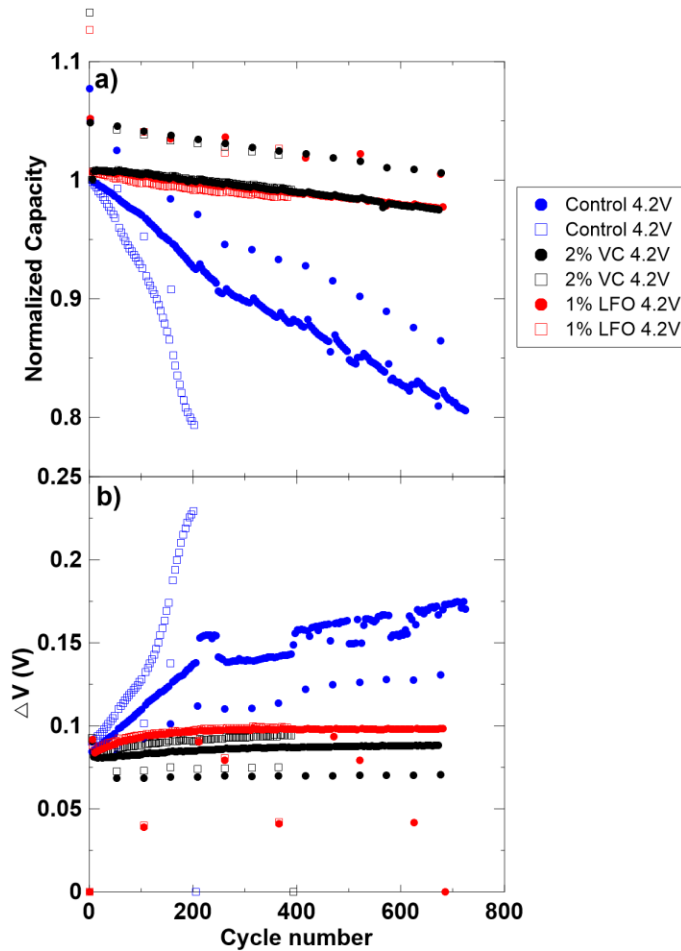
Figure 4.5: (a) Normalized capacity vs. cycle number, and (b) Δ V vs. cycle number for duplicate pouch cells containing control, control + 2% VC, and control + 1% LFO electrolytes. All cells were cycled between 3.0 V and 4.2 V.

Figure 4.6 shows 10ºC Nyquist plots for (-/-) and (+/+) cells for all cells in this comparison. Figure 4.6 (a-c) show good agreement in $R_{contact}$ across all (-/-) cells. Figure 4.6 (d-f) show minor increases in $R_{contact}$ for (+/+) cells after cycling. $R_{contact}$ will be compared more closely at all temperatures in Figure 4.8.

Figure 4.6 (a) shows that R_{ct} decreases after cycling for (-/-) cells with control electrolyte, while Figure 4.6 (d) shows that (+/+) cell R_{ct} increases significantly for control cells after cycling. The addition of the impedance from the positive electrode and the negative electrode in a control cell

72

gives an overall increase in impedance after cycling. This increase in impedance after cycling is consistent with the ΔV results for the control cell as seen in Figure 4.6 (b).

Figure 4.6 (b) shows that R_{ct} for the negative electrode changes only slightly over cycle life for cells with 2% VC additive, and Figure 4.6 (c) shows virtually no change in R_{ct} for the negative electrode in cells with 1% LFO. Negative electrode R_{ct} for 1% LFO cells is significantly smaller than R_{ct} for the 2% VC and control cells. Figure 4.6 (e) and (f) show a reduction in positive electrode R_{ct} for both 2% VC and 1% LFO cells. This suggests good SEI formation on the positive electrode in cells containing these additives. This differs from the trend for cells containing control electrolyte, in which positive electrode R_{ct} increases significantly with cycling. Section 4.2.4 summarizes R_{ct} changes with cycling.
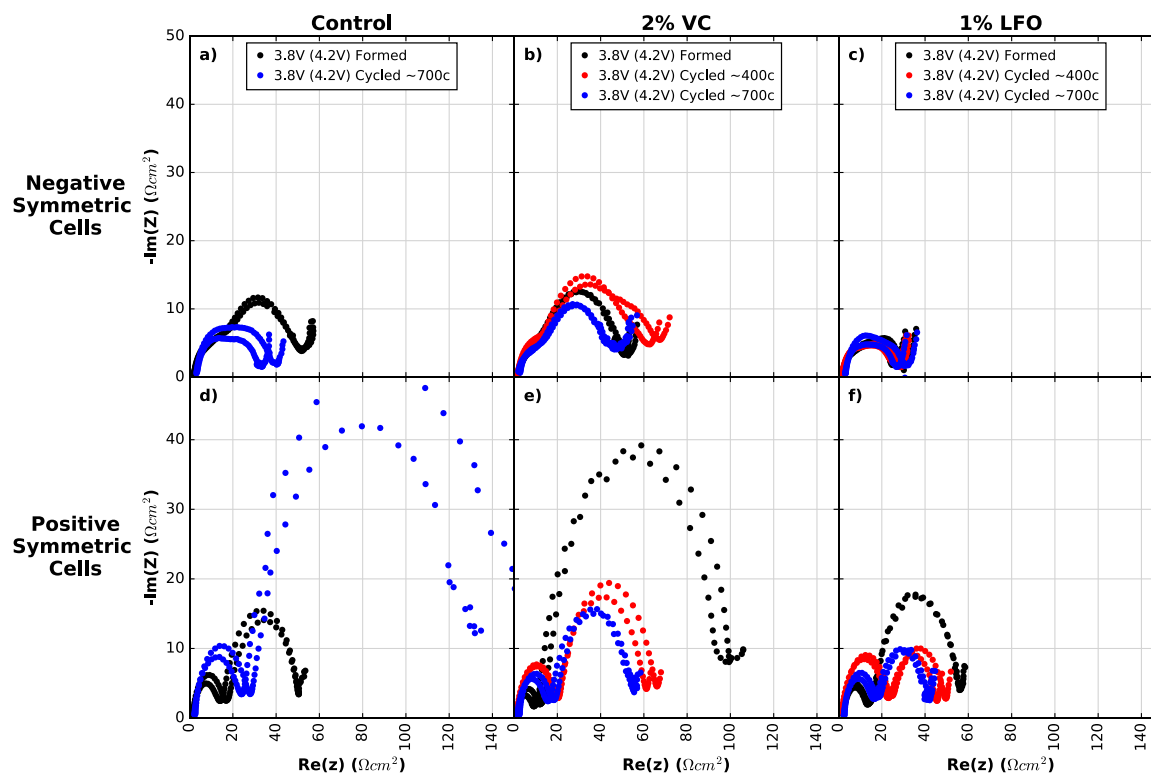
Figure 4.6: 10ºC Nyquist plots of symmetric cells from formed and cycled pouch cells with 4.2 V TOC. (a) and (d) show cells with control electrolyte; (b) and (e) show cells with control + 2% VC electrolyte; (c) and (f) show cells with control + 1% LFO electrolyte. (a-c) show (-/-) cells and (d-f) show (+/+) cells. Legends indicate the voltage at disassembly (always 3.8 V here), the TOC voltage in brackets (always 4.2 V here), and the approximate number of cycles done by the cell before disassembly. Duplicate cells are shown for every cell type.

Figure 4.7 shows the logarithm of R_{ct} vs. 1/T for all cells in this comparison. The relationship is linear for all cells, indicating that R_{ct} continues to follow the Arrhenius relationship after cycling. E_a values and errors are shown for each cell. For the negative electrode in control cells, E_a decreases from 0.59 (0.02) eV to 0.48 (0.01) eV after ~700 charge-discharge cycles. This decrease in activation energy suggests a different SEI composition with a lower energy barrier to Li^+ transport after cycling. Figure 4.6 (a) also showed that R_{ct} decreased by a factor of two after cycling in these control cells. Perhaps these decreases in R_{ct} and E_a are caused by increasing negative electrode SEI

porosity after cycling in control cells. This is discussed further below in relation to capacitance data.

Figure 4.7 (b) shows that E_a for negative electrode cells with 2% VC remains constant after ~400 cycles (0.62 (0.02) eV after formation and 0.63 (0.01) eV after ~400 cycles), and then starts to decrease after ~700 cycles (0.54 (0.02) eV). Figure 4.6 (b) showed no major changes in R_{ct} values for these cells. Figure 4.7 (c) shows that E_a remains constant after cycling for LFO cells. The mean and standard deviation across the formed cell, cell after ~400 cycles, and cell after ~700 cycles was 0.50 (0.01) eV. This suggests that cells containing LFO form the most stable negative electrode SEI.

Figure 4.7 (d) shows a significant increase in R_{ct} magnitude for the positive electrode after cycling in the cells with control electrolyte. Although the magnitude of R_{ct} changes dramatically, the slope of the line, and therefore the magnitude of E_a, remains the same which may surprise the reader. The increase in R_{ct} suggests that the SEI becomes more resistive after cycling. The similarity in E_a before and after cycling suggests similar SEI compositions on these electrodes, however, the XPS results in Figure 10 below indicate that the SEI surface composition changes after long term cycling.

Figure 4.7 (e) and (f) show changes in positive electrode E_a after cycling for cells with 2% VC and 1% LFO respectively. Figure 4.7 (e) shows that E_a decreases from 0.71 ± 0.01 eV (after formation) to 0.63 (0.04) eV after cycling (mean and standard deviation of the two cycled cells). Figure 4.7 (f) shows that E_a decreases from 0.64 ± 0.01 eV (after formation) to 0.55 (0.01) eV after cycling (mean and standard deviation of the two cycled cells with 1% LFO). These E_a decreases are

accompanied by R_{ct} decreases for the positive electrode. Figure 4.6 (e) and (f) showed that R_{ct} decrease by about a factor of two after cycling for cells containing 2% VC and 1% LFO. These decreases indicated better Li^+ transport through the positive electrode SEI after cycling, which may be due to changes in SEI composition or morphology.

The behavior of the SEI on negative and positive electrodes does appear to differ upon cycling. In control cells, E_a for the negative electrode decreased after cycling, while E_a for the positive electrode remained the same. In cells containing 2% VC, E_a for the negative electrode remained the same after ~400 cycles and then decreased after ~700 cycles, while E_a for the positive electrode decreased after ~400 cycles and then stayed the same after ~700 cycles. In cells containing 1% LFO, E_a for the negative electrode saw no change as a function of cycling, while E_a for the positive electrode noticeably decreased between formation and cycling. While the mechanisms for these differences may not be clear, the differences between the behavior of the two electrodes is consistent with reports of differing SEI composition between positive and negative electrodes. XPS results for electrode samples from these cells are examined later below.
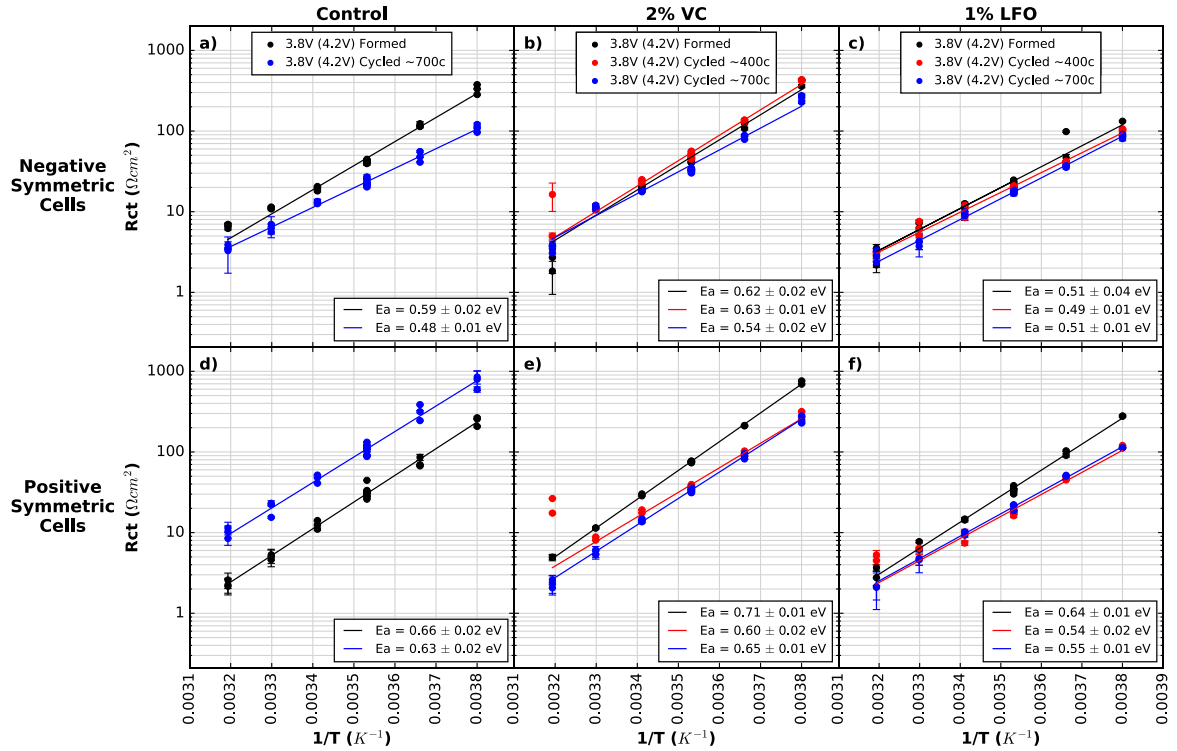
Figure 4.7: R_{ct} plotted on a logarithmic scale vs. the inverse of temperature for symmetric cells from formed and cycled pouch cells with 4.2 V TOC. (a) and (d) show cells with control electrolyte; (b) and (e) show cells with control + 2% VC electrolyte; (c) and (f) show cells with control + 1% LFO electrolyte. (a-c) show (-/-) cells and (d-f) show (+/+) cells. Legends indicate the voltage at disassembly (always 3.8 V here), the TOC voltage in brackets (always 4.2 V here), and the approximate number of cycles done by the cell before disassembly. Duplicate and triplicate cell data is shown at each temperature, with additional points at 10°C (0.0035 K⁻¹) due to repeat tests at that temperature. The error bars shown are the statistical error from the fitting results, however the true error in the measurement is larger than this. Points at 40°C (0.0032 K⁻¹) were not used in the linear fit due to unreliability in EIS fitting at high temperature.

Figure 4.8 shows $R_{contact}$ vs. temperature for the cells formed and cycled to 4.2 V in this comparison. Again, no major differences are seen across (-/-) cells. $R_{contact}$ for the (+/+) cells with control electrolyte appears to increase with cycling. However, for (+/+) cells with 2% VC and 1% LFO electrolyte additives, $R_{contact}$ appears to increase after ~400 cycles and then decrease after ~700 cycles. Differences are more prominent in cells cycled to higher voltages, which will be shown in the next section.

Figure 4.8: R_contact vs. temperature for symmetric cells from formed and cycled pouch cells with 4.2 V TOC. Plot layout and comments are identical to Figure 4.7.

Figure 4.9 shows capacitance vs. temperature for these cells. The characteristic frequencies associated with the charge transfer impedance used to calculate these capacitance values can be seen in Appendix B.2. As explained above, capacitance is not expected to change with temperature. Only small changes in capacitance are observed here over the temperature range under study (excluding unreliable high temperature data). Capacitance values are about an order or magnitude different between positive and negative electrodes, suggesting a thinner positive electrode SEI. Figure 4.9 (a) shows that the negative electrode capacitance decreases by >60% after cycling in control cells. In contrast, Figure 4.9 (b) and (c) show no changes in negative electrode capacitance in cells with VC and LFO additives. This suggests that SEI thickening is happening on the negative electrode in the control cell, which is consistent with the literature.[10,35] Since SEI thickening

78

consumes Li$^+$, this is consistent with reports of Li$^+$ inventory loss leading to capacity fade.[24,89]

Figure 4.6 (a) showed a decrease in R$_{ct}$ for the control cell after cycling, and Figure 4.7 (a) showed a decrease in E$_a$ after cycling. Perhaps this suggests a highly porous, thick SEI after cycling. Compared to a dense SEI, a porous SEI could have better Li$^+$ transport, leading to a smaller measured R$_{ct}$.

Figure 4.9 (d) shows that the capacitance of the positive electrode SEI increases slightly after cycling in control cells. This increase in capacitance would indicate a decrease in SEI thickness, which will be discussed in the next section where increases in positive electrode capacitance are larger.
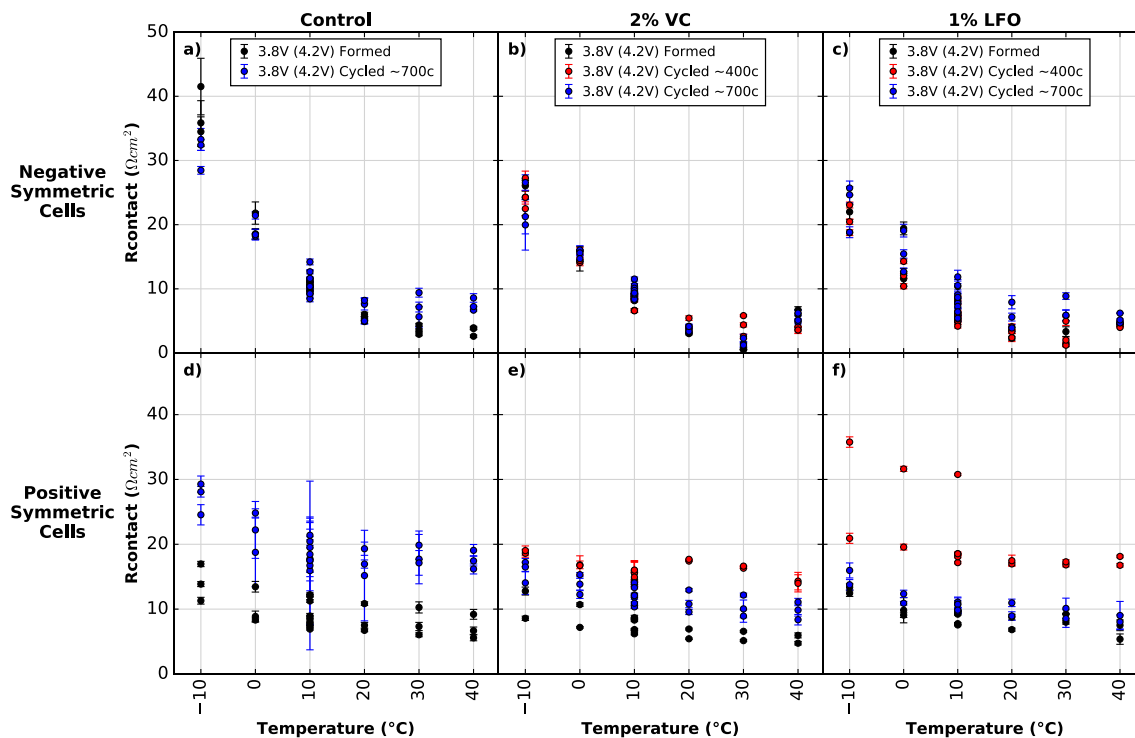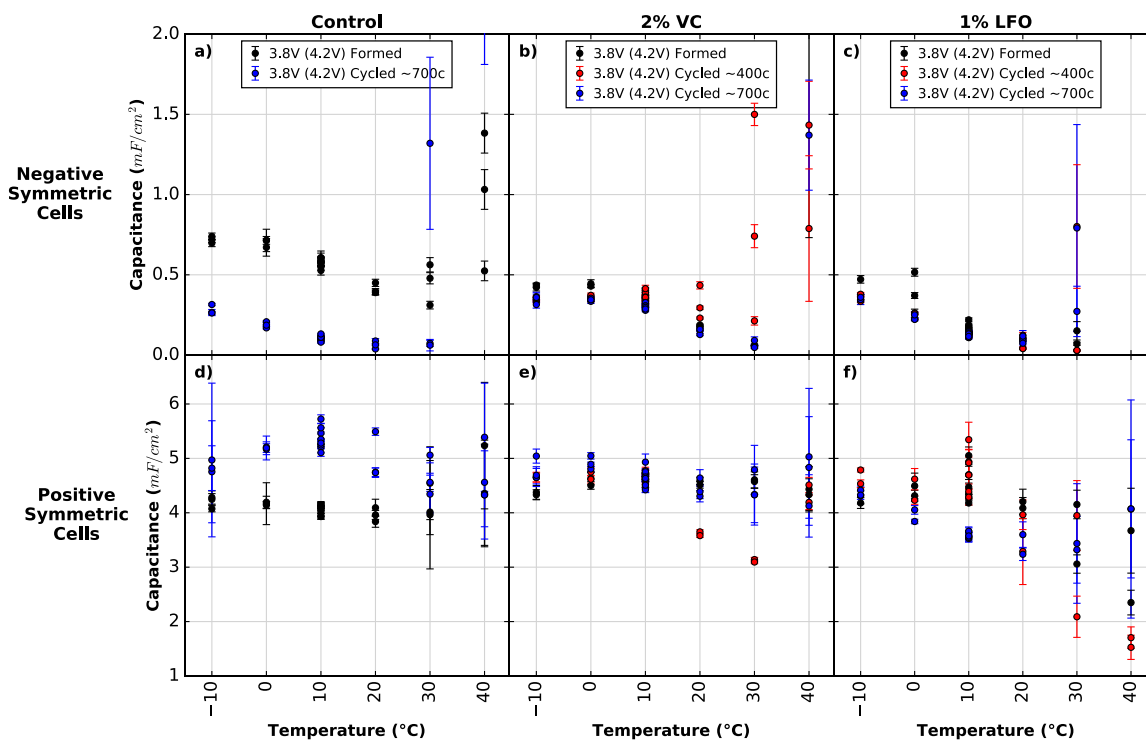

Figure 4.9: Calculated capacitance (associated with R$_{ct}$) vs. temperature for symmetric cells from formed and cycled pouch cells with 4.2 V TOC. Plot layout and comments are identical to Figure 4.7.

Figure 4.10 shows the F 1s, O 1s, C 1s, P 2p, Ti 2p, and 'TM + Li' (transition metals and lithium) XPS spectra for NMC532 electrodes. Spectra from a fresh, uncharged NMC532 electrode are shown in the top row. The following rows contain spectra from electrodes extracted from cells after formation and after ~700 cycles. These are the same cells that underwent temperature dependent EIS studies shown above in this section. All formed and cycled cells were disassembled at 3.8 V. Spectra for electrodes from control cells are shown in the second and third rows; 2% VC cells are shown in the fourth and fifth rows; 1% LFO cells are shown in the sixth and seventh rows. Note that y-axes for similar spectra are the same (i.e. all F 1s spectra, all O 1s spectra etc.), allowing for the comparison of similar peaks between spectra.

The O 1s spectra will be highlighted first. In the fresh electrode, two peaks are observed at 532 eV and 529.5 eV. The peak at 532 eV is typically assigned to surface oxygen,[10,42] and the peak at 529.5 eV is due to lattice oxygen anions in the NMC active material (shown in yellow here).[10,73] In formed and cycled cells, peaks at ~533 eV and ~531.5 eV are attributed to C-O and C=O bonds respectively. These peaks may be assigned to carbonaceous species from oxidation of electrolyte solvents at the NMC electrode.[10] These peaks increase by different amounts in all cell types after cycling.

Compared to the fresh electrode, the lattice oxygen peak reduces slightly after formation, and a significant reduction is seen after cycling for all electrolytes. The prominence of this peak is an indicator of SEI thickness. Upon SEI thickening, the active material gets covered in SEI, thus this peak signal weakens. Additionally, the Ti 2p spectra for all electrodes show two peaks which are associated with TiO_2 from the NMC electrode coating. The 'TM + Li' spectra shows Ni, Co, and Mn peaks (see Table 2.2) from the NMC active material. The TiO_2 and TM peaks are significantly

smaller after cycling, in agreement with the decrease in the lattice oxygen peak. The magnitudes of both the lattice oxygen and TiO_2 peaks do not differ substantially between electrolytes after cycling. This suggests that SEI thickness on the NMC532 electrode may be similar for all electrolyte systems after cycling. Major differences in cycling data for control cells compared to cells with 2% VC and 1% LFO additives were presented above for these cells. Additionally, R_{ct} magnitudes differed for (+/+) cells containing the three electrolytes after cycling. After cycling, R_{ct} of 2% VC cells was about two times larger than R_{ct} of 1% LFO cells, and R_{ct} of control cells was nearly three times larger than R_{ct} of 2% VC cells. This suggests that SEI thickness alone may not be a major contributor to impedance and to capacity fade.

An additional peak at ~534.3 eV is observed in the electrodes from 2% VC cells. This peak is associated with an oligomer of VC (oligo-VC) formed at the surface, and is highlighted in blue here.[10,42,43] This peak increases slightly after cycling, suggesting continued oligo-VC production during cycling.

Blue peaks are also shown in the C 1s spectra as they may also be associated with the production of oligo-VC. Ouatani et al.,[42] Ota et al.,[43] and Madec et al.[9,10] associated peaks around these binding energies with CO_3 and CO_2 in oligo-VC. However, it is difficult to deconvolute these peaks from other peaks in the C 1s spectrum. In the C 1s spectrum of the fresh electrode, four peaks are shown with their associated assignments. The C-C peak appears to reduce after cycling for all electrolytes. The C-F peak at ~290.8 eV is associated with the PDVF binder in the NMC electrodes and is highlighted in orange.[71,72]

In the F 1s spectrum, C-F appears around 688 eV and is also highlighted in orange.[71,72] C-F, associated with PVDF binder is the only visible peak in the fresh electrode, however, after formation and cycling, two more peaks appear in the F 1s spectra. A peak at ~687 eV is associated with fluorophosphates such as $LiPF_6$ and $Li_xPO_yF_z$ (purple).[9,73] A fluorophosphate peak is also seen in the P 2p spectra at ~137 eV.[9,73] The fluorophosphate peaks increase significantly after cycling for all electrolytes. The P 2p spectra show a second peak around 134 eV associated with phosphates (P_xO_y).[9,73] When comparing the electrodes with different additives after formation, it is clear that this P_xO_y is more prominent in the cell containing 1% LFO. After cycling, the cell with 1% LFO has the largest increase in P_xO_y.

Finally, LiF production is seen in the F 1s spectra around 685 eV (green).[9,45] LiF results from the degradation of $LiPF_6$ salt in the electrolyte[2,20] and production of LiF has been observed to increase with electrolytes containing LFO additive due to the additional fluorine.[35] Figure 4.10 shows LiF in all cells after formation, with the control cell having the most. After cycling, the control cell gains some LiF, the 2% VC cell has no visible LiF, and the 1% LFO cell has the largest LiF peak. LiF peak intensities correlate well with the Li peak intensities in the 'TM + Li' spectra.

The biggest differences in SEI composition between electrolyte additives appears to be in inorganic compounds such as fluorophosphates and LiF. The P_xO_y peak also shows differences between cycled cells with different electrolytes, and oligo-VC may be a factor in the SEI of cells containing VC additive. Figure 4.6 (d) and (f) show significantly different positive electrode charge transfer impedance after cycling for control cells and 1% LFO cells respectively. Figure 4.7 (d) and (f) showed different activation energies for cycled positive electrode control cells (0.63 ± 0.02 eV) and 1% LFO cells (0.55 (0.01) eV for both cycled cells). In contrast, XPS results in

Figure 4.10 showed small differences in the SEI composition on the NMC532 electrodes of these cells. Further research is required to determine the cause of the SEI differences.
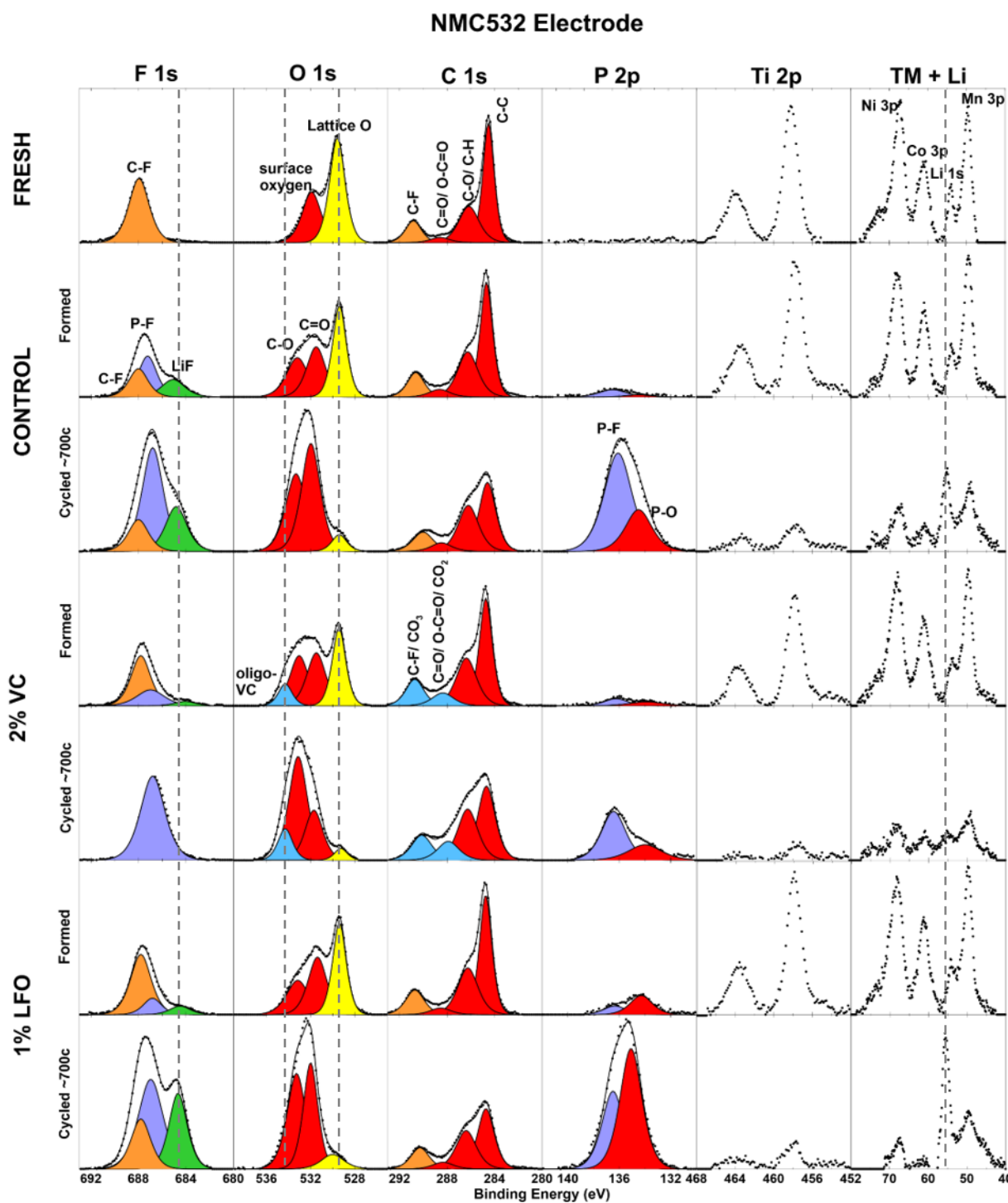
Figure 4.10: XPS data for NMC532 electrodes extracted from fresh, formed, and cycled pouch cells. Formed cells were formed to 4.2 V; cycled cells were cycled between 3.0 V and 4.2 V; all formed and cycled cells were disassembled at 3.8 V and contained control, control + 2% VC, or control + 1% LFO electrolyte. Each row contains data from one electrode sample. F 1s, O 1s, C 1s, P 2p, Ti 2p, and 'TM + Li' (all transition metals) spectra are shown. The y-axis scales are equal

for spectra of the same type (columns). Components are labeled based on BE and literature assignments.

Figure 4.11 shows the F 1s, O 1s, C 1s, and P 2p XPS spectra for the graphite (AG) electrodes. Spectra from a fresh AG electrode are shown in the top row. The following rows contain spectra from AG electrodes extracted from the same formed and cycled cells shown in Figure 4.10.

The C 1s spectrum for the fresh electrode shows a peak at 284.2 eV associated with graphite.[9,10] After formation, the graphite is lithiated, shifting the peak to ~282.5 eV.[9,10] The lithiated graphite peak is shown in dark gray. In a similar manner to the lattice oxygen peak in NMC532 electrode, the lithiated graphite peak is an indicator of SEI thickness. After formation, the 2% VC cell has the smallest lithiated graphite peak, suggesting that is also has the thickest SEI. This is in agreement with the work of Madec et al.[10] and Qian et al.[35] After cycling, the lithiated graphite peak is no longer observed for all electrolytes, indicating that the SEI is too thick for the photoelectrons to penetrate from below the SEI on the electrode. A minor increase in the C-O/C-H peak and a more significant decrease in the C-C peak is observed after cycling for all electrolytes. Again, peaks that may be associated with oligo-VC are shown in blue. In the C 1s spectra, it is difficult to distinguish these peaks from C-F and C=O peaks. However the additional peak in the O 1s spectra at ~534.5 eV is apparent for cells with 2% VC, suggesting the presence of oligo-VC in the SEI. The O 1s spectra contain two peaks associated with carbonaceous species from the decomposition of solvents on the graphite electrode.[10,42] In both control and 1% LFO cells, the C-O peak increases significantly after cycling.

Fluorophosphates appear in all F 1s and P 2p spectra after formation (purple). The cell with 2% VC initially has more P-F than control and 1% LFO cells, but the P-F peaks increase to roughly

the same magnitude in all electrolyte systems after cycling. P-O peaks also begin with different intensities after formation with the 1% LFO cell showing a significantly larger peak. P-O peaks also increase to roughly the same magnitude after cycling. Lastly, the LiF peak in the F 1s spectra is of interest. After formation, LiF appears with different intensities following: 2% VC > control > 1% LFO. After ~700 charge-discharge cycles, the peak intensities of LiF follow: 1% LFO > control > 2% VC.

The differences in SEI composition on the graphite electrodes with different electrolyte additives after cycling include differences in: LiF content, C-O content, C-C content, and oligo-VC for the cell containing VC. Figure 4.6 showed that the 2% VC cell had the largest negative electrode R_{ct} after cycling, while the control and 1% LFO cells had similar, smaller negative electrode R_{ct}. Qian et al. have suggested that inorganic compounds, such as LiF, create SEIs with lower impedance by lowering the energy barrier and favoring Li^+ diffusion.[35] Figure 4.11 shows higher LiF content in control and 1% LFO negative electrode SEIs after cycling. Figure 4.7 also showed low E_a for control (0.48 ± 0.01 eV) and 1% LFO cells (0.50 (0.01) eV) after cycling. Along with the small R_{ct} measurements, this may support Qian et al.'s hypothesis.
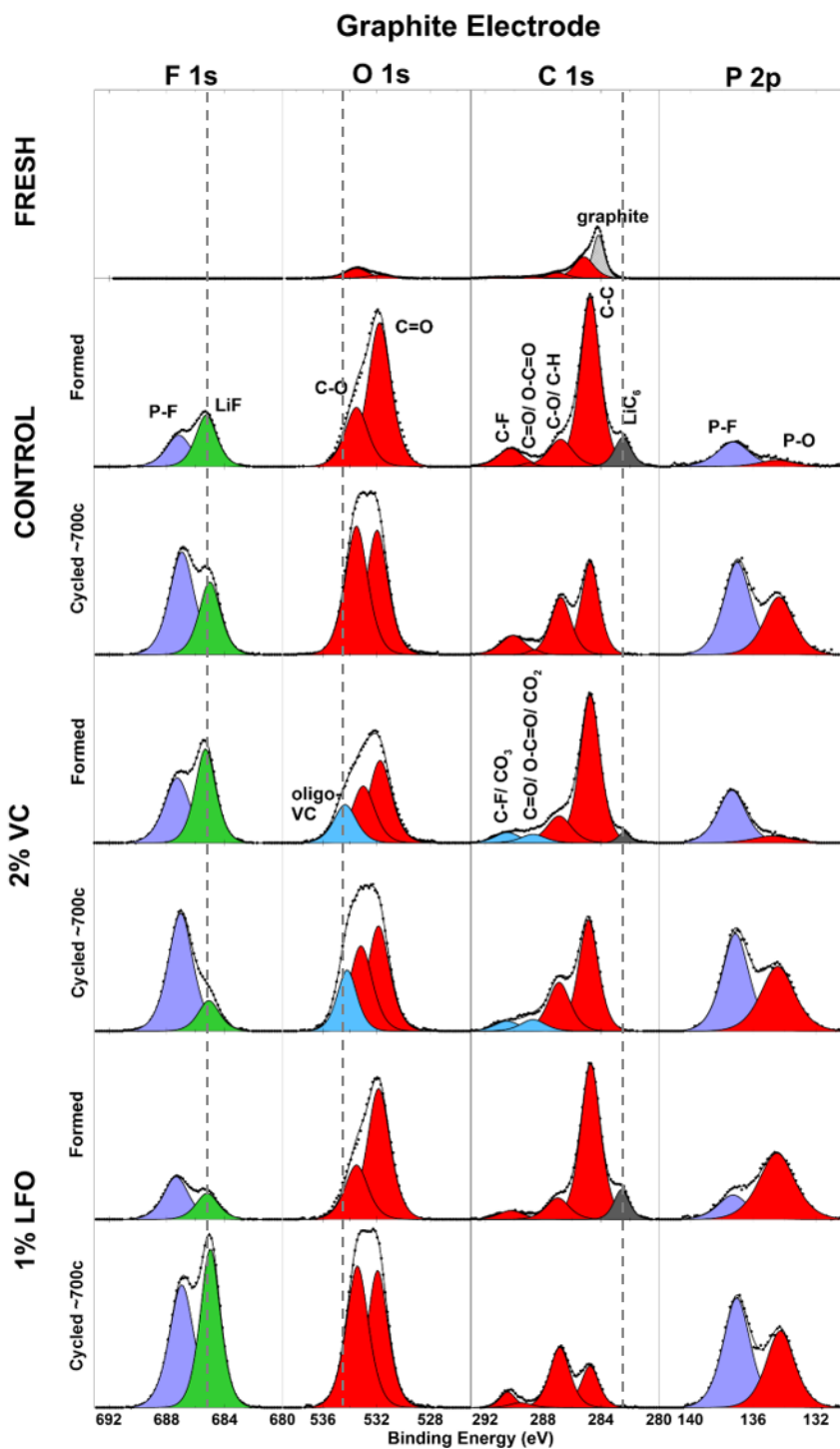
Figure 4.11: XPS data for graphite electrodes extracted from fresh, formed, and cycled pouch cells. Formed cells were formed to 4.2 V; cycled cells were cycled between 3.0 V and 4.2 V; all formed and cycled cells were disassembled at 3.8 V and contained control, control + 2% VC, or control + 1% LFO electrolyte. F 1s, O 1s, C 1s, and P 2p spectra are shown. The y-axis scales are equal for spectra of the same type (columns). Components are labeled based on BE and literature assignments.

4.2.3 Formed Cells vs. Cycled Cells to 4.4 V

Table 4.4 shows the matrix of cells in this comparison. All cells were formed or cycled to 4.4 V and disassembled at 3.8 V. The number of cycles and capacity retention are indicated in the table. Cycled cells are labeled by approximate cycle number (~300c, ~400c, or ~700c) in future figures.

Table 4.4: Matrix of pouch cells formed and cycled to 4.4 V.

Additive	Formed/Cycled	Formed/Cycled to (V)	Voltage at disassembly (V)	No. of cycles	Capacity retention (%)
Control	formed		3.78	---	---
	cycled		3.69	322	80.9
2% VC	formed		3.79	---	---
	cycled	4.4	3.71	385	97.8
1% LFO	formed		3.79	---	---
	cycled		3.74	384	98.2
	cycled		3.78	678	98.6

Figure 4.12 shows the capacity retention and ΔV growth for all cycled pouch cells in Table 4.4. Duplicate cells with 2% VC additive did not show similar capacity retention and only the better cell was studied further. Figure 4.12 (a) and (b) show rapid capacity fade and ΔV growth in the cells with control electrolyte while cells with additives have good capacity retention and minimal ΔV growth. In comparison with the cells cycled to 4.2 V in the previous section, cells containing 2% VC and 1% LFO electrolyte additives had similar capacity retention after ~400 and ~700 cycles. Cells with control electrolyte cycled to 4.4 V experienced much quicker capacity fade than similar cells cycled to 4.2 V. This increase in capacity fade is expected at higher upper cutoff potentials and has been observed by Nelson et al.,[90] Thompson et al.,[91] and Ma et al.[92] for different cell and electrolyte chemistries.
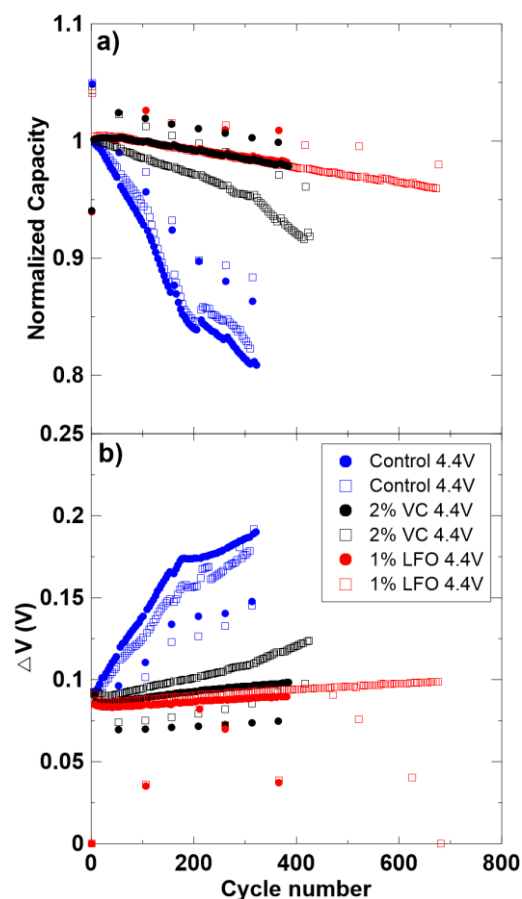
Figure 4.12: (a) Normalized capacity vs. cycle number, and (b) Δ V vs. cycle number for duplicate pouch cells containing control, control + 2% VC, and control + 1% LFO electrolytes. All cells were cycled between 3.0 V and 4.4 V.

Figure 4.13 shows 10ºC Nyquist plots of symmetric cells made from pouch cells in this comparison. Figure 4.13 (a-c) show that negative electrode R_{ct} decreases after cycling in all electrolyte systems. Again, the 1% LFO cells have the smallest R_{ct}. Figure 4.13 (a-c) also show no changes in $R_{contact}$. Figure 4.13 (d-f) show data from positive electrode symmetric cells with the three electrolyte mixtures. $R_{contact}$ does appear to show changes with cycling which will be discussed in more detail below. R_{ct} for the positive electrode with control electrolyte increases significantly after ~300 cycles. R_{ct} also increased for the positive electrode with control + 2% VC electrolyte. This is different than the 2% VC results for the 4.2 V cells, where R_{ct} decreased after

cycling. Ma et al. have observed higher impedance in full NMC111/graphite cells containing 2% VC additive cycled to 4.4 V, compared with cells cycled to 4.2 V.[92] Figure 4.13 (f) shows that the positive electrode R_{ct} for cells with 1% LFO additive initially decreases after ~400 cycles, and then increases after ~700 cycles to almost the same magnitude as after formation.
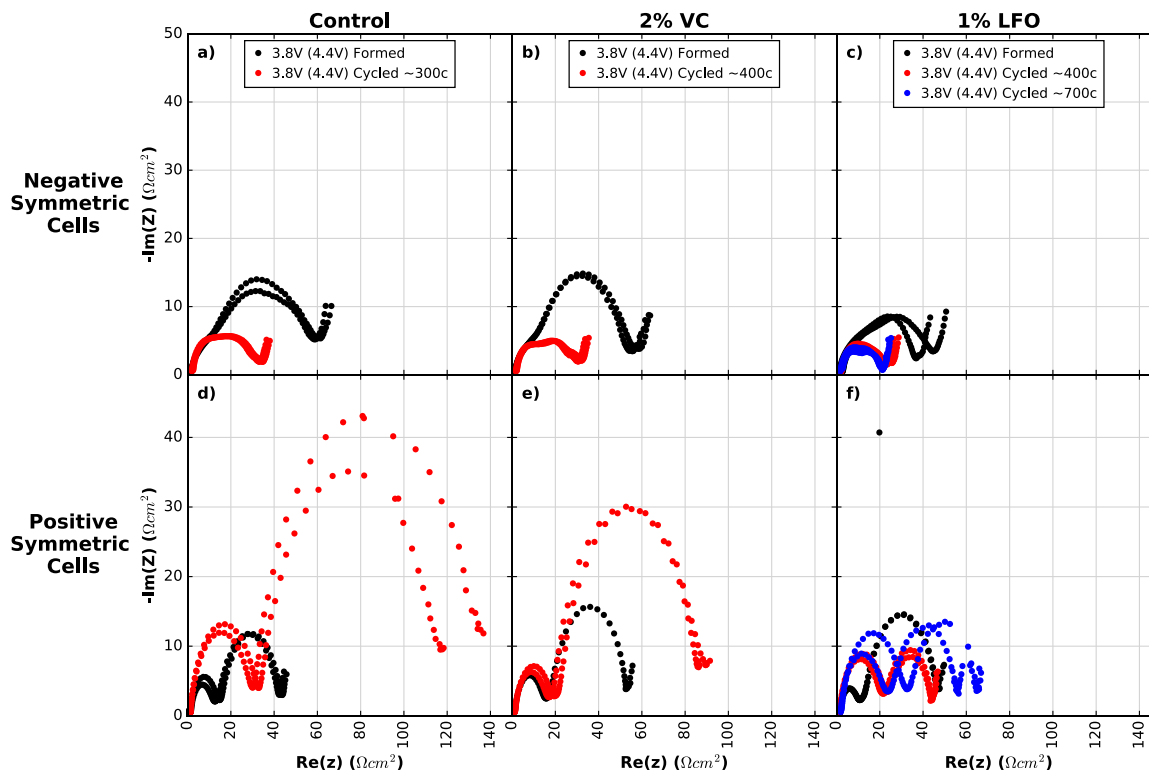

Figure 4.13: 10ºC Nyquist plots of symmetric cells from formed and cycled pouch cells with 4.4 V TOC. (a) and (d) show cells with control electrolyte; (b) and (e) show cells with control + 2% VC electrolyte; (c) and (f) show cells with control + 1% LFO electrolyte. (a-c) show (-/-) cells and (d-f) show (+/+) cells. Legends indicate the voltage at disassembly (always 3.8 V here), the TOC voltage in brackets (always 4.2 V here), and the approximate number of cycles done by the cell before disassembly. Duplicate cells are shown for every cell type except for '3.8 V (4.4 V) Formed' in (e).

Figure 4.14 shows the logarithm of R_{ct} vs. 1/T for all cells in this 4.4 V comparison. E_a values and errors are shown in each panel of Figure 4.14. In contrast to the cells cycled to 4.2 V shown in Figure 4.7, no significant changes to positive electrode E_a are seen for these 4.4 V cells with all

90

electrolytes after cycling. However, changes are seen in negative electrode E_a values after cycling for all electrolyte types. For negative electrodes, E_a reduces from 0.62 (0.01) eV (after formation) to 0.50 (0.01) eV (after ~400 cycles) in control cells; 0.65 (0.02) eV (after formation) to 0.52 (0.01) eV (after ~400 cycles) in cells with 2% VC; and 0.55 (0.02) eV (after formation) to 0.44 (0.01) eV (averaged over both cycled cells) in cells with 1% LFO. These reductions in E_a after cycling are consistent with reductions in R_{ct} after cycling in these cells, and the activation energy is lowest in cells with 1% LFO, supporting the improved transport qualities of SEIs containing LFO.

Figure 4.14 (d) and (e) show a significant increase in R_{ct} magnitude for the positive electrode after cycling in the cell with control and control + 2% VC electrolytes. However, E_a values do not differ significantly between formation and cycling. Averaged over all formed and cycled cells shown, the means and standard deviations for (+/+) cells are: 0.61 (0.01) eV for control cells, 0.65 (0.01) for control + 2% VC cells, and 0.63 (0.01) eV for control + 1% LFO cells. There are only minor differences between values for all three electrolytes, suggesting similarities in Li^+ transport through the positive electrode SEI for all three additives, despite very different R_{ct} behavior.
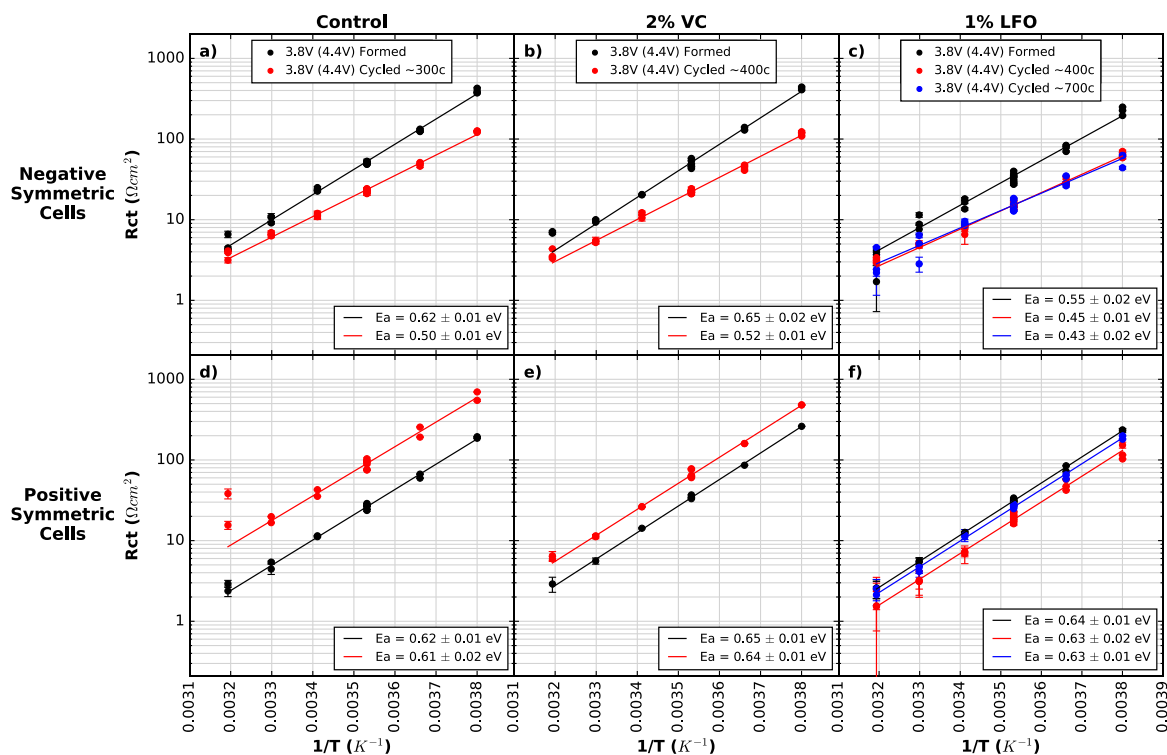
Figure 4.14: R_{ct} plotted on a logarithmic scale vs. the inverse of temperature for symmetric cells from formed and cycled pouch cells with 4.4 V TOC. (a) and (d) show cells with control electrolyte; (b) and (e) show cells with control + 2% VC electrolyte; (c) and (f) show cells with control + 1% LFO electrolyte. (a-c) show (-/-) cells and (d-f) show (+/+) cells. Legends indicate the voltage at disassembly (always 3.8 V here), the TOC voltage in brackets (always 4.2 V here), and the approximate number of cycles done by the cell before disassembly. Duplicate and triplicate cell data is shown at each temperature, with additional points at 10°C (0.0035 K^{-1}) due to repeat tests at that temperature. The error bars shown are the statistical error from the fitting results, however the true error in the measurement is larger than this. Points at 40°C (0.0032 K^{-1}) were not used in the linear fit due to unreliability in EIS fitting at high temperature.

Figure 4.15 (a-c) show that $R_{contact}$ at the negative electrode does not change significantly with cycling for any electrolyte system. Figure 4.15 (d-f) show increases in $R_{contact}$ with cycling for positive electrodes. The increase is most prominent in panel (d)—positive symmetric cells with control electrolyte. Landesfeind et al.[61] have shown increasing contact impedance with cycling in LiNi$_{0.5}$Mn$_{1.5}$O$_4$ cells (cycled to 4.9 V at 40°C). The authors suggest that loss of contact between active cathode material and the current collector occurs under aggressive cycling conditions in

these cells.[61] Atebamba et al. also suggest that volume change during repeated Li^+ intercalation may affect the distribution of active particles and conductive additives.[53] Perhaps this may lead to increased contact impedance after aggressive cycling observed here.
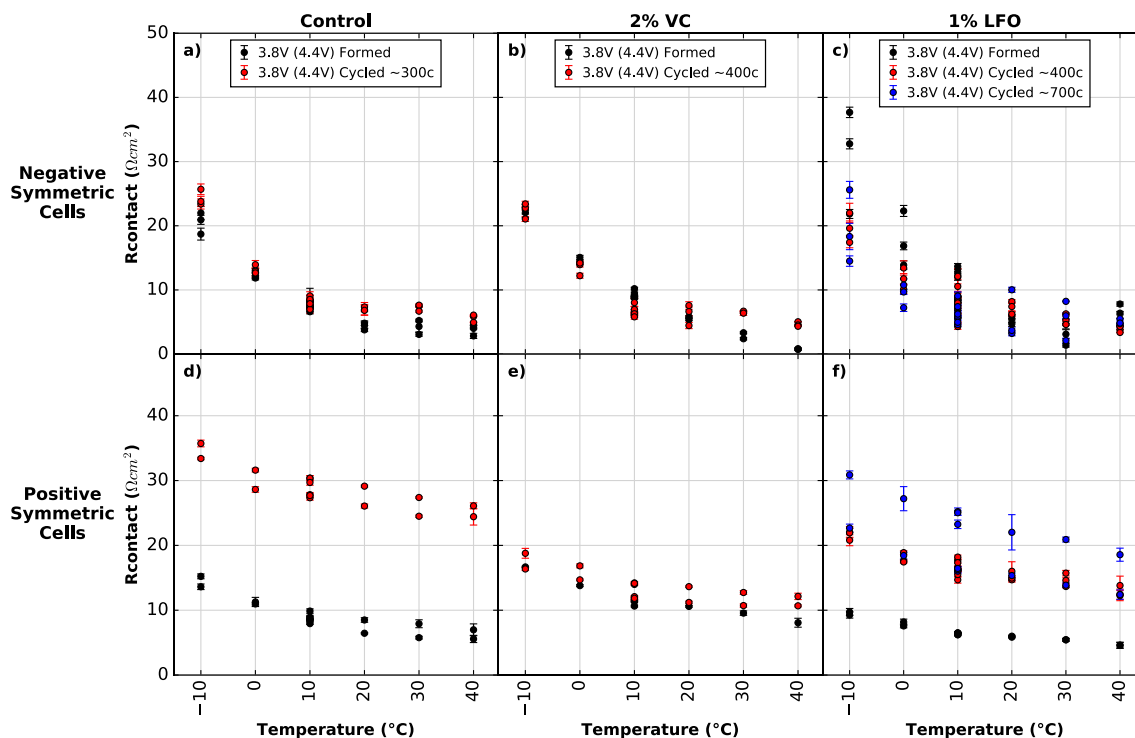

Figure 4.15: $R_{contact}$ vs. temperature for symmetric cells from formed and cycled pouch cells with 4.4 V TOC. Plot layout and comments are identical to Figure 4.14.

Figure 4.16 shows consistent capacitance values across the evaluated temperature range (excluding unreliable high temperature data). Again, positive electrode capacitance is an order of magnitude larger than negative electrode capacitance, suggesting a thinner positive electrode SEI. Panels (d) and (e) show slightly increased capacitance after cycling for positive electrode symmetric cells with control and control + 2% VC additives. This suggests somewhat thinner SEI layers after cycling, which contradicts the literature,[9,10,41] and thus capacitance measurements may be an inaccurate indicator of SEI thickness.
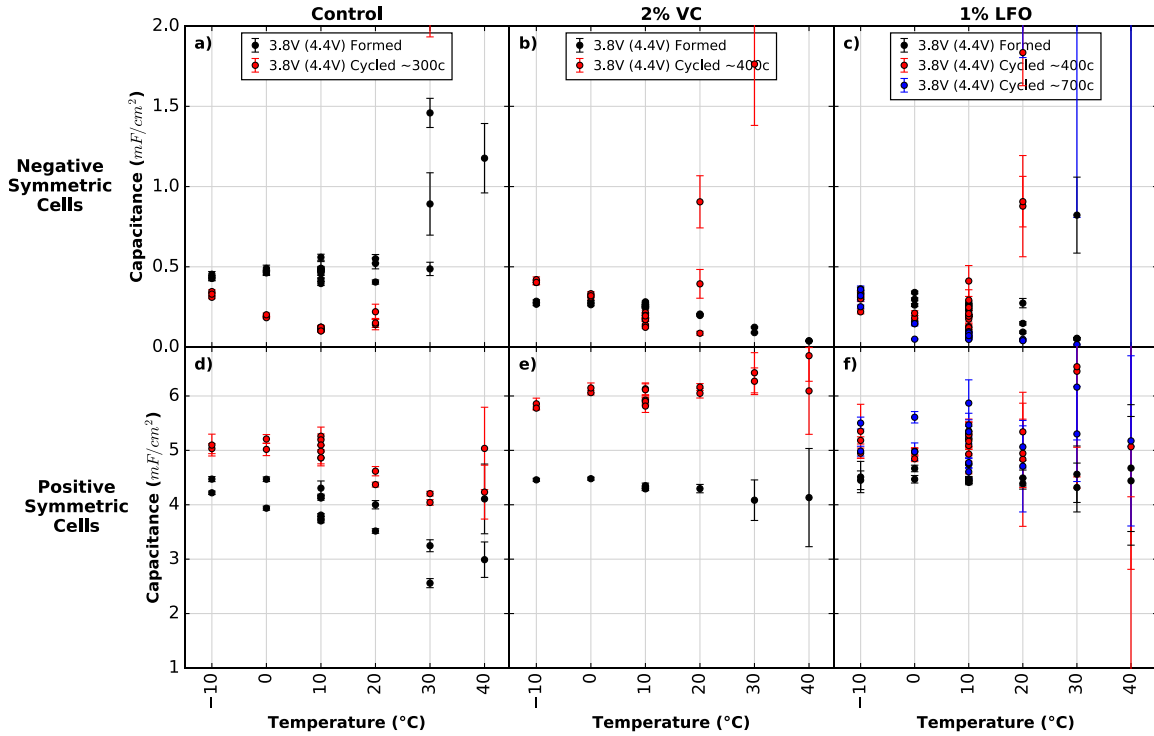
Figure 4.16: Calculated capacitance (associated with R_{ct}) vs. temperature for symmetric cells from formed and cycled pouch cells with 4.4 V TOC. Plot layout and comments are identical to Figure 4.14.

4.2.4   Summary of R_{ct} and $R_{contact}$ Over Cycle Life

Two figures are presented in this section to summarize R_{ct} and $R_{contact}$ results for all cells in this study. Figure 4.17 and Figure 4.18 show R_{ct} vs. cycle number and $R_{contact}$ vs. cycle number respectively. Only 10°C measurements are presented in these figures for simplicity. Duplicate and triplicate cells data is shown and repeat measurements at 10°C are also included.

Figure 4.17 (a-c) show generally stable or decreasing negative electrode R_{ct} values over cycling for 4.2 V and 4.4 V cells with all additives. Figure 4.17 (d) shows a significant increase in (+/+) R_{ct} after cycling in both the 4.2 V and 4.4 V cells with control electrolyte. A larger increase in impedance is observed for the cell cycled to 4.4 V, and dashed lines are shown in this plot as a

94

guide to the eye. Figure 4.17 (e) shows that (+/+) R_{ct} decreases with cycling for the 4.2 V cells with 2% VC but increases with cycling for the 4.4 V cells. This agrees with the higher impedance growth observed by Ma et al.[92] in cells containing 2% VC electrolyte additive. Figure 4.17 (f) shows stable or decreased (+/+) R_{ct} throughout cycling for the cells with 1% LFO. This data suggests that cells with 2% VC cycled to 4.2 V and cells with 1% LFO cycled up to 4.4 V suppress impedance growth over cycle life. This is consistent with the good cyclability of these cells, shown in Figure 4.5 and Figure 4.12 above.
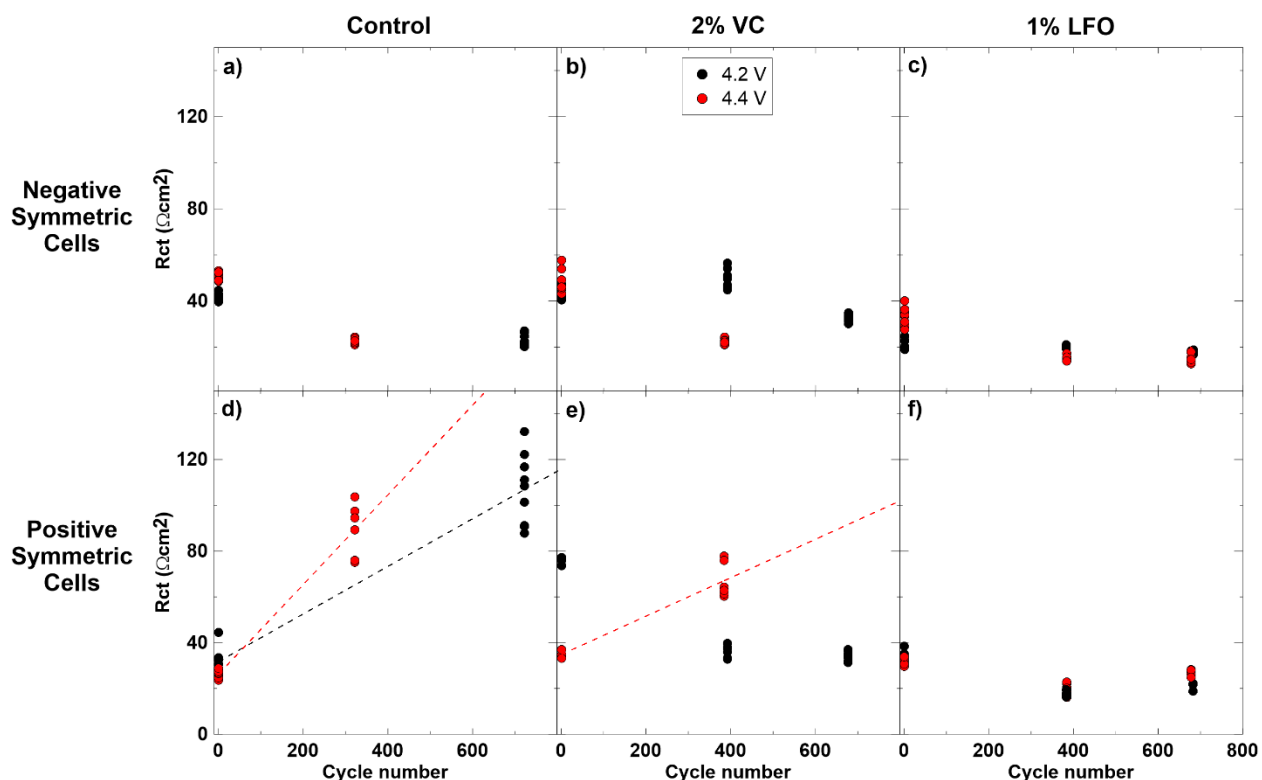

Figure 4.17: R_{ct} measured at 10°C vs. cycle number for symmetric cells from formed and cycled pouch cells with 4.2 V and 4.4 V TOC. (a) and (d) show cells with control electrolyte; (b) and (e) show cells with control + 2% VC electrolyte; (c) and (f) show cells with control + 1% LFO electrolyte. (a-c) show (-/-) cells and (d-f) show (+/+) cells. All data from repeat measurements at 10°C are shown. Plots (d) and (e) contain dashed lines as guides to the eye.

Figure 4.18 (a-c) show no significant changes in negative electrode $R_{contact}$ over cycle life for all electrolyte mixes. Figure 4.18 (d) shows increases in positive electrode $R_{contact}$ after cycling for

both the 4.2 V and 4.4 V cells containing control electrolyte. The increase is more sizeable for the 4.4 V cell after cycling. As suggested in the previous section, this may have to do with loss of contact between positive electrode active material and the current collector after aggressive cycling. Figure 4.18 (e) and (f) also show an increase in positive electrode $R_{contact}$ over cycle life for the 4.4 V 2% VC and 1% LFO cells. The trend is not the same for the 4.2 V 2% VC and 1% LFO cells which show an initial increase followed by a decrease in $R_{contact}$ over cycle life. The reason for this behavior is unclear.
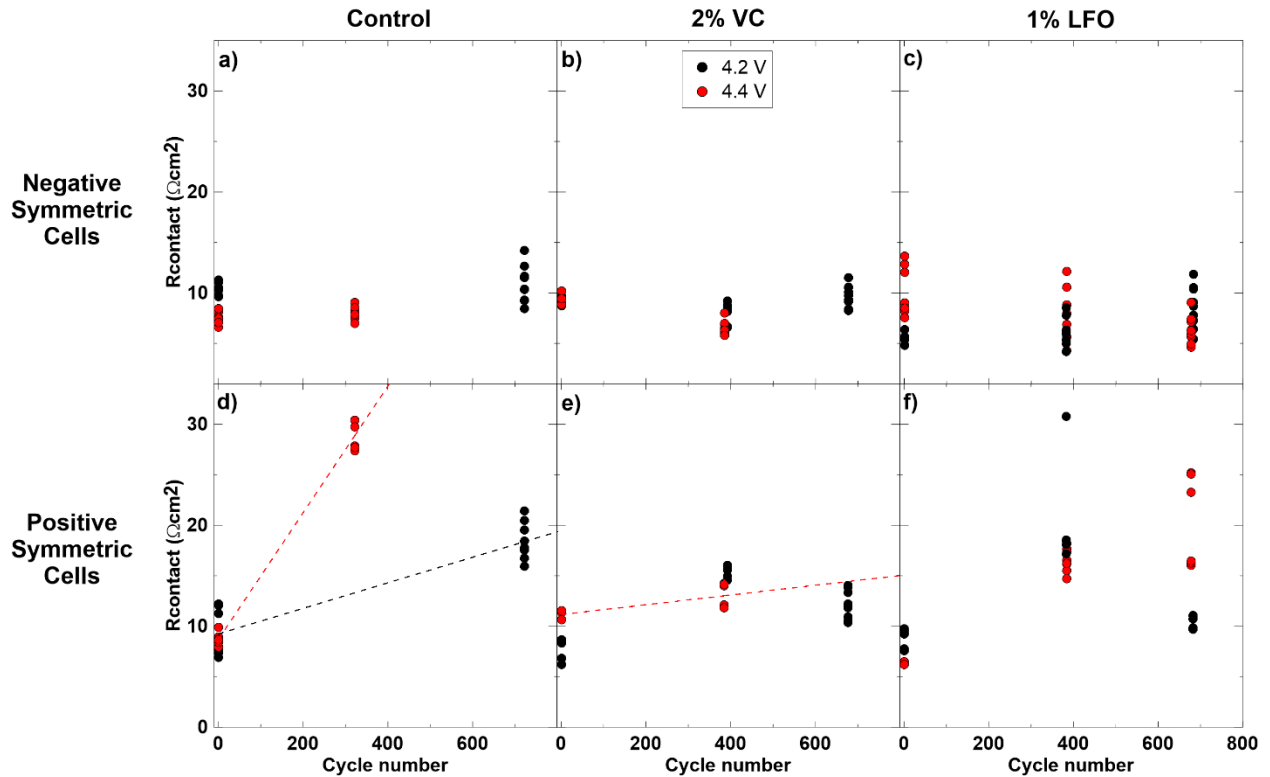

Figure 4.18: $R_{contact}$ measured at 10ºC vs. cycle number for symmetric cells from formed and cycled pouch cells with 4.2 V and 4.4 V TOC. (a) and (d) show cells with control electrolyte; (b) and (e) show cells with control + 2% VC electrolyte; (c) and (f) show cells with control + 1% LFO electrolyte. (a-c) show (-/-) cells and (d-f) show (+/+) cells. All data from repeat measurements at 10ºC are shown. Plots (d) and (e) contain dashed lines as guides to the eye.

4.2.5   Comparison of Cells with 2% VC Electrolyte Additive

A comparison of cycling data and XPS results for cells containing control + 2% VC electrolyte is presented here. Table 4.5 shows the matrix of cells in this comparison. All cells were disassembled at 3.8 V. The upper voltage limit, number of cycles, and capacity retention are indicated in the table. Cycled cells are labeled by approximate cycle number (~400c or ~700c) in future figures.

Table 4.5: Matrix of formed and cycled pouch cells containing 2% VC electrolyte additive.

Additive	Formed/Cycled	Formed/Cycled to (V)	Voltage at disassembly (V)	No. of cycles	Capacity retention (%)
	formed	4.2	3.78	---	---
2% VC	cycled	4.4	3.71	385	97.8
	cycled	4.2	3.78	392	99.1
	cycled	4.2	3.83	677	97.4

Figure 4.19 (a) shows the capacity retention and (b) shows ΔV growth for all cycled pouch cells containing 2% VC electrolyte additive in this comparison. Figure 4.19 (a) and (b) show faster capacity fade and ΔV growth in the cells cycled to 4.4 V compared to the cells cycled to 4.2 V, in agreement with work by Ma et al.[92] Nyquist plots at 10ºC, as well as $\log(R_{ct})$ vs. 1/T, $R_{contact}$ vs. temperature, capacitance vs. temperature and characteristic frequency vs. temperature plots for cells in Table 4.5 can all be found in Appendix B.3.
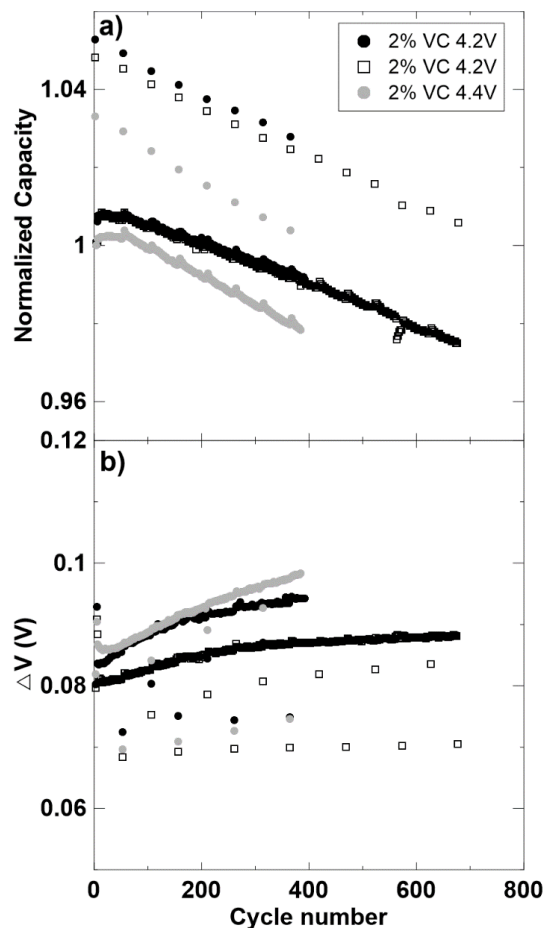
Figure 4.19: (a) Normalized capacity vs. cycle number, and (b) Δ V vs. cycle number for cells containing control + 2% VC electrolyte. Cells were cycled between 3.0 V and the TOC voltage indicated in the legend.

Figure 4.20 shows the F 1s, O 1s, C 1s, P 2p, Ti 2p, and 'TM + Li' XPS spectra for NMC532 electrodes. The first row shows spectra from a fresh NMC532 electrode; the following rows show electrodes from cells containing 2% VC electrolyte additive. The second row shows spectra from an NMC532 electrode that underwent formation to 4.2V; the third row shows an electrode from a cell cycled to 4.4 V for ~400 cycles; the fourth row shows an electrode from a cell cycled to 4.2 V for ~400 cycles; and the fifth row shows an electrode from a cell cycled to 4.2 V for ~700 cycles. The first, second, and fifth rows were presented in the 4.2 V comparison in Figure 4.10, but are included here for comparison with other VC cells. All cells were disassembled at 3.8 V.

As previously shown, the lattice oxygen peak in the O 1s spectra decreases after formation and again after cycling. In cells cycled to 4.2 V, the lattice oxygen peak suggests that the SEI continues to thicken over cycle life. The lattice oxygen peak is smallest for the cell cycled to 4.4 V ~400 times, suggesting that the SEI is thickest on this electrode. TiO_2 peaks in the Ti 2p spectra and transition metal peaks in the 'TM + Li' spectra are reduced after cycling. TiO_2 is from the electrode coating and transition metals are from the active electrode material, therefore the reduction of these peaks after cycling also supports the trend of SEI thickening during cycling.

In the F 1s spectra, the C-F peak associated with PDVF binder disappears in all cycled cells. This may point to interpretation of the high BE C 1s peak as being associated with oligo-VC rather than with C-F. In the O 1s spectra, the peak associated with oligo-VC at ~534.5 eV can be seen in all electrodes.

Fluorophosphates increase in the following order: formed < cycled to 4.2 V ~ 400c < cycled to 4.2 V ~700c < cycled to 4.4 V ~400c. LiF appears to increase slightly after ~400 cycles to 4.2 V, but then decreases and is undetectable after ~700c. In contrast, after ~400 cycles to 4.4 V, LiF increased significantly. Of the cycled cells, R_{ct} of the cell cycled to 4.4 V was largest, and Figure 4.19 showed that this cell also had the worst capacity retention and ΔV growth. The LiF formation suggests significant $LiPF_6$ decomposition on the positive electrode during high voltage cycling in VC cells.
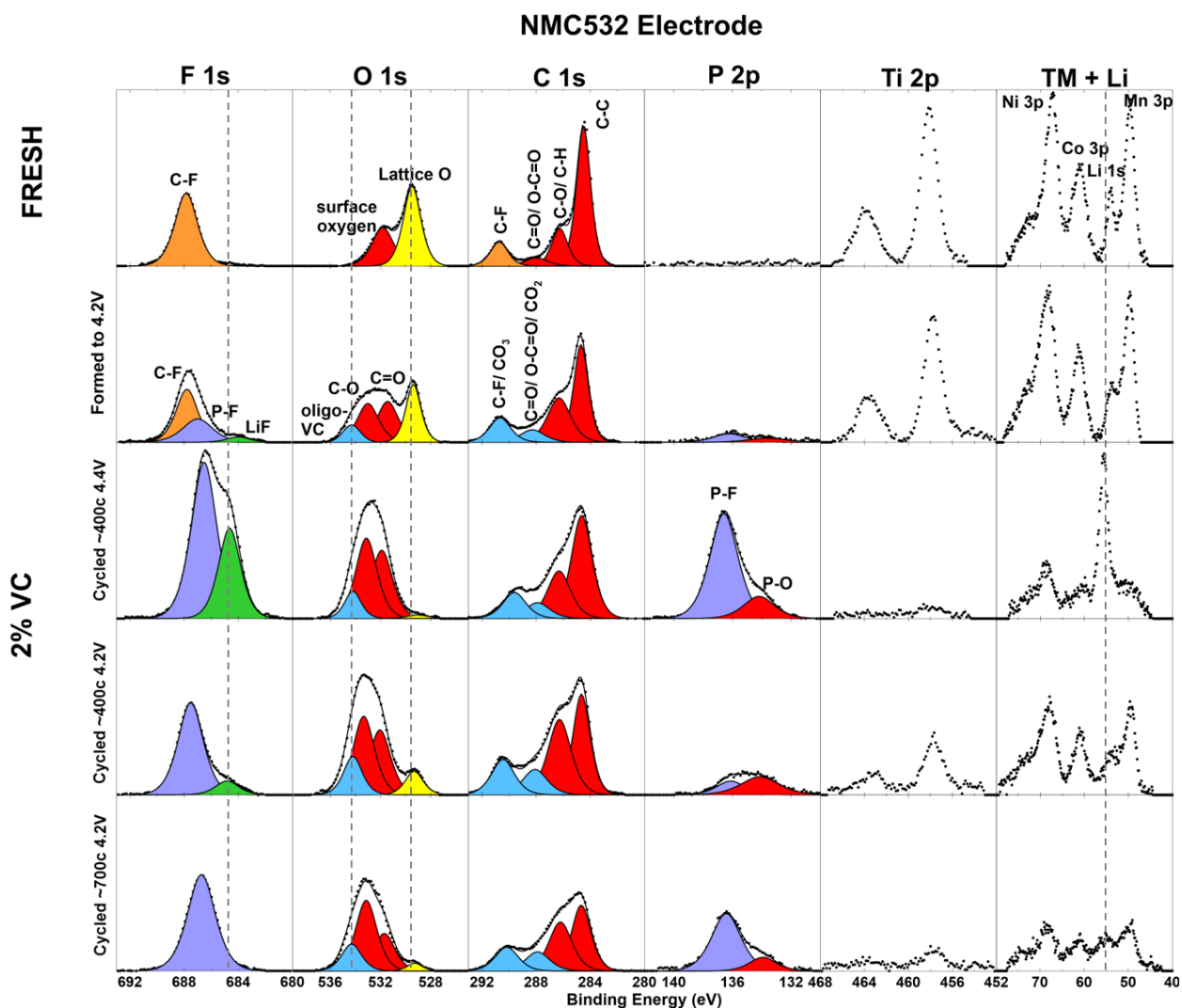
Figure 4.20: XPS data for NMC532 electrodes extracted from fresh, formed, and cycled pouch cells. Formed and cycled cells contained control + 2% VC electrolyte. Each row contains data from one electrode sample. Formation or cycling TOC is indicated to the left of each row. F 1s, O 1s, C 1s, P 2p, Ti 2p, and 'TM + Li' (all transition metals) spectra are shown. The y-axes are equal for spectra of the same type (columns). Components are labeled based on BE and literature assignments.

Figure 4.21 shows the F 1s, O 1s, C 1s, and P 2p XPS spectra for AG electrodes. The first row shows spectra from a fresh AG electrode; the following rows show electrodes from cells containing 2% VC electrolyte additive—these electrodes were from the same cells whose NMC532 electrodes were shown in Figure 4.20. Unfortunately, AG data for the cell with ~400 cycles to 4.4 V was not available, therefore only cells formed and cycled to 4.2 V are shown.

Figure 4.21 shows a decrease and then an increase in LiF and in fluorophosphates after ~400 cycles and ~700 cycles, respectively. P-O content increases between formation and ~400 cycles, but remains about the same after ~700 cycles.
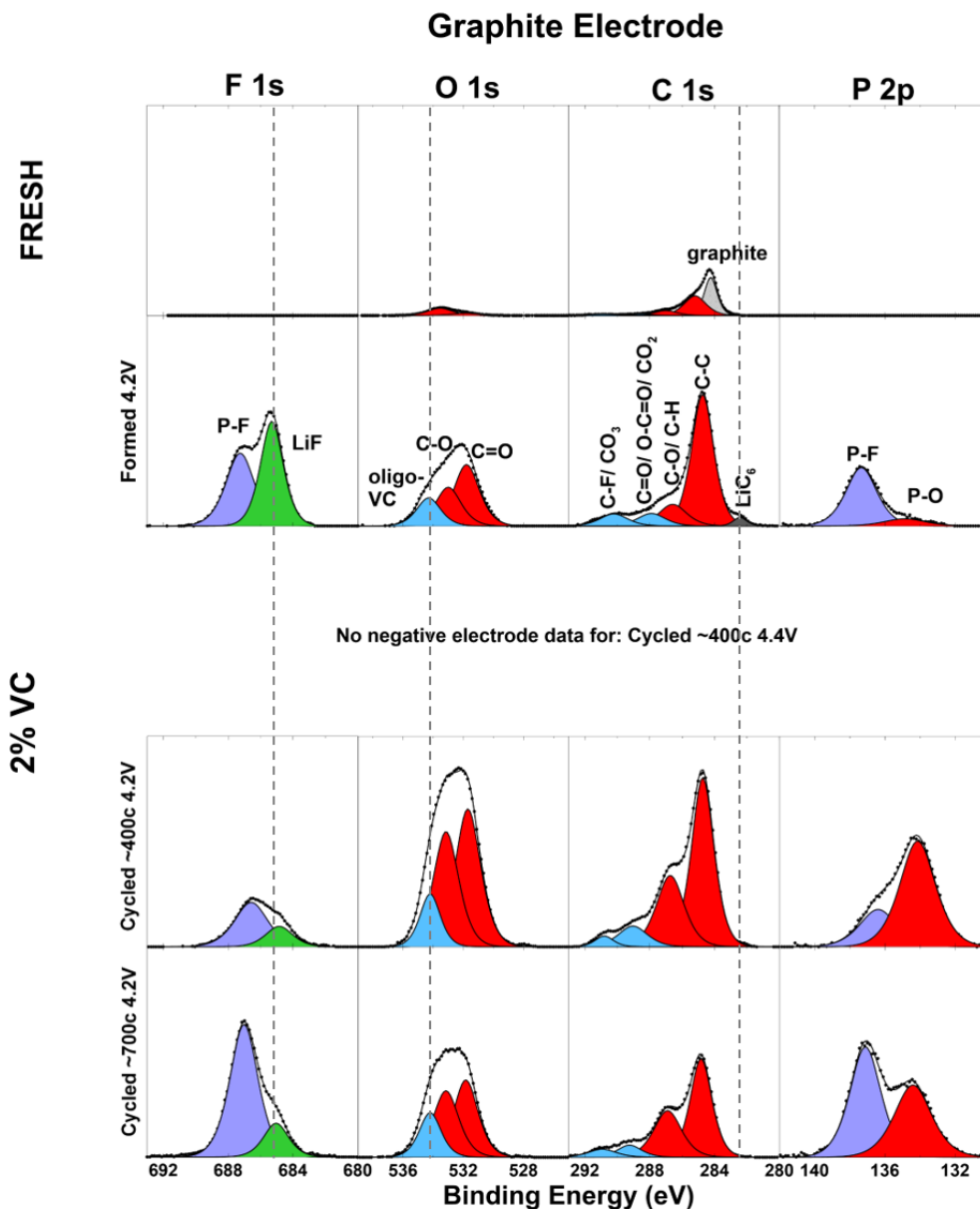

Figure 4.21: XPS data for graphite electrodes extracted from fresh, formed, and cycled pouch cells. Formed and cycled cells contained control + 2% VC electrolyte. Each row contains data from one electrode sample. Formation or cycling TOC is indicated to the left of each row. F 1s, O 1s, C 1s, and P 2p spectra are shown. The y-axes are equal for spectra of the same type (columns). Components are labeled based on BE and literature assignments.

4.3   Conclusions

This chapter has presented comparisons of cells after formation, cells formed and cycled to 4.2 V, and cells formed and cycled to 4.4 V. Cells with control, control + 2% VC, and control + 1% LFO electrolytes were studied in all comparisons. Temperature dependent EIS was performed on negative and positive symmetric cells and impedance contributions from each electrode were studied separately. XPS data was collected for negative and positive electrode samples to study the surface chemistry of the SEI. Some general conclusions may be made based on the data presented:

1. $R_{contact}$ remained consistent over cycling for negative electrodes but appeared to increase slightly over cycling for positive electrodes. This may be due to loss of electrical contact between positive electrode active particles and the current collector during aggressive cycling.

2. R_{ct} decreased or remained constant after cycling for (-/-) cells with all electrolyte systems, while R_{ct} in (+/+) cells showed different behavior based on the electrolyte additive. Impedance growth was most significant in cells with control electrolyte, which correlated well with capacity fade seen in cycling data.

3. R_{ct} as a function of temperature followed the Arrhenius relationship in all cases. Activation energies were calculated. Negative electrode E_a values were shown to vary with electrolyte additive after formation, while positive electrode E_a values did not vary significantly. After cycling, E_a either remained constant or decreased, indicating similar or better transport properties. E_a for the negative electrode decreased for all electrolytes in cells cycled to 4.4 V compared to formed cells. E_a for the positive electrode after cycling to 4.4 V did not differ from the positive electrode E_a after formation. Compared to cells after formation, E_a for the

negative electrode decreased for cells cycled to 4.2 V containing control and control + 2% VC electrolyte. Negative electrode E_a for 1% LFO cells cycled to 4.2 V remained unchanged compared to formed cells. Compared to formed cells, E_a for the positive electrode from cells cycled to 4.2 V remained constant for the control electrolyte and decreased for cells with 2% VC or 1% LFO additives. LFO-containing cells had the lowest negative electrode E_a for all tests.

4. XPS showed increasing SEI thickness for both the positive and negative electrodes after cycling. The composition of the SEI had slight variations based on electrolyte additive. The relationship between SEI composition, thickness, E_a, and R_{ct} appears to be quite complicated and requires further study.

Chapter 5: Cycling Studies of Li(Ni$_{0.5}$Mn$_{0.3}$Co$_{0.2}$)O$_2$ Symmetric Cells

5.1 Introduction

In a full Li-ion cell, parasitic reactions occur that contribute to capacity loss and impedance growth. These undesired reactions include: Li$^+$ loss due to SEI growth; electrolyte oxidation at the positive electrode; and transition metal dissolution.[89] These reactions happen at electrode/electrolyte interfaces in the cell. However, it is difficult to determine how negative and positive electrodes contribute to these reactions in a full cell because reactions at one electrode can create products which migrate to the other electrode and affect processes there. As described by Burns et al.[46], symmetric cells are a useful tool for studying electrode/electrolyte interactions at only one electrode. Symmetric cells use the same active electrode material for both electrodes, thus eliminating effects from a second active material. In this work, positive electrode symmetric cells were cycled in order to study the interactions of NMC532 with different electrolytes.

5.2 Experimental

NMC532/AG pouch cells containing control, control + 2% VC, or control + 1% LFO electrolyte underwent formation to 4.2 V or to 4.4 V, as detailed in Section 2.1.1. Cells were discharged to 3.8 V (approximately 50% SOC for these cells) for disassembly and symmetric cell construction. Positive symmetric cells were assembled from double-sided NMC532 electrodes with the same electrolyte as the parent pouch cells. Symmetric cells were cycled between +0.5 V and -0.5 V or between +0.9 V and -0.9 V at 30ºC. Cells did two cycles with a 90 μA constant current (C/45 for ±0.9 V cells; C/25 for ±0.5 V cells) and were subsequently cycled with a 180 μA constant current

(C/20 for ±0.9 V cells; C/12 for ±0.5 V cells). More details about symmetric cell assembly can be found in Section 2.1.2, and details about symmetric cell cycling can be found in Section 2.2.2.

Cells were stopped at 0.00 V periodically for EIS tests. EIS testing was done after the first two cycles and every ten cycles thereafter. All EIS tests were done at 10ºC. EIS data was fit with the equivalent electric circuit model as described in Section 2.3.1, and R_{ct} values were extracted from the fits. dV/dQ analysis was performed at the beginning and end of cycling to help determine mechanisms of capacity loss. A NMC532/Li metal half cell was used for the charge and discharge reference curves. Details about dV/dQ analysis can be found in Section 2.6.

Table 5.1 shows the matrix of positive symmetric cells in this study. Duplicate positive symmetric cells were built and cycled for each cell variation (each line in Table 5.1). Data from the better duplicate cell is shown.

Table 5.1: Matrix of all cycled positive symmetric cells in this study.

Electrolyte Additive	TOC during formation (V)	Cycling voltage limits (V)
Control	4.2	± 0.5
		± 0.9
	4.4	± 0.5
		± 0.9
2% VC	4.2	± 0.5
		± 0.9
	4.4	± 0.5
		± 0.9
1% LFO	4.2	± 0.5
		± 0.9
	4.4	± 0.5
		± 0.9

5.3   Results and Discussion

Figure 5.1 shows cycling data for all positive symmetric cells in this study. Cells cycled between ±0.9 V completed approximately 60 cycles, while cells cycled between ±0.5 V completed approximately 100 cycles. Under both formation protocols and all electrolyte systems, cells cycled between ±0.9 V at C/20 lost an average of 30% capacity (5% standard deviation). Cells cycled between ±0.5 V at C/12 lost an average of 39% capacity (6% standard deviation), excluding the cell containing VC that was formed to 4.2 V (panel b). The 2% VC cell formed to 4.2 V and cycled between ±0.5 V (panel b) lost 66% capacity.
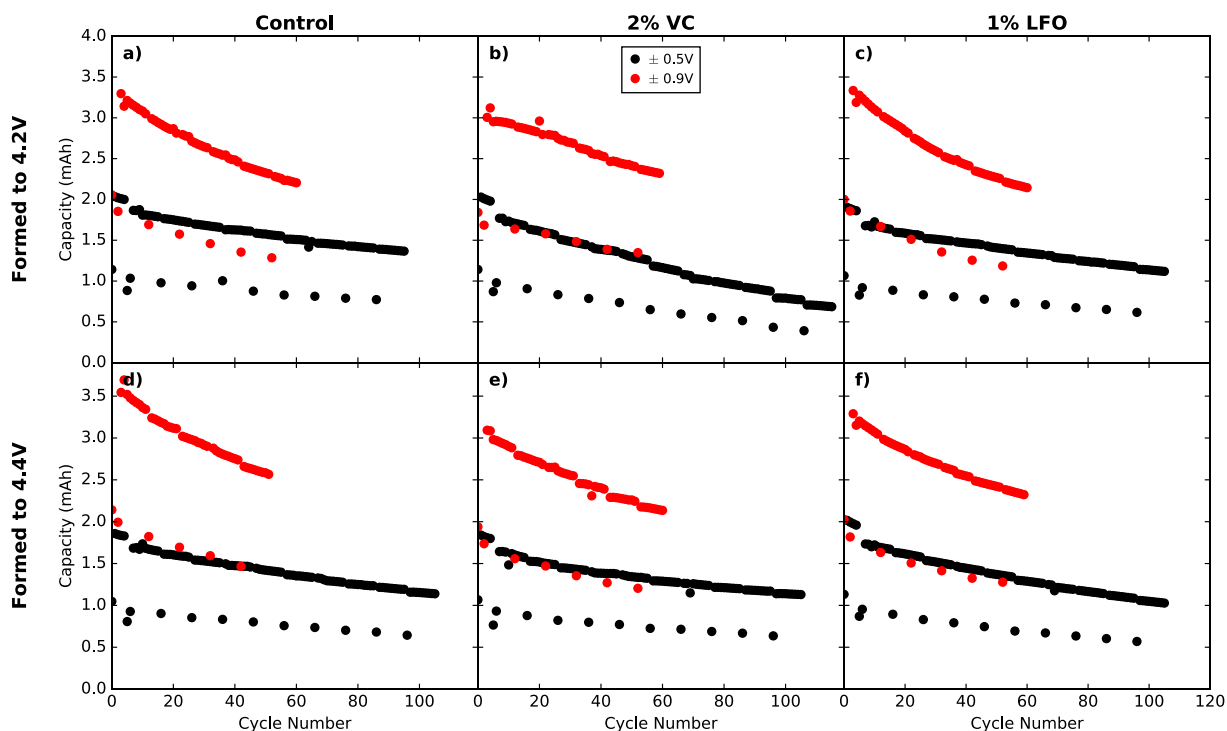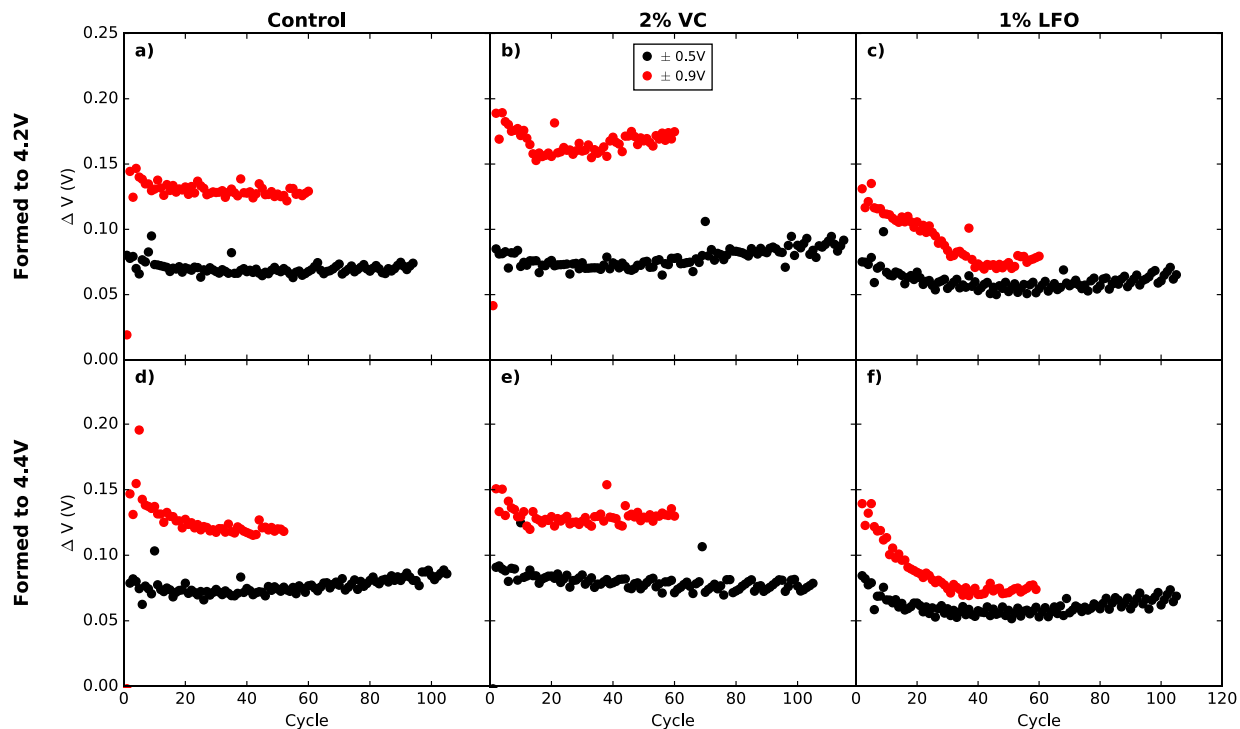

Figure 5.1: Capacity vs. cycle number for all cycled NMC532 symmetric cells. Cells cycled between ± 0.5 V are in black; cells cycled between ± 0.9 V are in red. Cells in (a-c) were made from NMC532 electrodes from pouch cells formed to 4.2 V, while (d-f) were from pouch cells formed to 4.4 V. (a) and (d) show cells with control electrolyte; (b) and (e) show cells with control + 2% VC electrolyte; (c) and (f) show cells with control + 1% LFO electrolyte.

Figure 5.2 shows ΔV vs. cycle number for each of the cells. Cells cycled between ±0.5 V (data in black) show very similar ΔV values between all cell types. In general, cells cycled between ±0.9 V (data in red) have higher ΔV than cells cycled between ±0.5 V, with panel (b) showing the largest difference between ±0.5 V and ±0.9 V data. The ±0.9 V cells containing LFO electrolyte additive (panels c and f) have a noticeable decrease in ΔV in the first ~40 cycles. ΔV subsequently stabilizes and is lower than ΔV for ±0.9 V cells with control and control + 2% VC electrolytes. This may suggest that LFO helps to reduce cell impedance at the positive electrode in high voltage cells.

Figure 5.2: ΔV vs. cycle number for all cycled NMC532 symmetric cells. Cells cycled between ± 0.5 V are in black; cells cycled between ± 0.9 V are in red. Cells in (a-c) were made from NMC532 electrodes from pouch cells formed to 4.2 V, while (d-f) were from pouch cells formed to 4.4 V. (a) and (d) show cells with control electrolyte; (b) and (e) show cells with control + 2% VC electrolyte; (c) and (f) show cells with control + 1% LFO electrolyte.

Figure 5.3 shows R_{ct} vs. cycle number for these cells. R_{ct} increases over cycle life for all cells. The cells containing VC electrolyte additive show the most significant differences. Figure 5.3 (b) shows that R_{ct} grows from ~30 Ωcm^2 to ~215 Ωcm^2 over approximately 100 charge-discharge cycles in the ±0.5 V 2% VC cell that was formed to 4.2 V. This large impedance growth may explain the 66% capacity loss seen for this cell in Figure 5.1 (b). Interestingly, Figure 5.2 (b) did not show substantial ΔV growth for this cell.

Figure 5.3 (b) and (e) also show significant R_{ct} growth in 2% VC cells cycled between ±0.9 V. This agrees with the large positive electrode impedance growth for high voltage VC-containing cells shown in Chapter 4 of this thesis. It also agrees with the large impedance growth in VC-containing full cells reported by Ma et al.[92] This large impedance growth does not appear to be accompanied by large ΔV growth for these cells and these cells also do not have larger capacity fade than the control or control + 1% LFO cells. This is consistent with the work of Nelson who showed that R_{ct} and ΔV do not correlate well in many cases.[93]

Figure 5.3 (d) and (f) show very similar trends in R_{ct} vs. cycle number for the control and control + 1% LFO cells cycled between ±0.5 V and between ±0.9 V from cells formed to 4.4 V. Cycling data and ΔV data was also very similar with the exception of the lower ΔV for the ±0.9 V LFO cell. Figure 5.3 (a) and (c) also show similar trends between control and control + 1% LFO cells, although R_{ct} is larger in the LFO-containing cells, despite seeing lower ΔV for these cells.
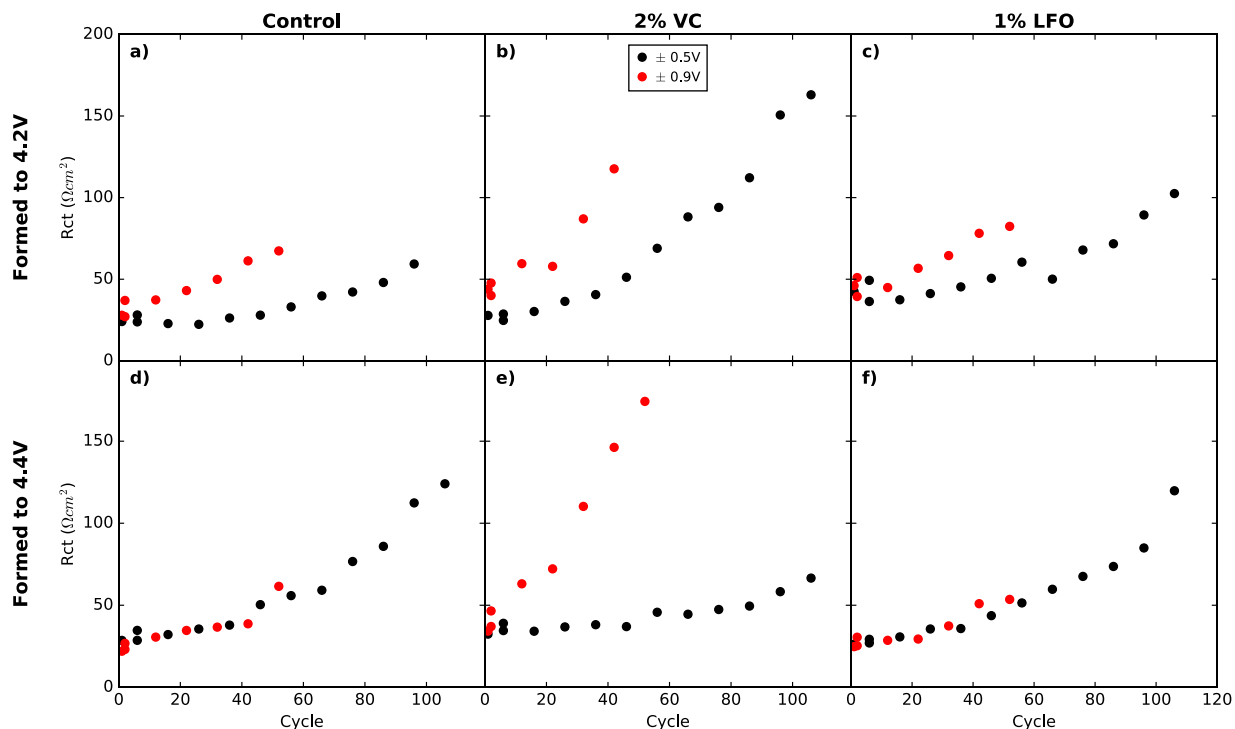
Figure 5.3: R$_{ct}$ (measured at 10°C) vs. cycle number for all cycled NMC532 symmetric cells. Cells cycled between ± 0.5 V are in black; cells cycled between ± 0.9 V are in red. Cells in (a-c) were made from NMC532 electrodes from pouch cells formed to 4.2 V, while (d-f) were from pouch cells formed to 4.4 V. (a) and (d) show cells with control electrolyte; (b) and (e) show cells with control + 2% VC electrolyte; (c) and (f) show cells with control + 1% LFO electrolyte.

Figure 5.4 shows results of dV/dQ analysis for the first charge (a and b) and last charge (c and d) of the positive symmetric cell containing control electrolyte cycled between ±0.9 V from a pouch cell formed to 4.2 V. Results were similar for all symmetric cells in this study. The relative slippage of the half cell curves was 0.74 mAh after the first charge, and 1.99 mAh after the last charge. This results in a Δ relative slippage of 1.25 mAh. Based on the fits, both electrodes had only ~10% mass loss. Change in slippage from Li$^+$ inventory loss was determined to be the larger contributor to capacity fade in these positive symmetric cells.

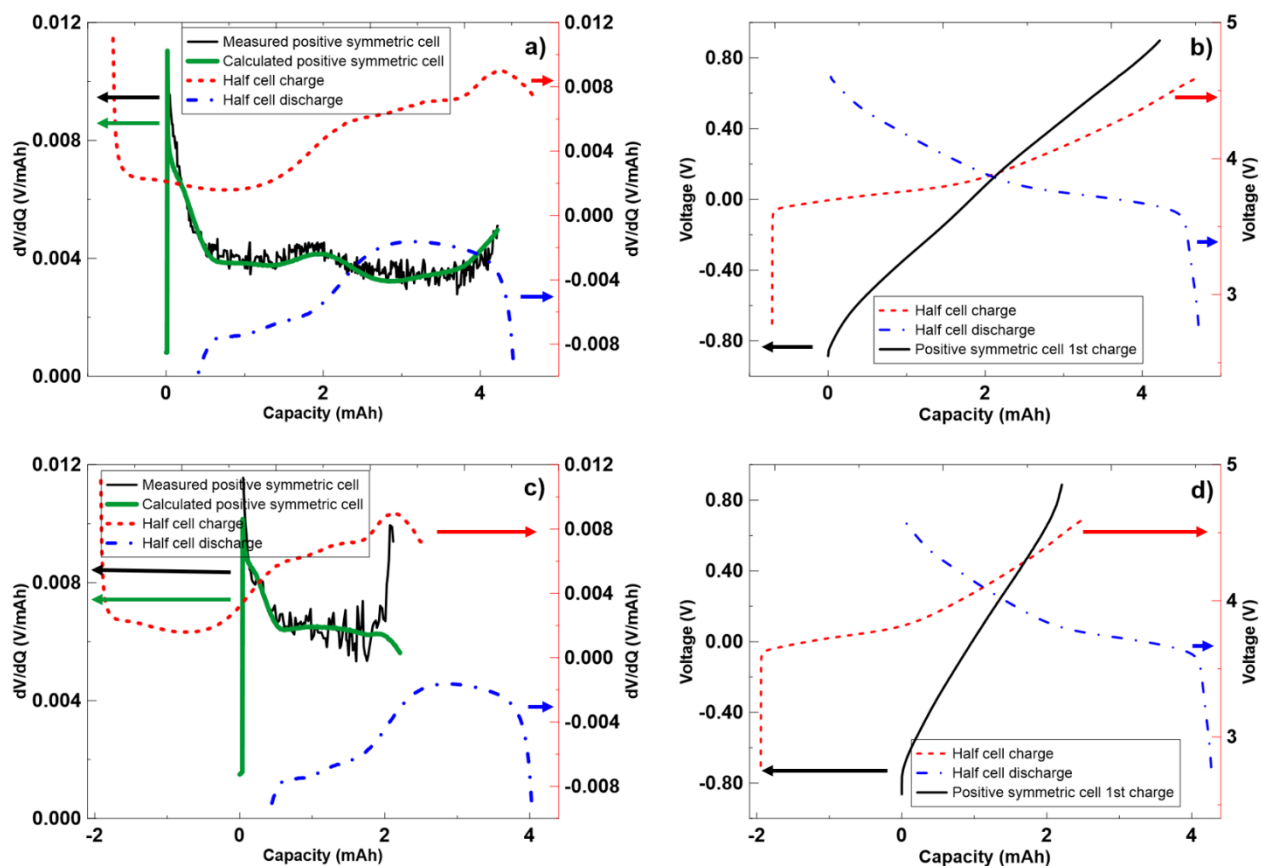Figure 5.4: Differential voltage analysis for a positive symmetric cell containing control electrolyte before and after cycling between ±0.9 V. (a) and (b) show data for the first charge of the positive symmetric cell; (c) and (d) show data for the 60th charge of the positive symmetric cell. (a) and (c) show dV/dQ vs. capacity fits of positive symmetric cell charge curves. Half cell charge and discharge dV/dQ vs. capacity curves used to calculate the fit are also shown. (b) and (d) show voltage vs. capacity of the positive symmetric cell charge curves as well as the half cell charge and discharge curves. The y-axis for each curve is indicated by an arrow which is the same color as the curve.

5.4   Conclusions

Positive symmetric cells with NMC532 electrodes were cycled with decent capacity retention. In general, electrolyte additives did not appear to have a large impact on capacity retention over the lifetime of the cells. Large differences were also not apparent in ΔV data, though cells cycled to high voltage containing LFO did have lower ΔV than cells with control and control + 2% VC

electrolytes. R_{ct} data showed the largest impedance growth in high voltage cells containing 2% VC, in agreement with the literature. No obvious variations were observed between cells made from pouch cells that were formed to 4.2 V versus pouch cells that were formed to 4.4 V. Through dV/dQ analysis, it was determined that capacity loss was mainly due to Li^+ inventory depletion as a result of reactions at the NMC532 electrodes.

It would be interesting to perform positive symmetric cell cycling studies with a variety of electrolyte systems. Using a frequency response analyzer (FRA) system to perform EIS measurements without removing cells from cycling would help control and automate this experiment. It is also recommended that researchers make many duplicate cells for cycling as symmetric cell variability is difficult to avoid.

Chapter 6: Conclusions and Future Work

6.1   Conclusions

The SEI that develops on Li-ion cell electrodes is critical to the function of the cell. A well formed SEI hinders unwanted reactions between the electrolyte and electrode active material, while simultaneously allowing for easy Li^+ transport. However, flawless SEIs are difficult to achieve and changes occur over cycling, contributing to impedance growth and capacity fade in the cell. Despite its vital role, the SEI is not well understood even after many years of research. This thesis attempted to study the properties of the SEI under various conditions.

Impedance measurements and XPS analysis were used to study the SEI on the negative and positive electrodes from formed and cycled NMC532/AG pouch cells. Negative and positive symmetric cells were made for all studies in this thesis in order to study SEI layers on each electrode separately. Since impedance measurements were a large part of this work, Chapter 3 was devoted to the interpretation of EIS spectra. The high frequency semicircle in Nyquist plots was shown to be due to contact impedance at the electrode particle/current collector interface. It was also shown that R_{ct} has a strong temperature dependence and that measuring EIS at low temperatures (ideally less than or equal to 10ºC) allows for clear separation of charge transfer impedance from contact impedance. Using double-sided electrodes in symmetric cells was shown to provide accurate measurements of charge transfer resistance.

Chapter 4 presented the results of the main study in this thesis in which the properties of the positive electrode SEI and negative electrode SEI were probed using XPS and temperature

dependent EIS. Cells were tested after formation and after cycling to different upper cutoff potentials. The effects of different electrolyte additives on the SEI were also studied. Temperature dependent EIS studies showed that R_{ct} follows an Arrhenius relationship. This allowed for the calculation of activation energies (E_a) associated with Li^+ transport through the SEI. After formation, E_a was shown to vary for negative electrode SEIs with different electrolytes, suggesting that electrolyte additives impact SEI composition and transport properties at the graphite electrode. In contrast, E_a for positive electrodes after formation was consistent for all electrolytes. E_a for positive and negative electrodes was either decreased after cycling or remained constant at the value measured after formation. The difference in E_a after cycling varied depending on electrolyte additive, voltage limits, and electrode type. Cells containing LFO electrolyte additive showed consistently lower E_a values for the negative electrode than cells with VC electrolyte additive or cells containing control electrolyte over all cycling conditions. This suggests that LFO may form the SEI with the best transport properties of the three electrolytes tested.

Charge transfer resistance also varied with cycling. For negative electrodes, R_{ct} either decreased or remained constant. For positive electrodes, R_{ct} decreased or increased with cycling depending on electrolyte additive and upper cutoff voltage. Charge transfer resistance trends with cycling were not always correlated to E_a trends, suggesting that Li^+ transport is only one of several factors impacting SEI impedance.

Capacitance was calculated from EIS data based on Equation 2.20. The results showed that the positive electrode had much higher capacitance, suggesting a thinner SEI layer on the positive active material. Additionally, in combination with R_{ct} and E_a results, capacitance data can suggest SEI thickness and porosity changes after cycling.

XPS was used to investigate SEI composition and thickness. With different electrolyte additives, the main differences in SEI compositions were in the quantities of inorganic materials. Higher inorganic material quantities appeared to correlate with lower activation energies measured by temperature dependent EIS. The development of SEI composition remains unclear and requires further research. Further study of the relationships between charge transfer resistance, activation energy, SEI chemistry, and SEI thickness may help in understanding the properties and development of the SEI. This in turn could help researchers control impedance growth and capacity loss in Li-ion cells.

$R_{contact}$ was also examined in this study and $R_{contact}$ for negative electrodes was shown to be unaffected by cycling. However, $R_{contact}$ for positive electrodes showed some changes over cycling which may have been caused by loss of electrical contact between active particles and the current collector.

Finally, in Chapter 5, NMC532 symmetric cells were cycled to study electrode/electrolyte interactions at the positive electrode alone. It was found that Li^+ inventory was lost at the NMC532 electrode, contributing to capacity loss.

6.2   Future Work

In this thesis, temperature dependent EIS showed that charge transfer impedance has a strong temperature dependence. This was shown for positive and negative electrode SEIs formed in cells containing various electrolytes and cycled for different lengths of time and to different upper voltage limits. Values for several components of impedance were extracted from Nyquist plot fits

and compared between cell types. Activation energy values were calculated based on temperature dependent EIS data. Further work related to this study could be done in a variety of areas. Some suggestions are offered below.

Tests could be performed more frequently during cycling and over a longer period of time. However, every temperature dependent EIS test requires building many symmetric cells in order to separate impedance contributions from the positive and negative electrodes (a time-intensive process). This necessitates disassembly of a pouch cell for every additional test during cycling. Therefore, every additional test requires an additional pouch cell to be cycled. This may be logistically limited by time and by the availability of cycling channels. Performing tests over a longer cycle life would also allow for cells with good capacity retention to be studied after more significant capacity fade, which may help in understanding failure mechanisms in these cells. For example, many cells containing 2% VC additive or 1% LFO additive studied in this thesis had only lost < 3 % capacity before the last measurements were made. With more cycling and more frequent measurements, trends in impedance parameters and activation energy could be monitored over cycle life. In this thesis, E_a after cycling either remained unchanged or decreased compared to E_a after formation. R_{ct} increased or decreased with cycling depending on the electrode tested, the electrolyte in the cell, and the upper cutoff voltage during cycling. Trends may become more apparent in E_a and R_{ct} over cycle life with more frequent tests.

XPS samples could also be made from disassembled pouch cell electrodes at these extra stages of cycle life. Additional XPS data may help elucidate the evolution of the SEI composition during cycling and could be compared to impedance measurements, and E_a values. Additional tools could be used to study SEI thickness, composition, and morphology. Argon-ion sputtering can be used

to measure the depth profile of the SEI;[94,95] SEI composition has also been studied using NMR and TEM;[38] and SEM can be used to observed SEI morphology.[96–98] Schwenke et al.[99] and Nie et al.[34,38] have evaluated SEI compositions based on NMR results. NMR samples were prepared by dissolving the SEI components in D_2O. This may be the most effective way to study the SEI, and should be adopted by Dahn lab personnel.

Cells containing different electrolyte systems could also undergo similar temperature dependent EIS tests and XPS tests and could be compared to the data presented in this thesis. Electrolytes containing electrolyte additives that are known to be excellent in full Li-ion cells may be of particular interest. Good electrolyte additive combinations include: 2% VC + 1% DTD (dimethyl carbonate), and 2% FEC (fluoroethylene carbonate) + 1% LFO.[24]

More research should be done regarding the interpretation of the capacitance calculated from EIS data. The dielectric constant is not well known or understood for SEI films, and the density of the SEI may change upon cycling. Porosity of the SEI would be valuable to investigate as increasing porosity could have differing effects on R_{ct}, E_a, and capacitance. For example, with a more porous SEI, transport of Li^+ through the SEI could improve, leading to decreased R_{ct} and E_a. Decreasing R_{ct} would increase the capacitance calculated based on Equation 2.20. In the situation where SEI porosity changes, Equation 2.21 may no longer report accurate thickness estimates since the calculated value of C that would be used in this Equation depends on the porosity.

The interpretation of EIS spectra could be studied further to clarify physical sources of impedance in the cell. Further studies using symmetric cells with electrolytes that have very low ionic conductivities may provide more clarity as to how ionic resistance in electrode pores (R_{ion}) and

contact impedance change as a function of electrolyte conductivity. These studies could be performed at multiple temperatures to highlight any temperature dependence observed for ionic resistance in electrode pores. It was shown in this thesis that the high frequency semicircle present in positive and negative symmetric cell Nyquist plots is due to contact resistance, and that the contact resistance does not have a strong temperature dependence. Therefore, if strong temperature dependence is observed in low conductivity cells, this may suggest a temperature dependence of R_{ion}.

As shown in Chapter 5 of this thesis, and previously presented by Burns et al., cycling symmetric cells can be a useful tool for studying the interactions of electrolytes with one electrode alone.[46] In this thesis, NMC532 positive symmetric cells were cycled and cells were removed from cycling periodically for EIS measurements. Cells were programmed to stop automatically at 0.00 V for EIS measurements every 10 cycles. This methodology introduced some unavoidable down time where cells were sitting at 0.00 V waiting for EIS measurements. As shown by Xiong et al., rapid impedance growth and gas generation occurs in storage cells containing only NMC positive electrodes.[100] Therefore, inconsistent downtime may impact impedance measurements in positive symmetric cells. Ideally, positive symmetric cells would be cycled on a frequency response analyzer (FRA) system. FRA systems can be programmed to perform cycling and do EIS measurements periodically. Cells can be stopped automatically at specified voltages to perform EIS measurements, and cycling is restarted immediately following completion of the EIS test. It is also recommended that high precision chargers be used to cycle positive symmetric cells if dV/dQ analysis will be performed. This would reduce noise in the data which makes dV/dQ fitting less accurate.

Positive symmetric cell cycling results in this thesis did not show major differences in capacity retention or ΔV between cells with control, control + 2% VC, or control + 1% LFO electrolytes. R_{ct} growth was most significant in high voltage 2% VC cells. It would be valuable to perform positive symmetric cell cycling studies with EIS measurements on a wide variety of cells. As mentioned above, electrolyte additives that perform well in Li-ion cells include 2% VC + 1% DTD, and 2% FEC + 1% LFO.[24] These additives may also be of interest in positive symmetric cell studies. These electrolytes could also be tested in (+/+) cells with different electrode materials to study the electrode/electrolyte interactions without the contribution from the negative electrode.

In relation to the FRA systems in the Dahn lab – software bugs currently exist in the system which make its use cumbersome. Communication is not robust between the FRA software and the Neware charger that cycles the cells. This leads to EIS being measured on the wrong cycle. The Gamry, which performs EIS measurements in the FRA system, also often gets stuck trying to measure EIS. Additionally, the FRA protocol software has limitations on when EIS measurements can be done. The FRA protocol software could be programmed to include more user scenarios.

Automated temperature control was achieved on the Dahn lab EIS system for temperature dependent EIS tests in this thesis. The system includes three BioLogic potentiostats connected to three Novonix temperature boxes each containing 16 cell channels (total of 48 channels). Each temperature box (all 16 cell channels) is connected to a switching unit to allow a potentiostat to measure EIS for many consecutive cells in a temperature box. Switching is controlled by Keithley multimeters, and multimeters are controlled by Dahn lab Visual Basic switching software on the EIS computer. EC-lab is the software that controls the BioLogic potentiostats, and it also sends

output triggers to the Keithley switching software when the EIS test on a cell is complete and the switching unit can switch the measuring channel.

Previously, 16 channels could do EIS measurements sequentially in one temperature-controlled box using one BioLogic potentiostat. If tests were required to run at multiple temperatures, the temperature of the box would need to be changed manually using a Watlow temperature controller installed as part of the Novonix temperature box. To automate temperature changes, the temperature controller in one Novonix box was replaced with a different, programmable, Watlow temperature controller. The new temperature controller is programmable on the device itself, not triggered externally. It can be set to change the temperature of the box and hold at the new temperature for a specified amount of time.

The in-house Keithley switching software was also modified in order to loop over the cells in the box to test each cell channel at each temperature. EC-lab settings were set to align with the test and send appropriate triggers to the Keithley switching software. Unfortunately, since the new temperature controller can not be triggered externally, the temperature switching and channel switching must be programmed to line up and must be started at the same time. This introduces several flaws to the automation of the temperature dependent EIS tests. The time to hold at a given temperature must be set on the temperature controller. If the timing is off for any reason, this introduces the possibility of EIS measurements being done at the wrong temperature. For example, if one cell channel takes more than the estimated time to complete EIS measurements, this can make the EIS measurements "late" and may run in to a temperature change.

Ideally, a different temperature controller that could be controlled by triggers sent by EC-lab would replace the non-triggerable controller that is currently part of the system. This would make running temperature dependent EIS on the system significantly more robust.

Another problem related to the system is that there is currently no way to automatically record the internal temperature of the box. This could be achieved using a thermocouple and software to record the temperature periodically. This also may be easily achievable with a different temperature controller that is directly connected to the computer.

Appendix A: Permissions

With minor editing privileges	yes
For distribution to	Worldwide
In the following language(s)	Original language of publication
With incidental promotional use	no
Lifetime unit quantity of new product	Up to 499
Title	PROBING CHANGES IN THE SOLID ELECTROLYTE INTERPHASE IN LI-ION CELLS
Institution name	Dalhousie University
Expected presentation date	Oct 2019

Note: This item was invoiced separately through our **RightsLink service,** More info $ 0,00

Total order items: 1   **Order Total: $0.00**

# Appendix B: Additional Data

B.1   Bode Plots for Blocking/Non-blocking cells
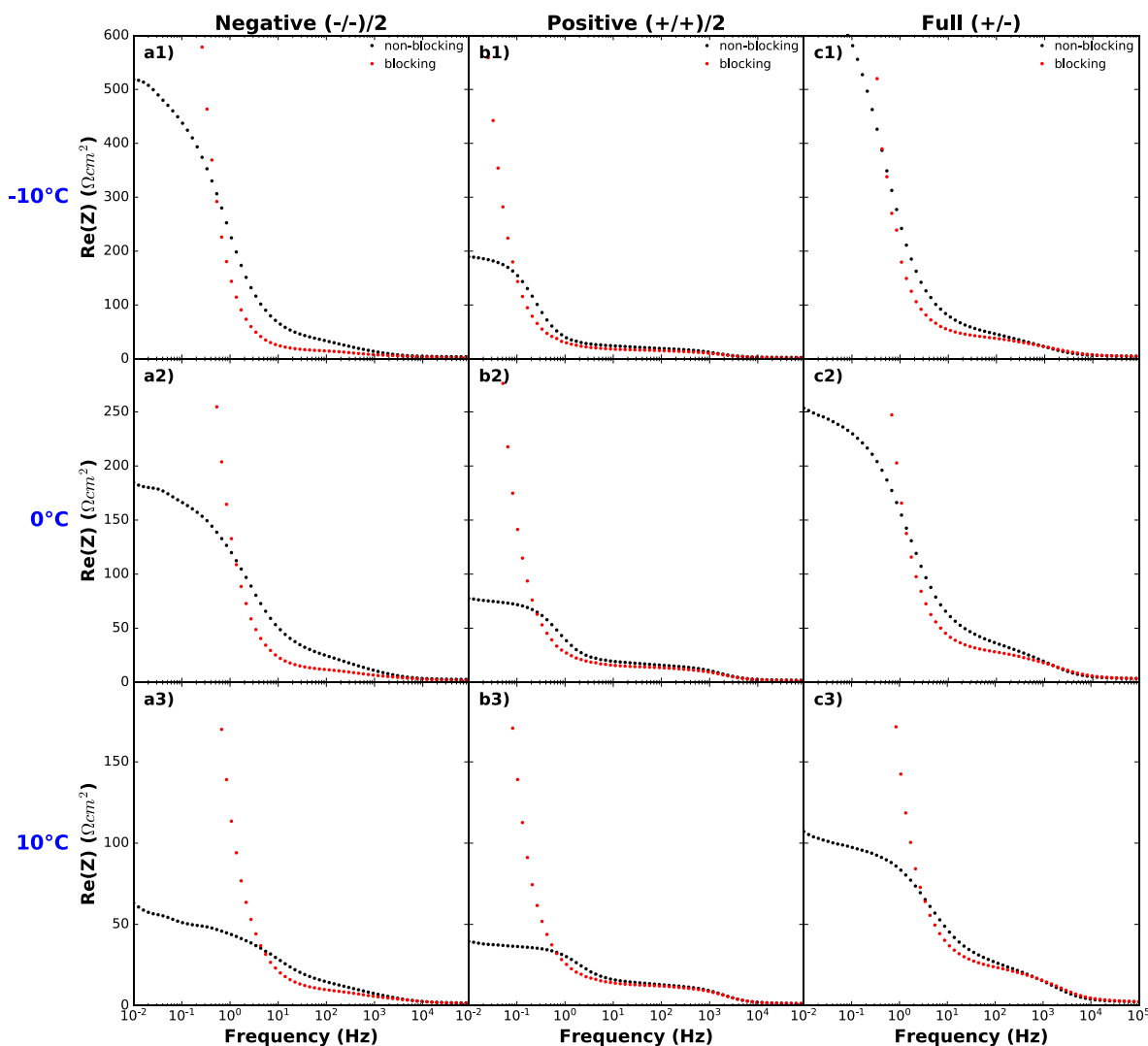
Figure B.1: Area specific real impedance versus the logarithm of frequency plots of blocking and non-blocking (a1-a3) negative electrode symmetric cells, (b1-b3) positive electrode symmetric cells, and (c1-c3) full coin cells. (a1), (b1), and (c1) measured at -10°C; (a2), (b2), and (c2) measured at 0°C; and (a3), (b3), and (c3) measured at 10°C.
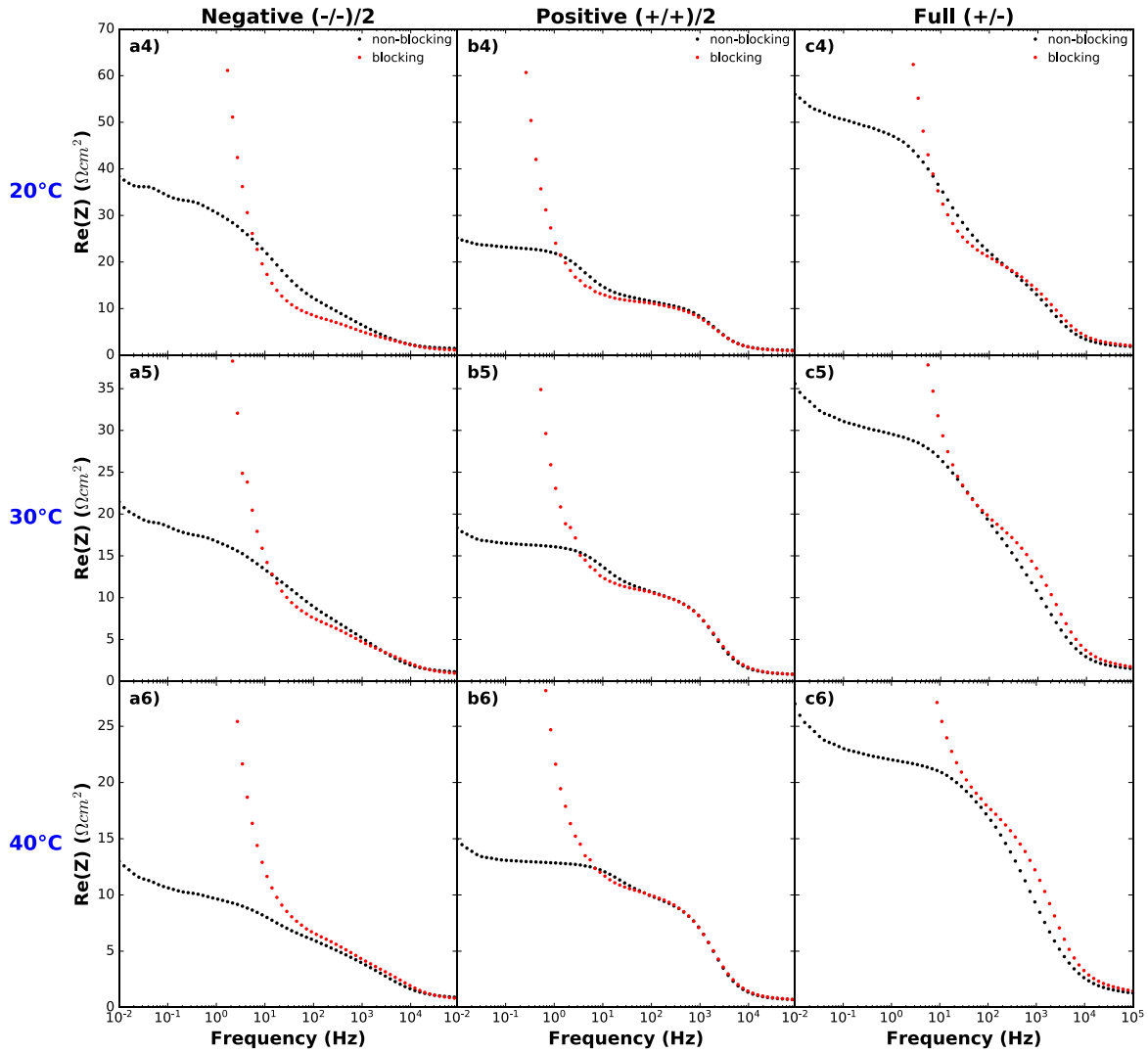
Figure B.2: Area specific real impedance versus the logarithm of frequency plots of blocking and non-blocking (a4-a6) negative electrode symmetric cells, (b4-b6) positive electrode symmetric cells, and (c4-c6) full coin cells. (a4), (b4), and (c4) measured at 20°C; (a5), (b5), and (c5) measured at 30°C; and (a6), (b6), and (c6) measured at 40°C.
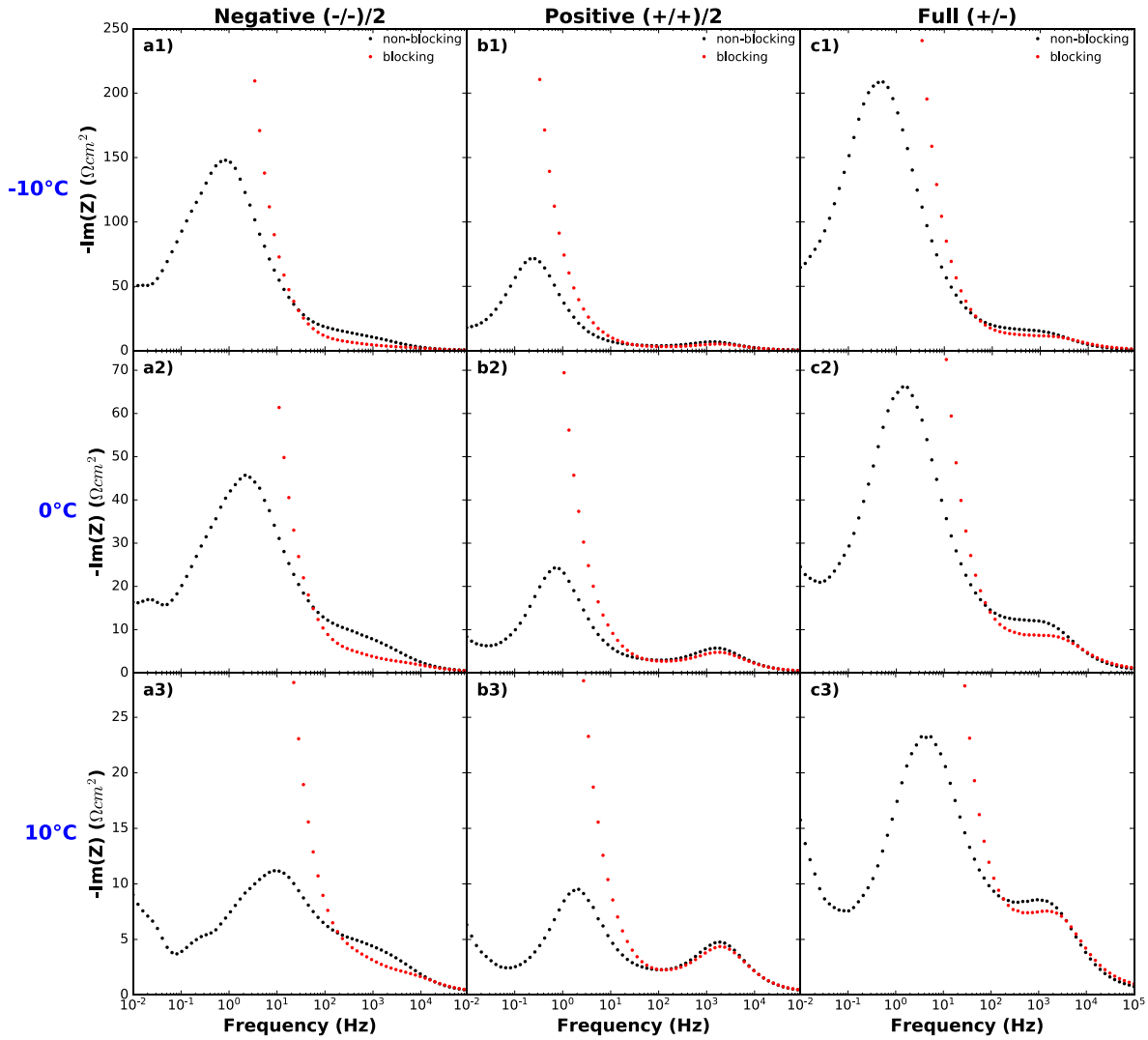
Figure B.3: Area specific negative imaginary impedance versus the logarithm of frequency plots of blocking and non-blocking (a1-a3) negative electrode symmetric cells, (b1-b3) positive electrode symmetric cells, and (c1-c3) full coin cells. (a1), (b1), and (c1) measured at -10°C; (a2), (b2), and (c2) measured at 0°C; and (a3), (b3), and (c3) measured at 10°C.
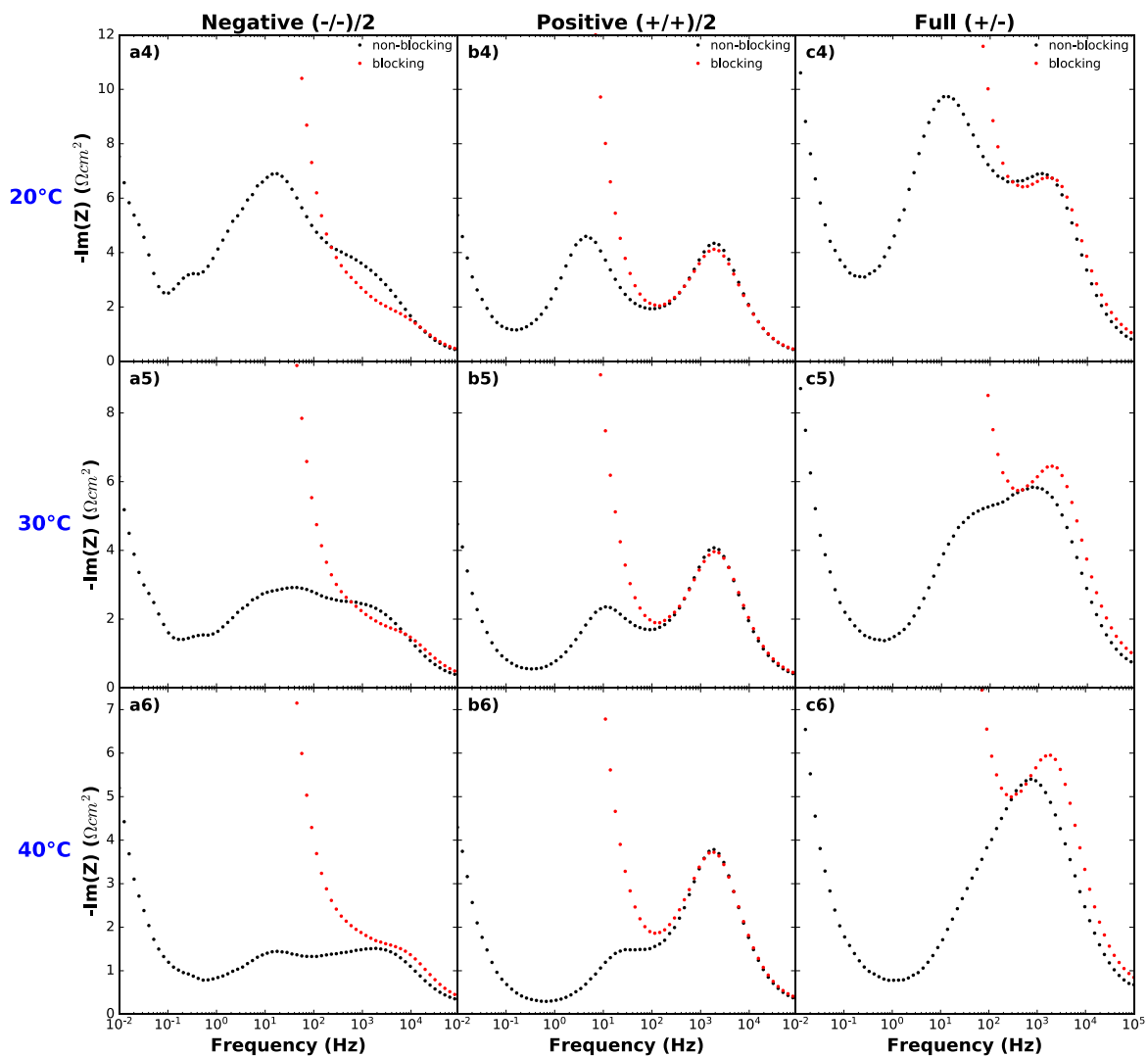
Figure B.4: Area specific negative imaginary impedance versus the logarithm of frequency plots of blocking and non-blocking (a4-a6) negative electrode symmetric cells, (b4-b6) positive electrode symmetric cells, and (c4-c6) full coin cells. (a4), (b4), and (c4) measured at 20°C; (a5), (b5), and (c5) measured at 30°C; and (a6), (b6), and (c6) measured at 40°C.

B.2   Characteristic Frequency
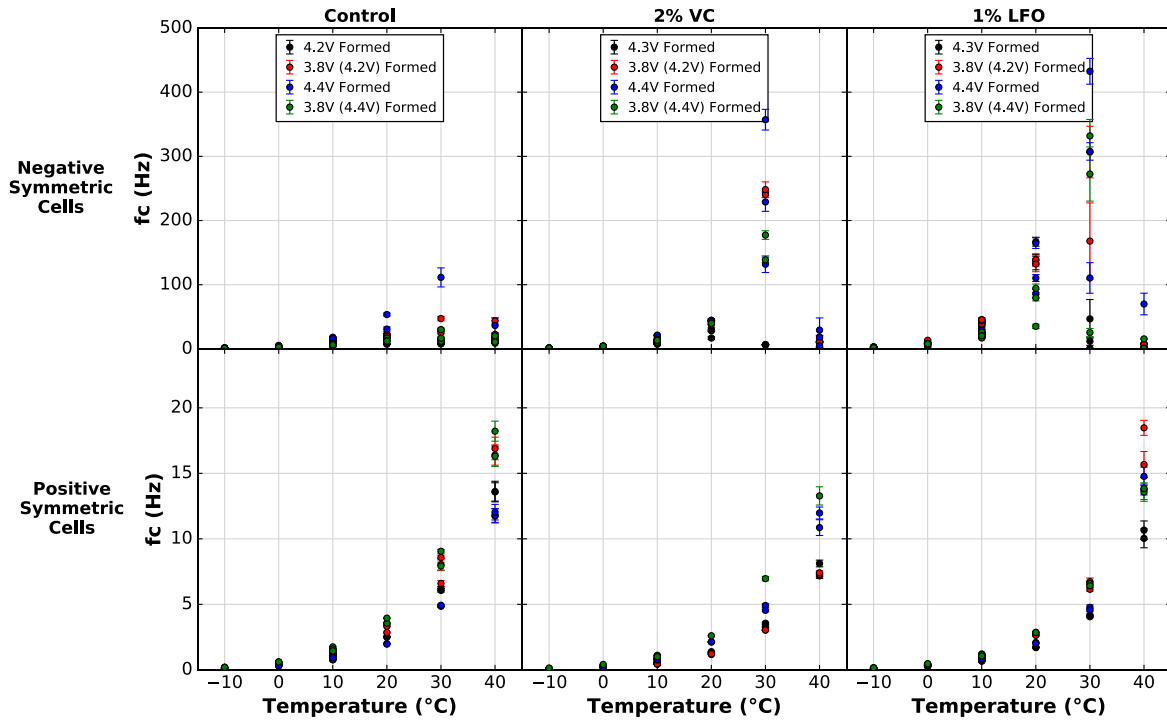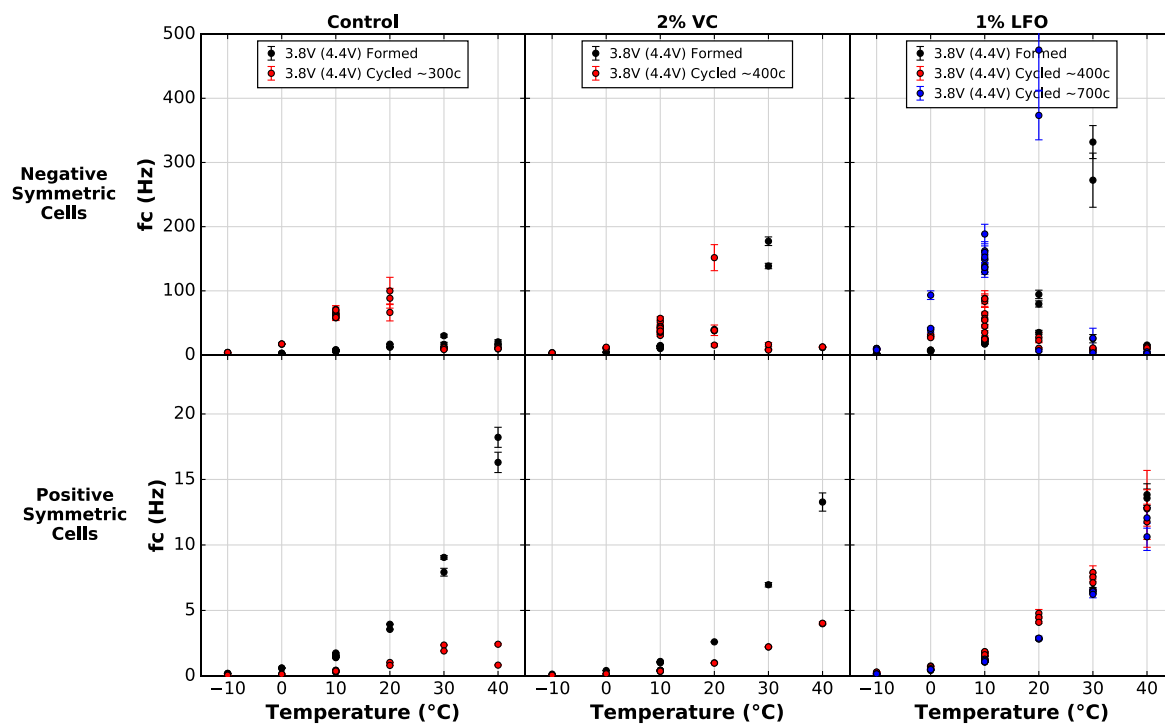

Figure B.5: Characteristic frequency of the charge transfer resistance semicircle in Nyquist plots of symmetric cells from formed pouch cells at different SOC. Negative symmetric cell data is in the top row; positive symmetric cell data is in the bottom row. Cells with control electrolyte are in the left column; control + 2% VC in the middle column; and control + 1% LFO in the right column. Legends indicate the voltage at disassembly and indicate the TOC voltage in brackets if different than TOC. The error bars shown are the statistical error from the fitting results, however the true error in the measurement is larger than this.
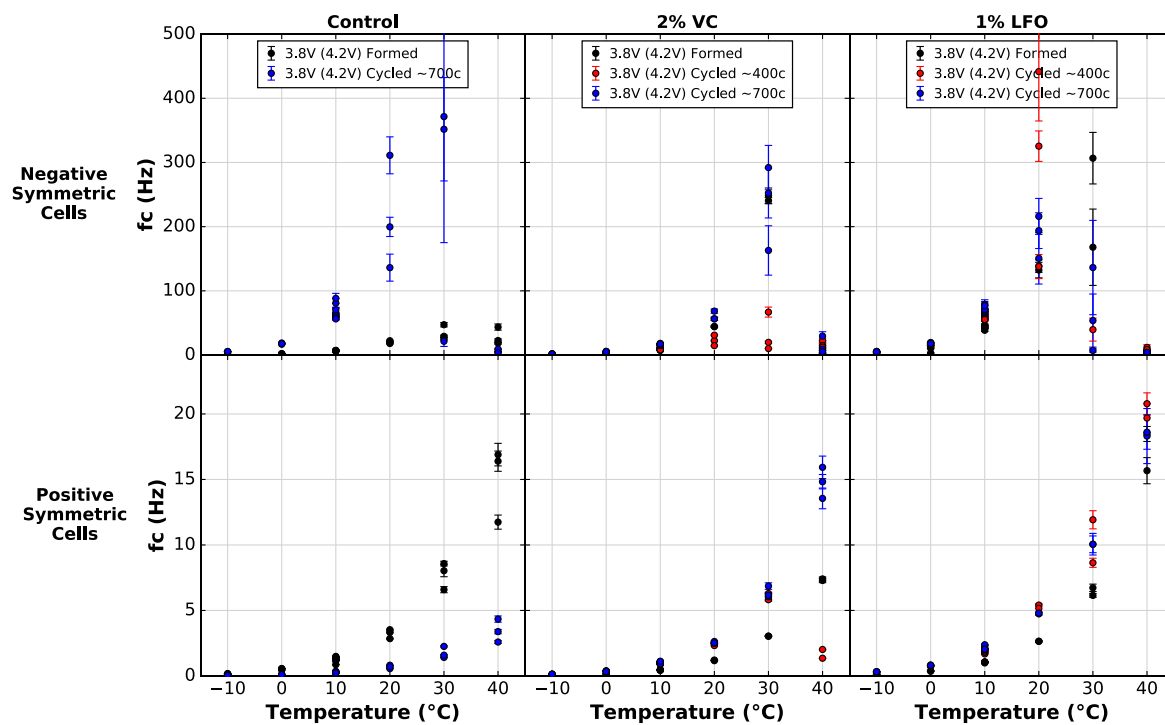
Figure B.6: Characteristic frequency of the charge transfer resistance semicircle in Nyquist plots of symmetric cells from formed and cycled pouch cells with 4.2 V TOC. Negative symmetric cell data is in the top row; positive symmetric cell data is in the bottom row. Cells with control electrolyte are in the left column; control + 2% VC in the middle column; and control + 1% LFO in the right column. Legends indicate the voltage at disassembly (always 3.8 V here), the TOC voltage in brackets (always 4.2 V here), and the approximate number of cycles done by the cell before disassembly. The error bars shown are the statistical error from the fitting results, however the true error in the measurement is larger than this.

Figure B.7: Characteristic frequency of the charge transfer resistance semicircle in Nyquist plots of symmetric cells from formed and cycled pouch cells with 4.4 V TOC. Negative symmetric cell data is in the top row; positive symmetric cell data is in the bottom row. Cells with control electrolyte are in the left column; control + 2% VC in the middle column; and control + 1% LFO in the right column. Legends indicate the voltage at disassembly (always 3.8V here), the TOC voltage in brackets (always 4.4 V here), and the approximate number of cycles done by the cell before disassembly. The error bars shown are the statistical error from the fitting results, however the true error in the measurement is larger than this.

129

B.3   Comparison of Cells with 2% VC Additive
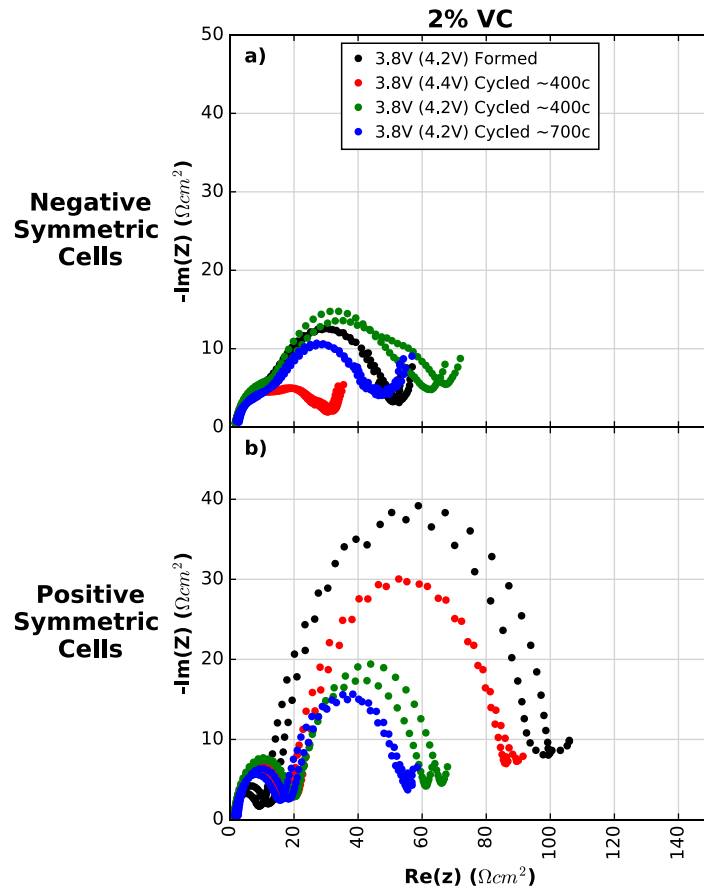
Figure B.8: Nyquist plots of symmetric cells from formed and cycled pouch cells with control + 2% VC electrolyte measured at 10ºC. (a) Negative symmetric cell data; (b) positive symmetric cell data. Legends indicate the voltage at disassembly (always 3.8V here), the TOC voltage in brackets, and the approximate number of cycles done by the pouch cell before disassembly. Data from duplicate cells is shown for every cell type.
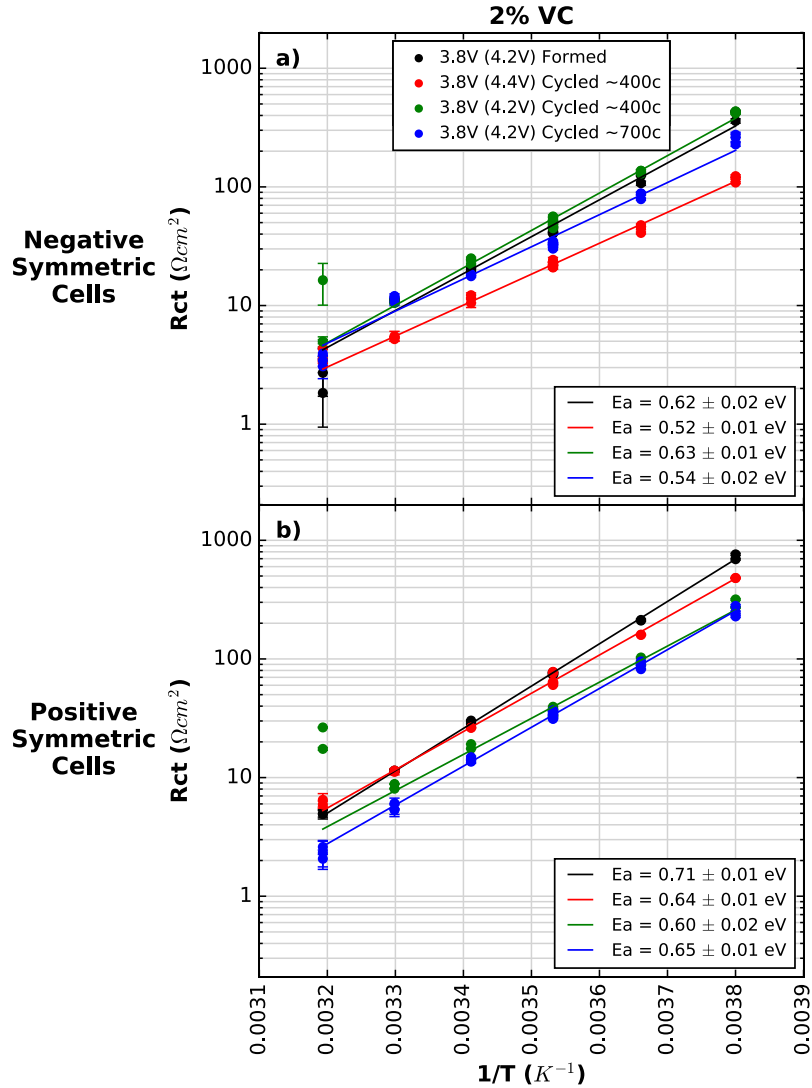
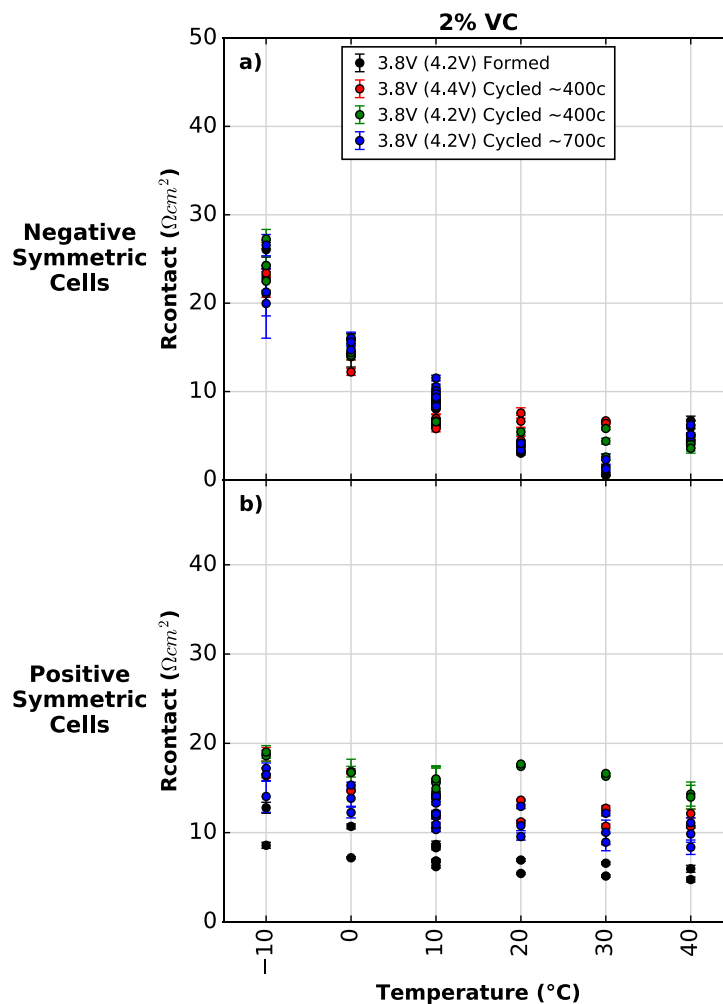Figure B.9: R$_{ct}$ plotted on a logarithmic scale vs. the inverse of temperature for symmetric cells from formed and cycled pouch cells with control + 2% VC electrolyte. (a) Negative symmetric cell data; (b) positive symmetric cell data. Legends indicate the voltage at disassembly (always 3.8V here), the TOC voltage in brackets, and the approximate number of cycles done by the pouch cell before disassembly. Linear fits of the data associated with each cell are shown and activation energies calculated from the linear fits are indicated in the bottom right legends. Data is shown for duplicate and triplicate cells at each temperature, with additional points at 10°C (0.0035 K-1) due to repeat tests at that temperature. The error bars shown are the statistical error from the fitting results, however the true error in the measurement is larger than this. Points at 40ºC (0.0032 K^{-1}) were not used in the linear fit due to unreliability in EIS fitting at high temperature.

131

Figure B.10: R$_{contact}$ vs. temperature for symmetric cells from formed and cycled pouch cells with control + 2% VC electrolyte. (a) Negative symmetric cell data; (b) positive symmetric cell data. Legends indicate the voltage at disassembly (always 3.8V here), the TOC voltage in brackets, and the approximate number of cycles done by the pouch cell before disassembly. Data from duplicate and triplicate cells is included for every cell type. The error bars shown are the statistical error from the fitting results, however the true error in the measurement is larger than this.
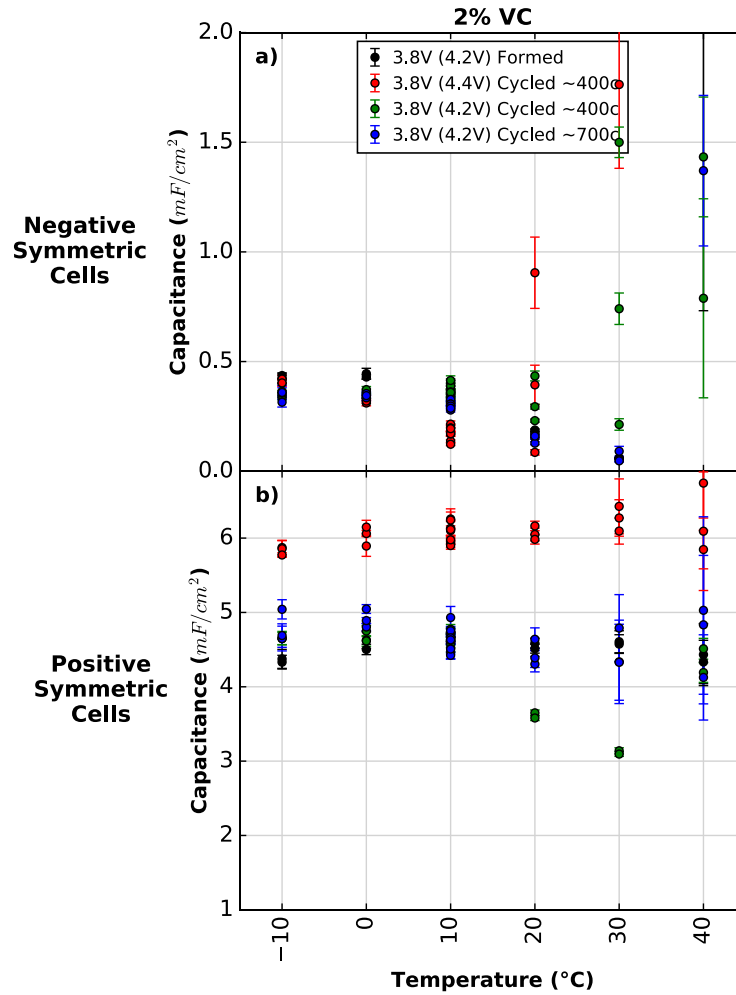
Figure B.11: Calculated capacitance (associated with R_{ct}) vs. temperature for symmetric cells from formed and cycled pouch cells with control + 2% VC electrolyte. (a) Negative symmetric cell data; (b) positive symmetric cell data. Legends indicate the voltage at disassembly (always 3.8V here), the TOC voltage in brackets, and the approximate number of cycles done by the pouch cell before disassembly. Data from duplicate and triplicate cells is included for every cell type. The error bars shown are the statistical error from the fitting results, however the true error in the measurement is larger than this.
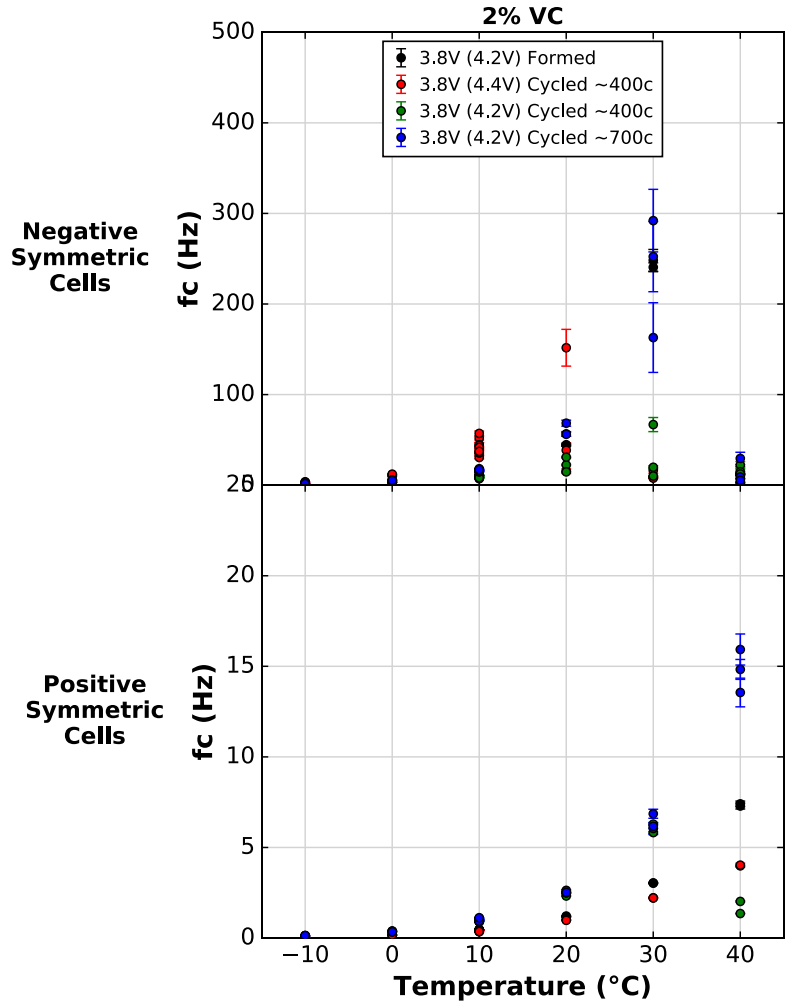
Figure B.12: Characteristic frequency (associated with R_{ct}) vs. temperature for symmetric cells from formed and cycled pouch cells with control + 2% VC electrolyte. (Top) negative symmetric cell data; (bottom) positive symmetric cell data. Legends indicate the voltage at disassembly (always 3.8V here), the TOC voltage in brackets, and the approximate number of cycles done by the pouch cell before disassembly. Data from duplicate and triplicate cells is included for every cell type. The error bars shown are the statistical error from the fitting results, however the true error in the measurement is larger than this.

B.4   Raw EIS Data

This section contains plots of EIS data for each disassembled cell in this thesis. Plots are each twelve panels and include (+/+), (-/-), and (+/-) cells measured at -10ºC, 10ºC, 30ºC and 40ºC. Additional data at 10ºC and data for 0ºC, 20ºC is not shown. Data for duplicate and triplicate cells is shown. All parent pouch cells contained NMC532/AG electrodes. Captions for these figures state the electrolyte, the number of cycles (if cycled); the TOC voltage, and the voltage at which cells were disassembled.
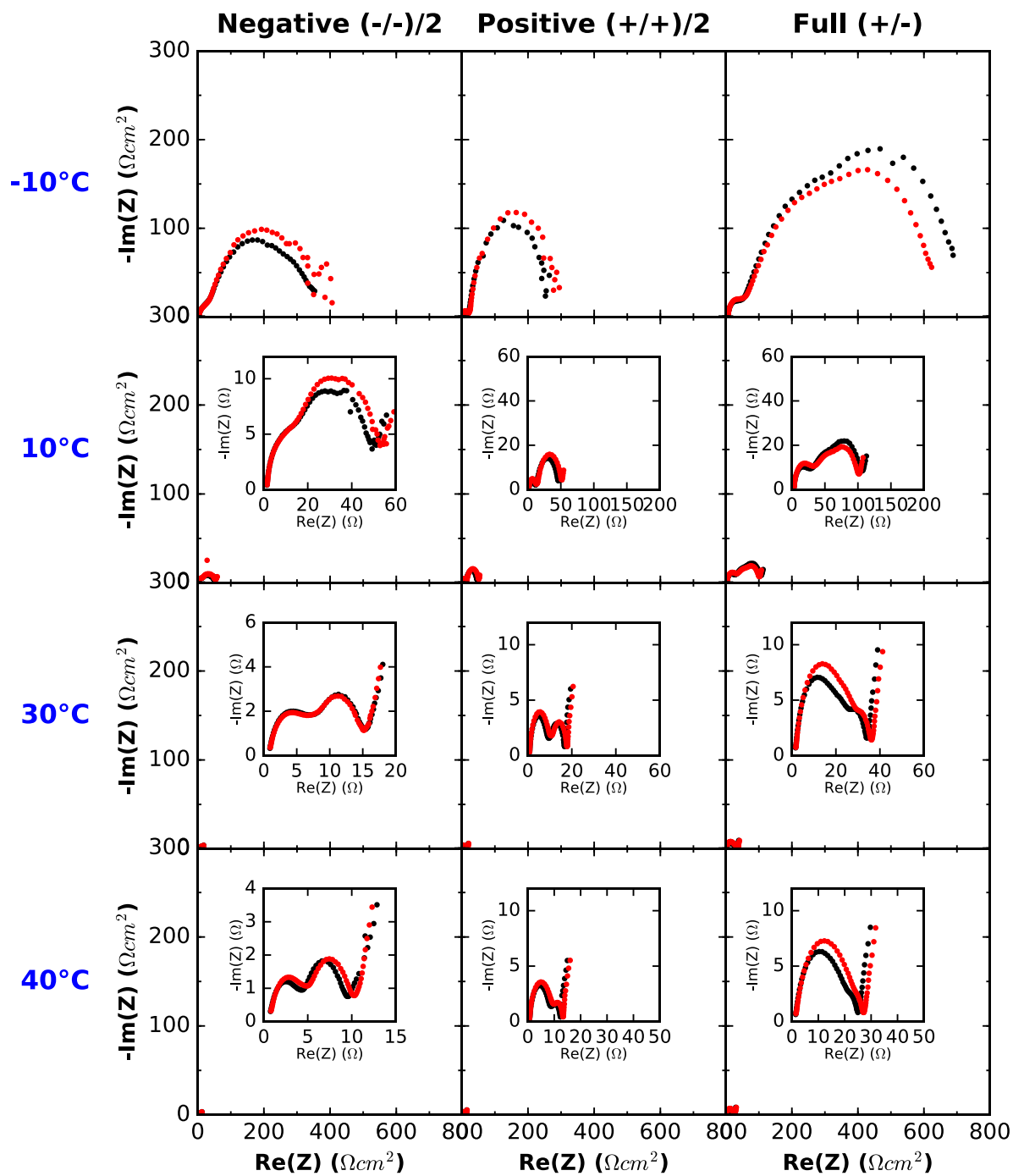
Figure B.13: Control electrolyte; disassembled after formation; formed to 4.2 V and measured at 4.2 V.
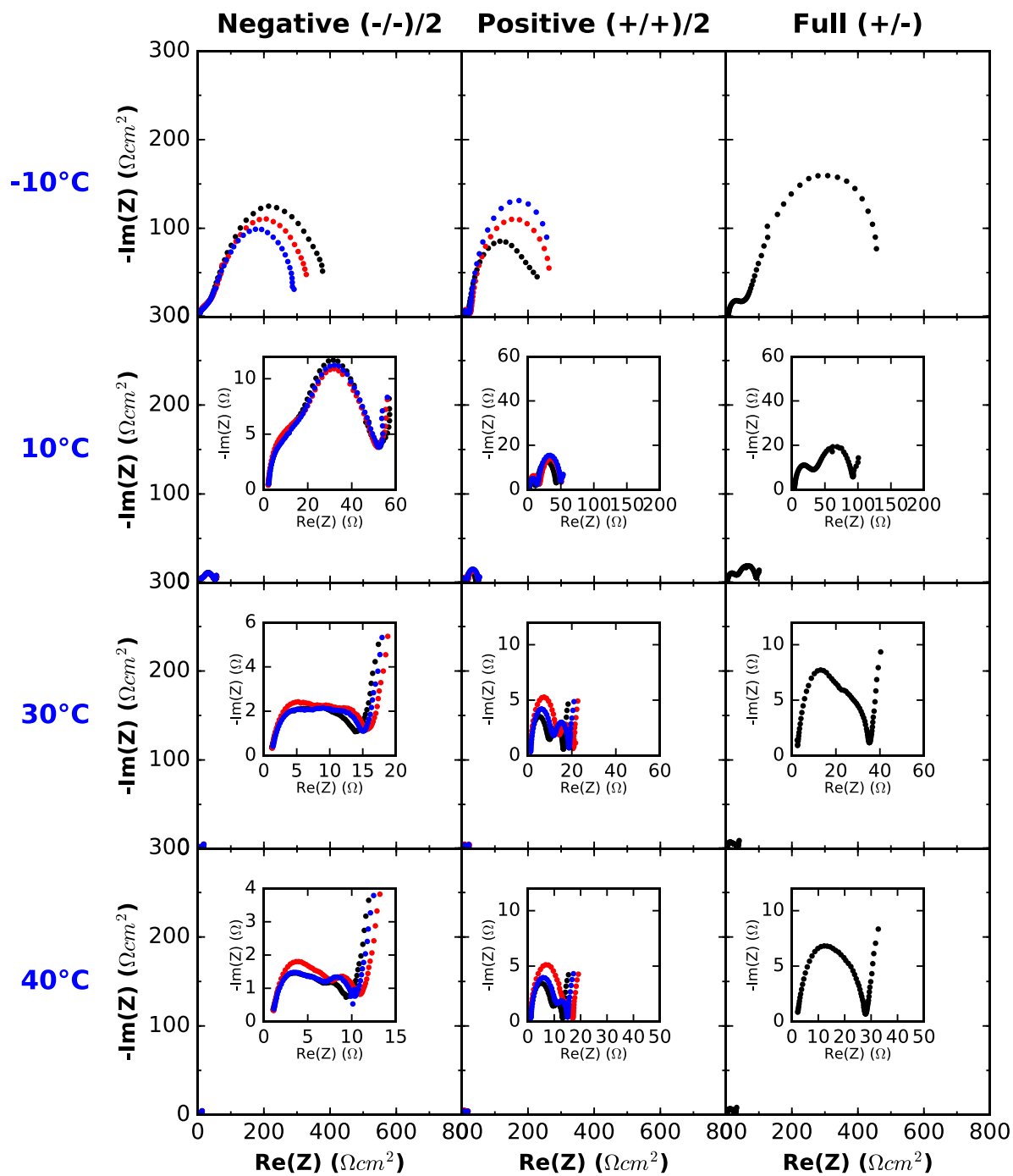
Figure B.14: Control electrolyte; disassembled after formation; formed to 4.2 V and measured at 3.8 V.
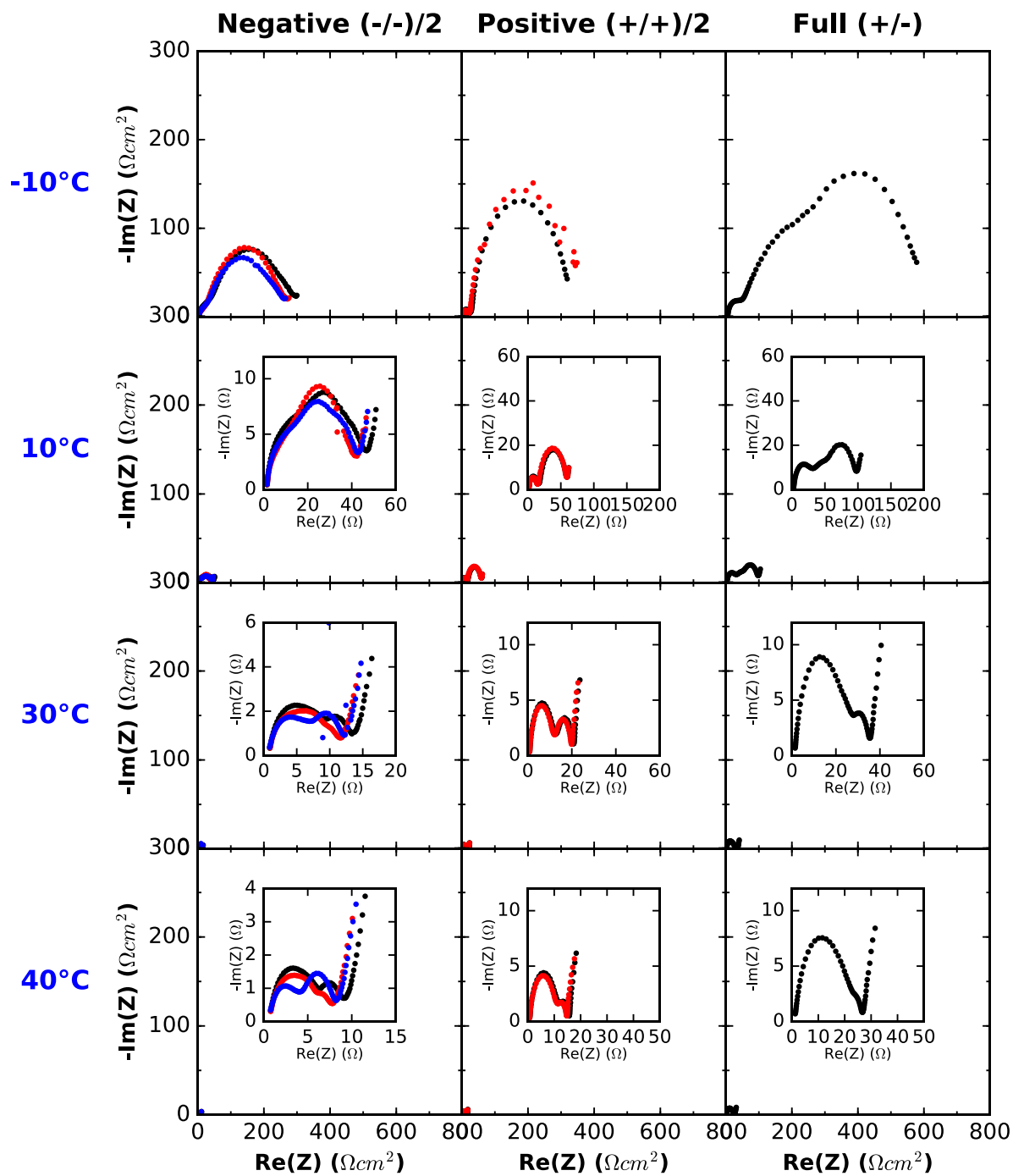
Figure B.15: Control electrolyte; disassembled after formation; formed to 4.4 V and measured at 4.4 V.
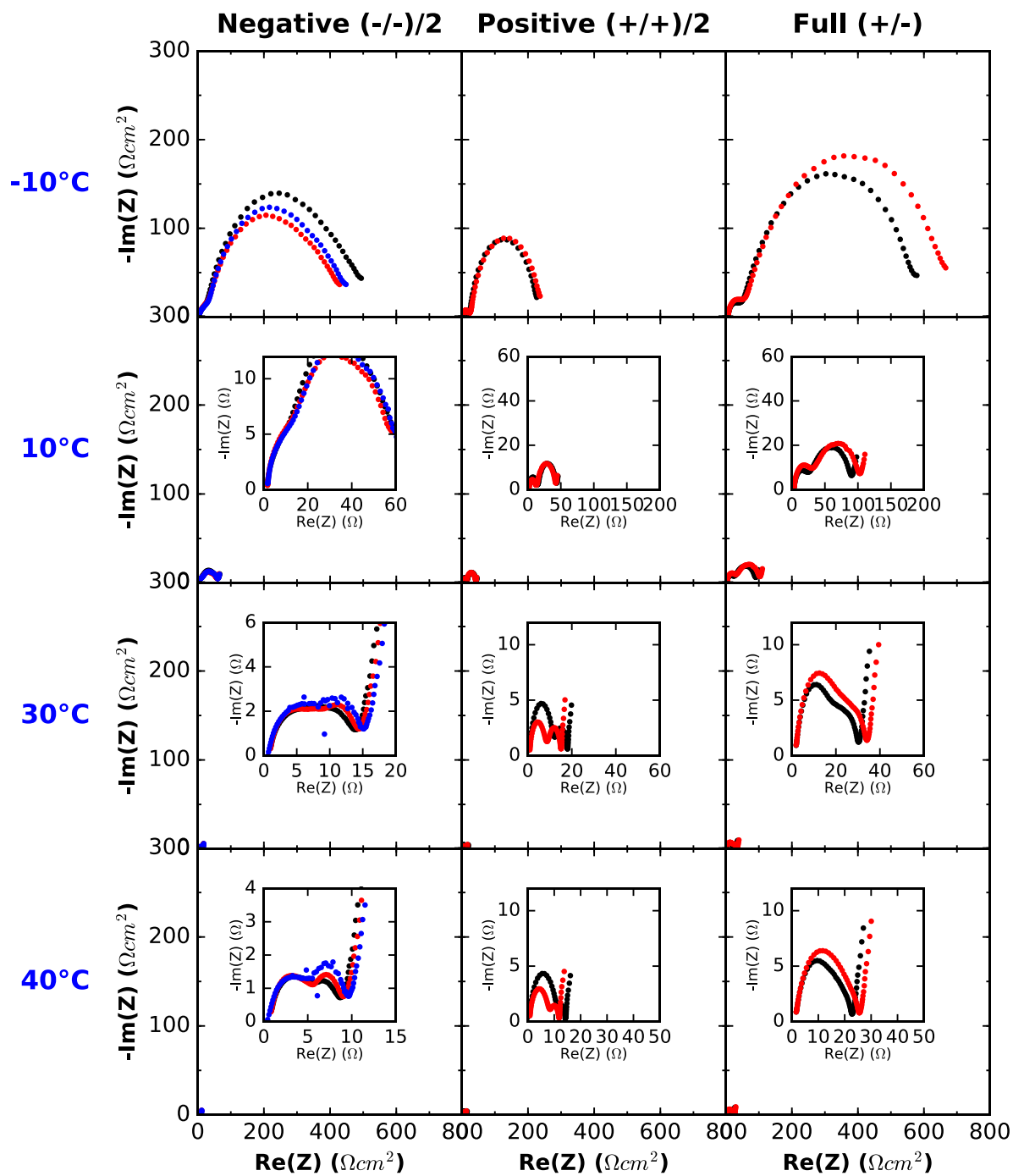
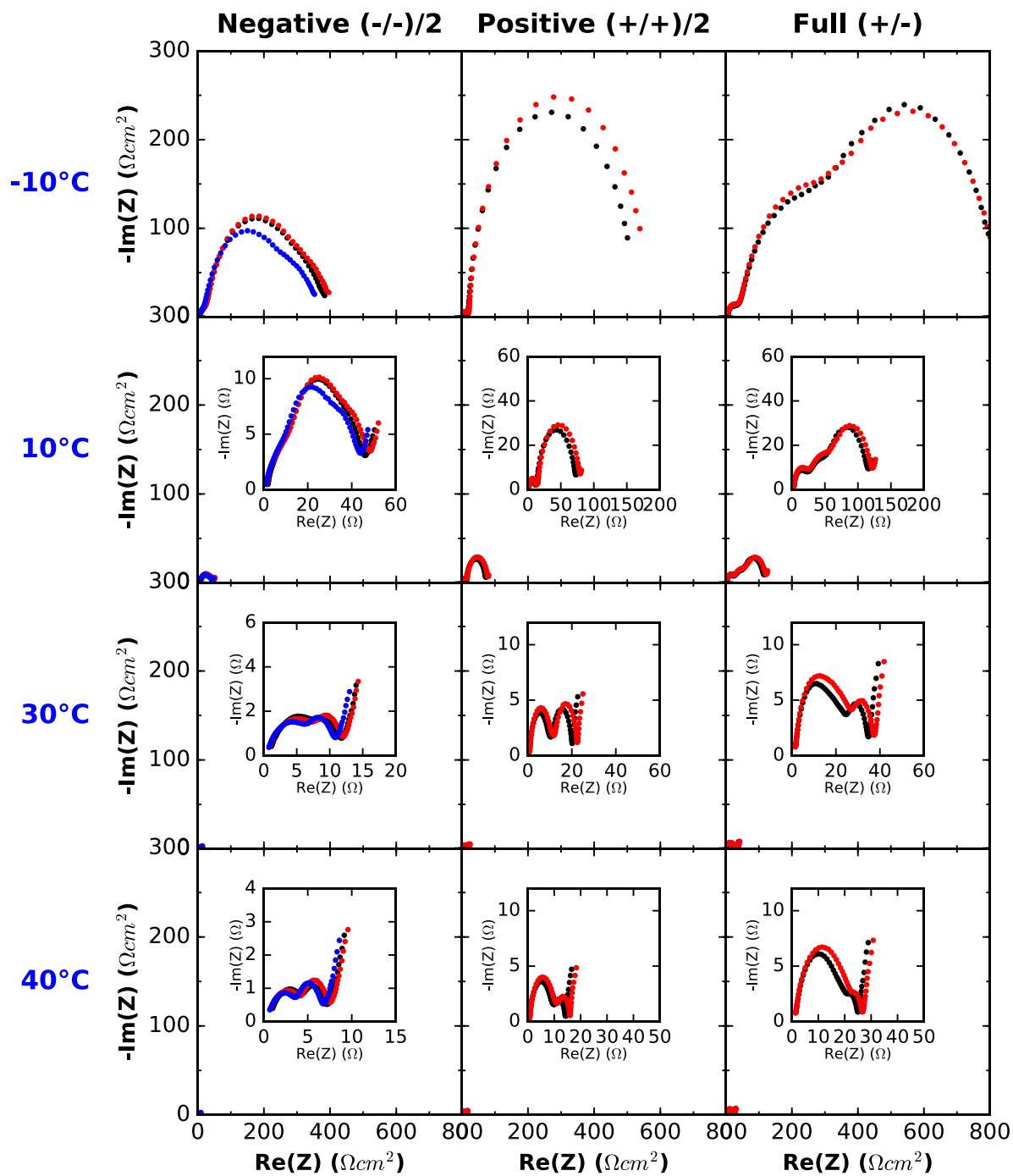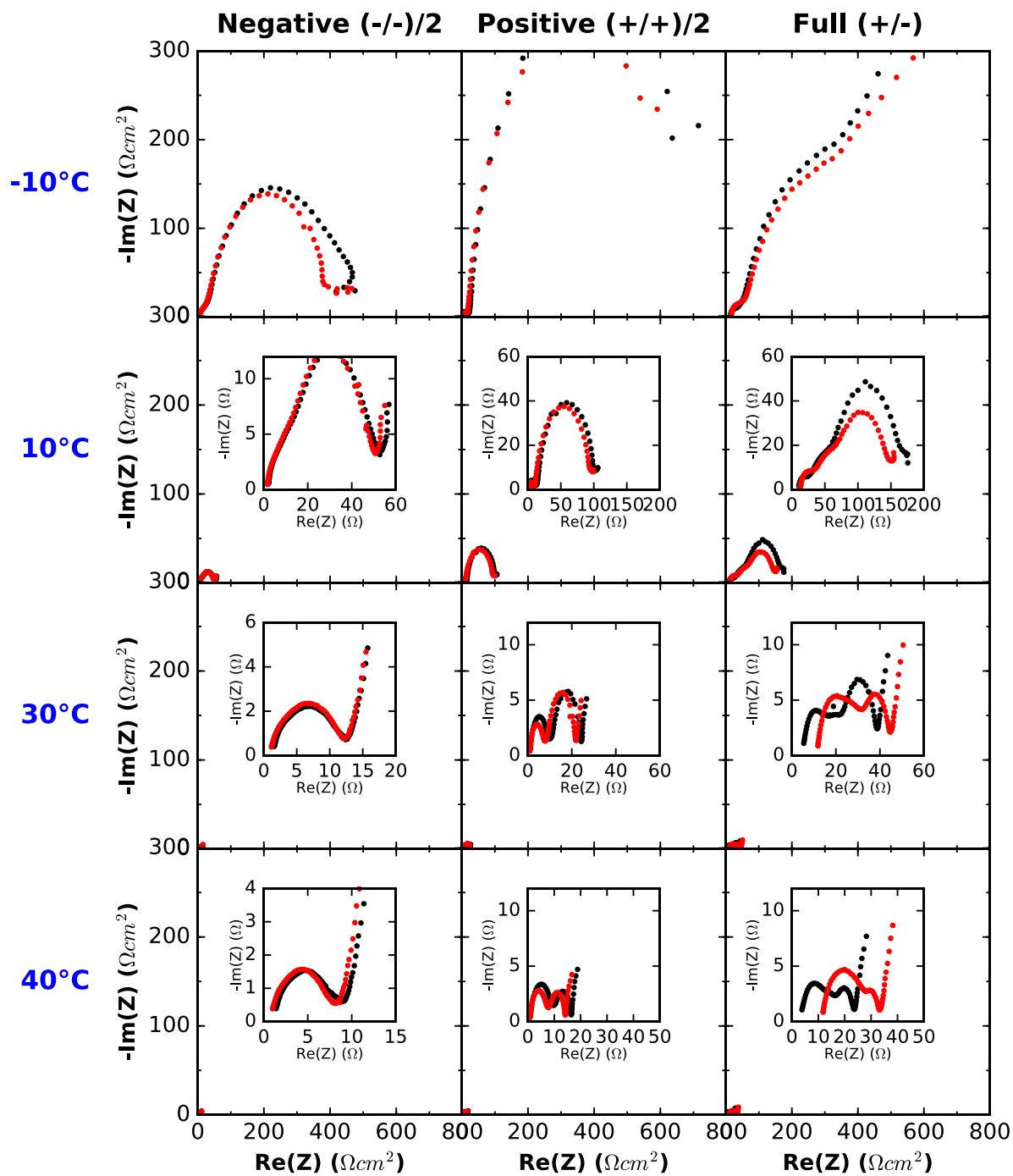Figure B.16: Control electrolyte; disassembled after formation; formed to 4.4 V and measured at 3.8 V.
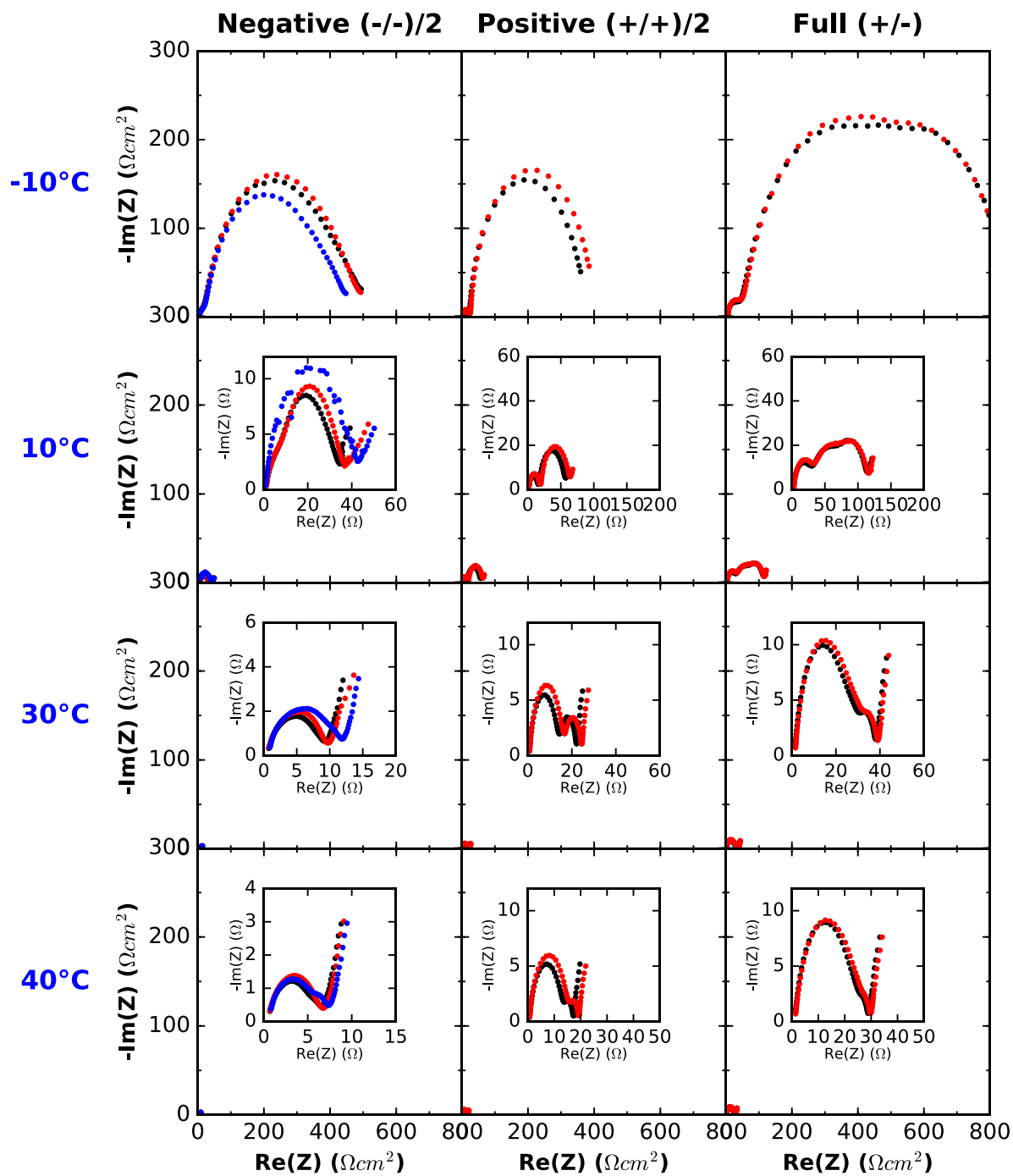
Figure B.17: Control + 2% VC electrolyte; disassembled after formation; formed to 4.2 V and measured at 4.2 V.
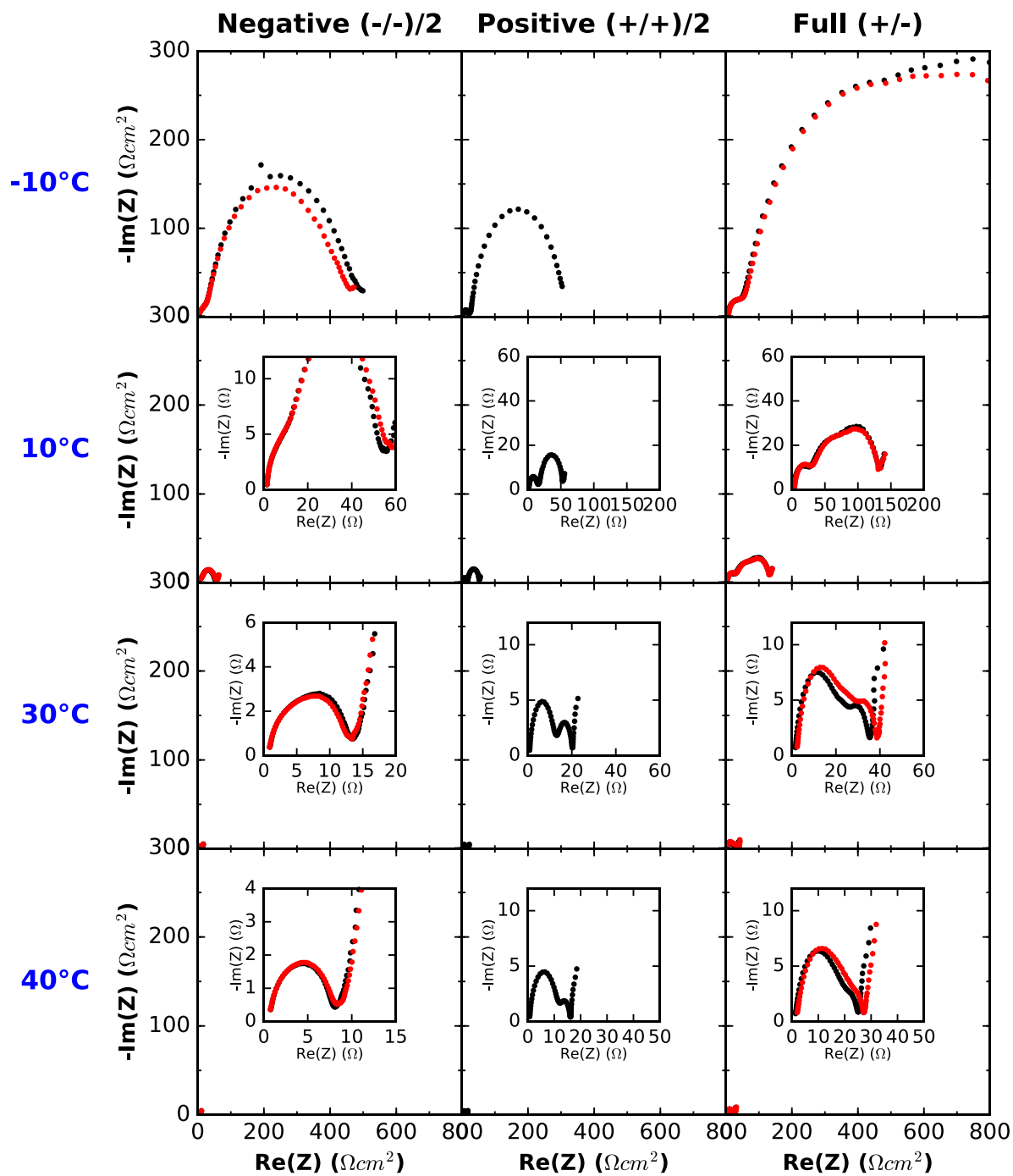
Figure B.18: Control + 2% VC electrolyte; disassembled after formation; formed to 4.2 V and measured at 3.8 V.

Figure B.19: Control + 2% VC electrolyte; disassembled after formation; formed to 4.4 V and measured at 4.4 V.

142

Figure B.20: Control + 2% VC electrolyte; disassembled after formation; formed to 4.4 V and measured at 3.8 V.
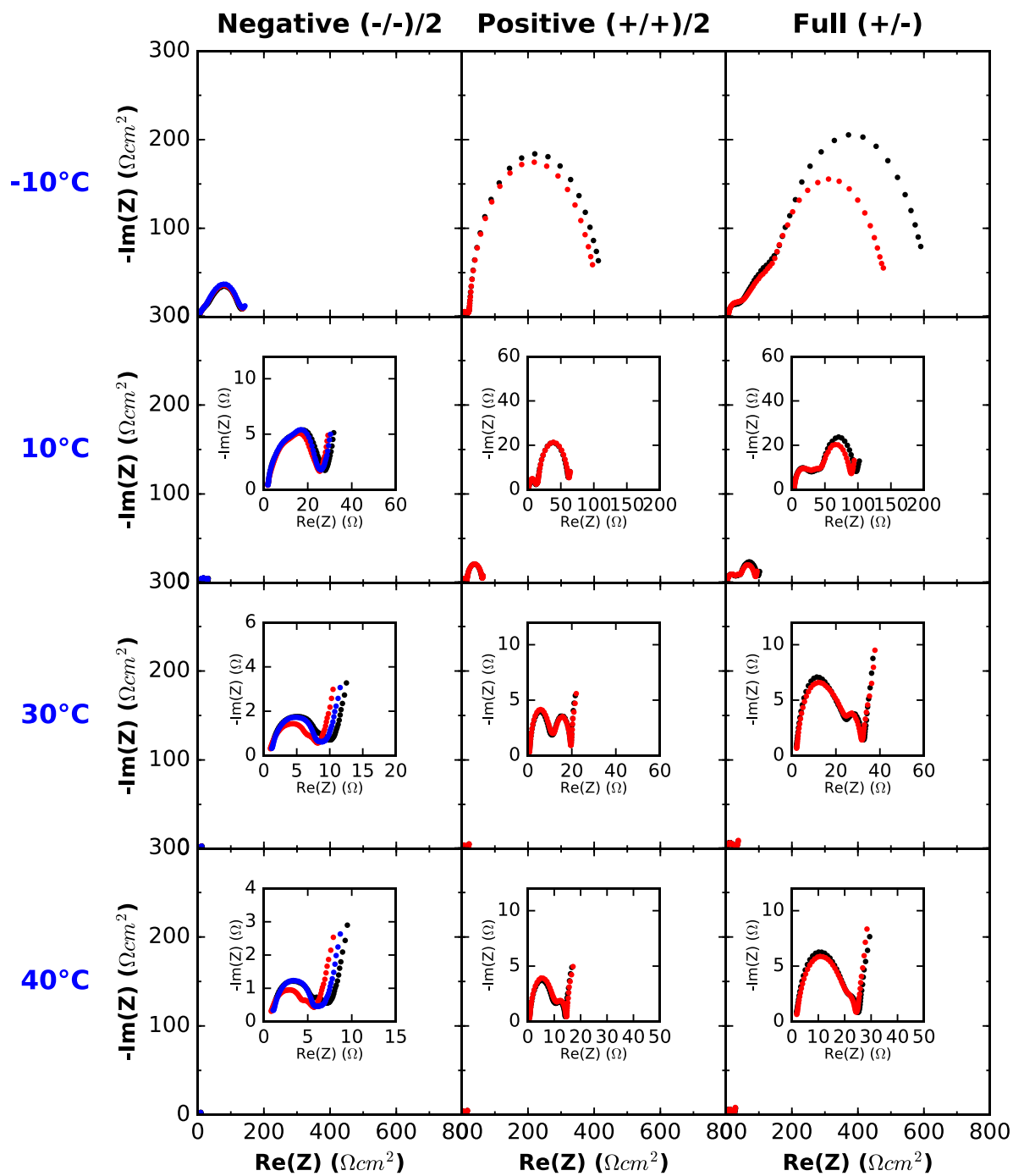
Figure B.21: Control + 1% LFO electrolyte; disassembled after formation; formed to 4.2 V and measured at 4.2 V.
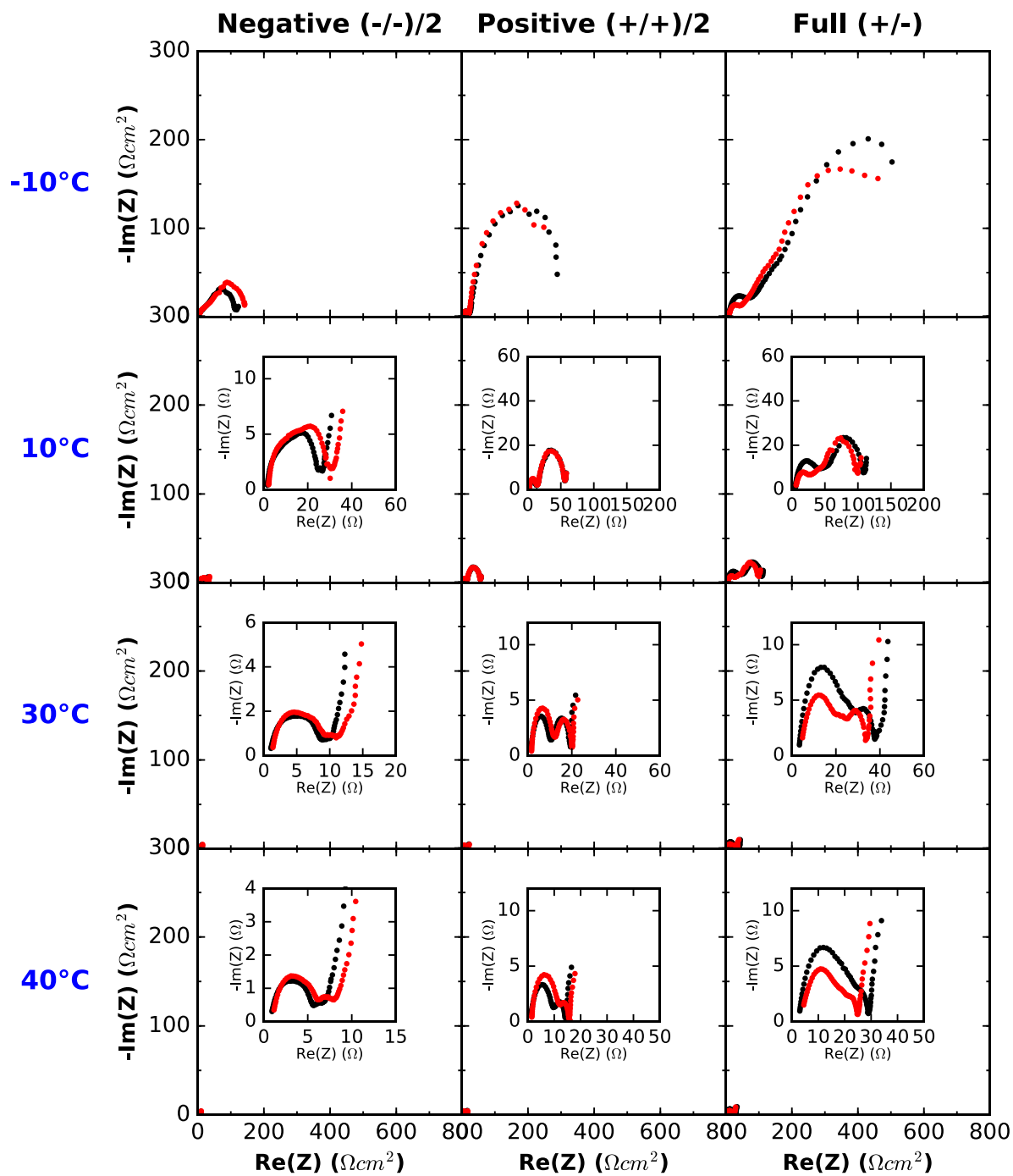
Figure B.22: Control + 1% LFO electrolyte; disassembled after formation; formed to 4.2 V and measured at 3.8 V.
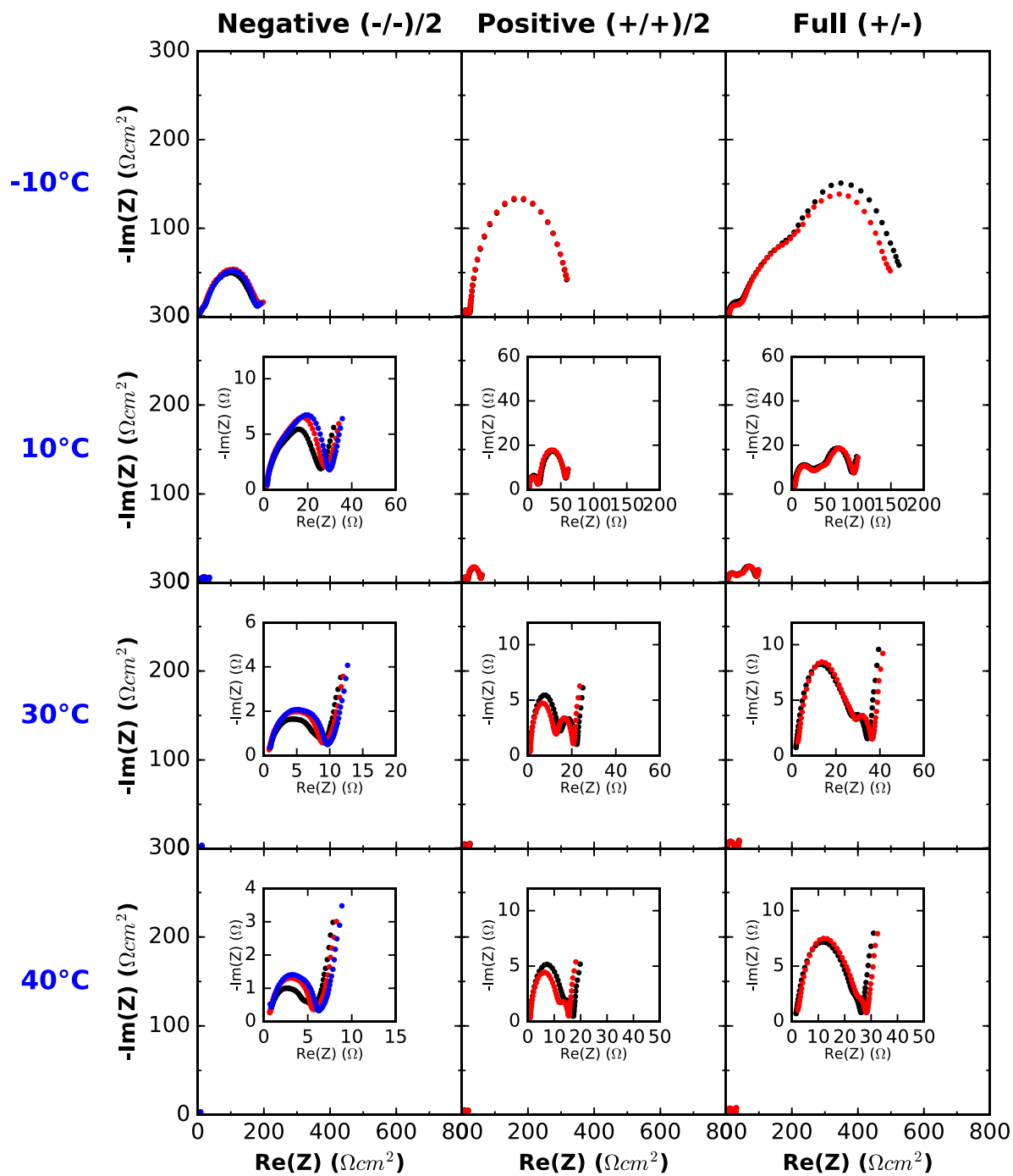
Figure B.23: Control + 1% LFO electrolyte; disassembled after formation; formed to 4.4 V and measured at 4.4 V.
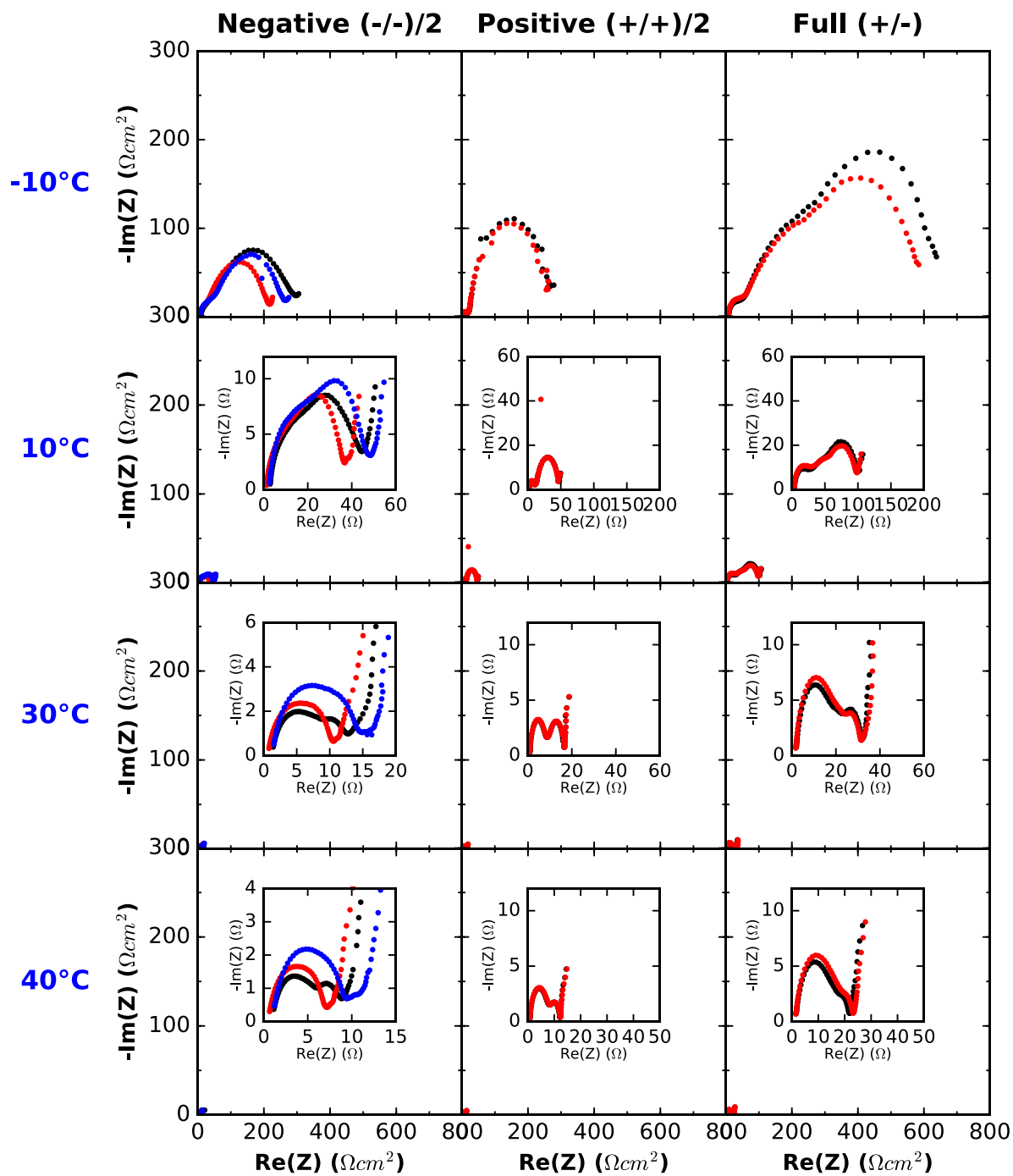
Figure B.24: Control + 1% LFO electrolyte; disassembled after formation; formed to 4.4 V and measured at 4.2 V.
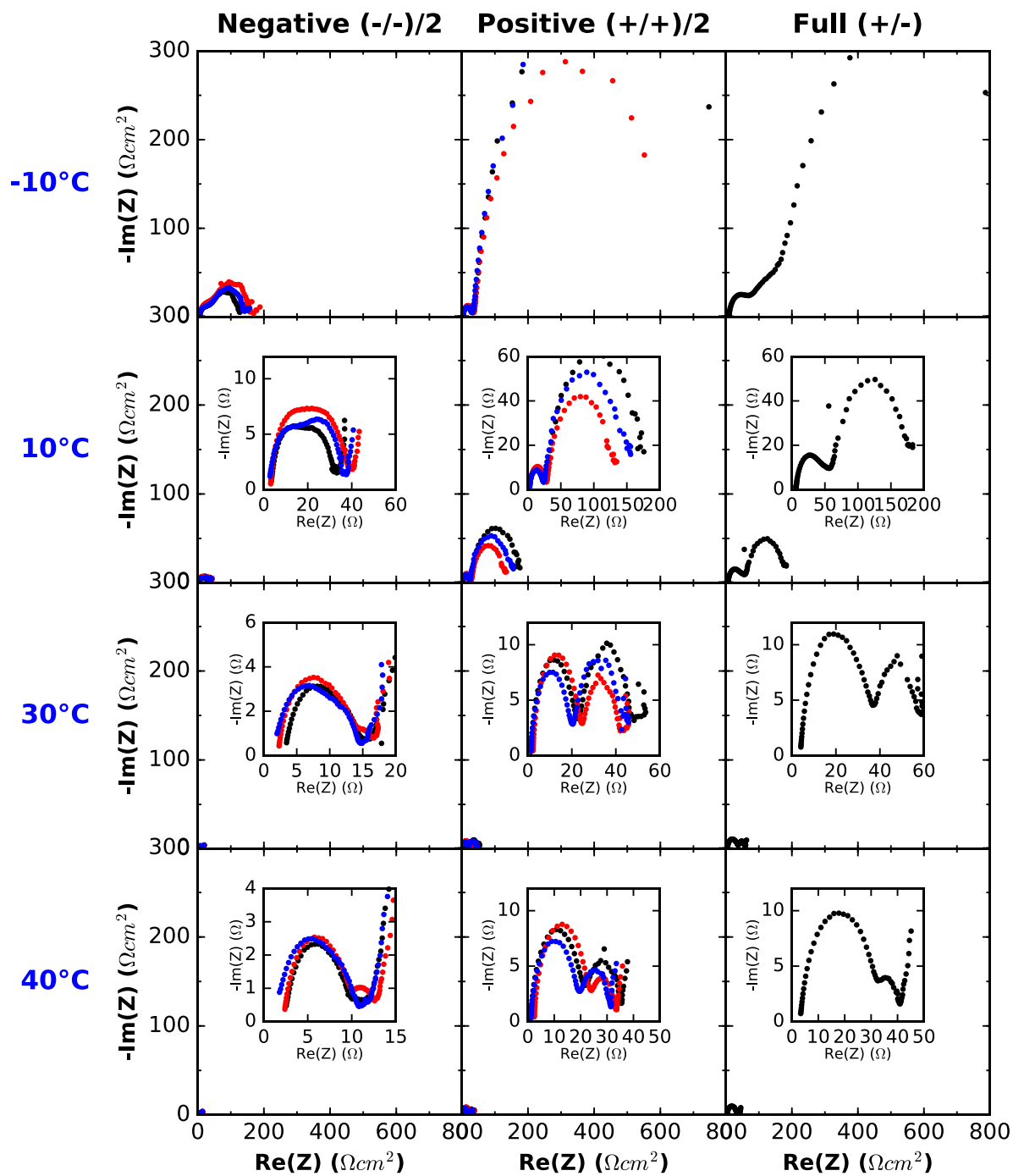
147

Figure B.25: Control electrolyte; disassembled after 722 cycles; formed to 4.2 V and measured at 3.8 V.
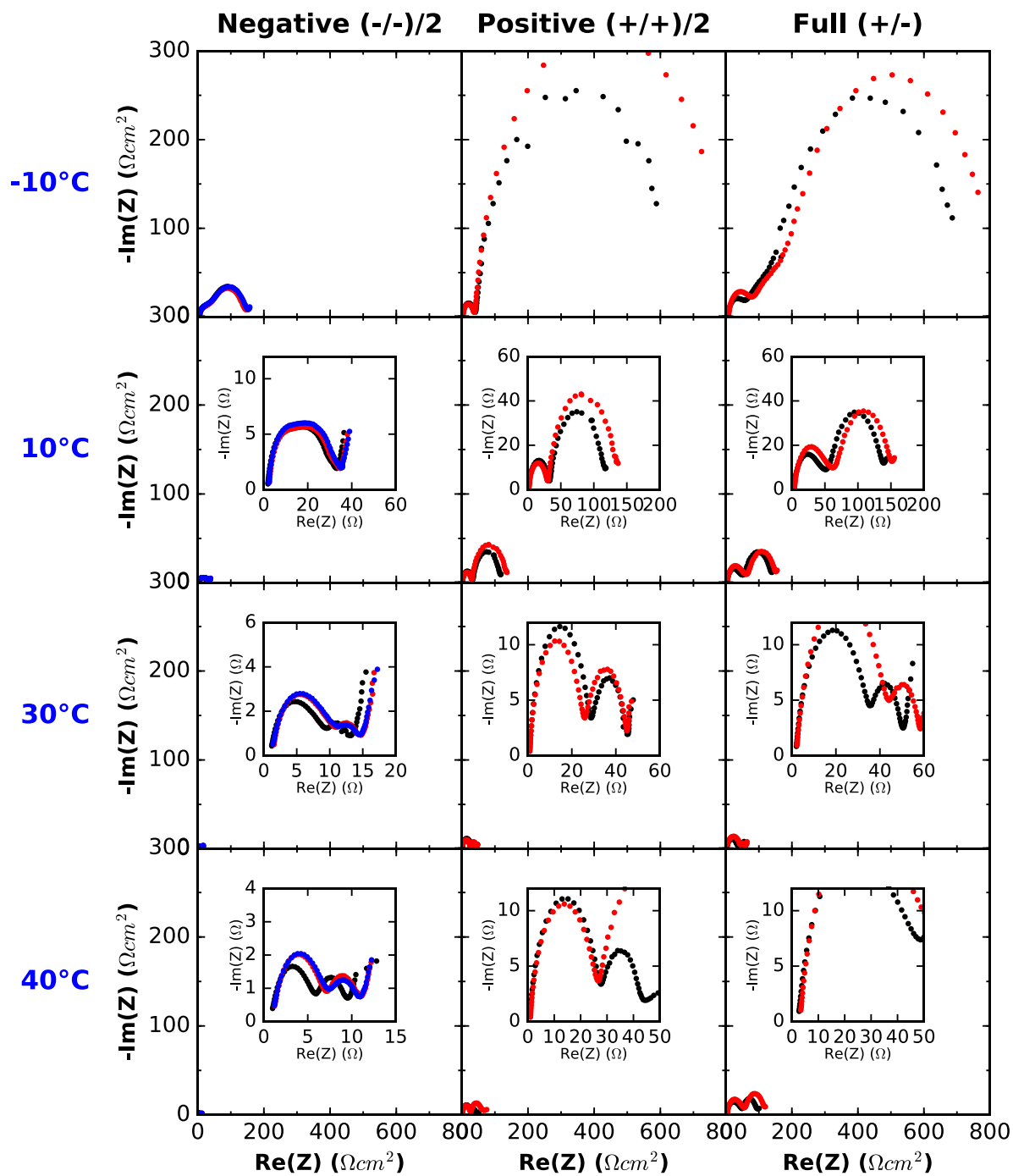
Figure B.26: Control electrolyte; disassembled after 322 cycles; formed to 4.4 V and measured at 3.8 V. (Note: temperature box was not at 40ºC for all (+/+) and (+/−) cells in the last row.)
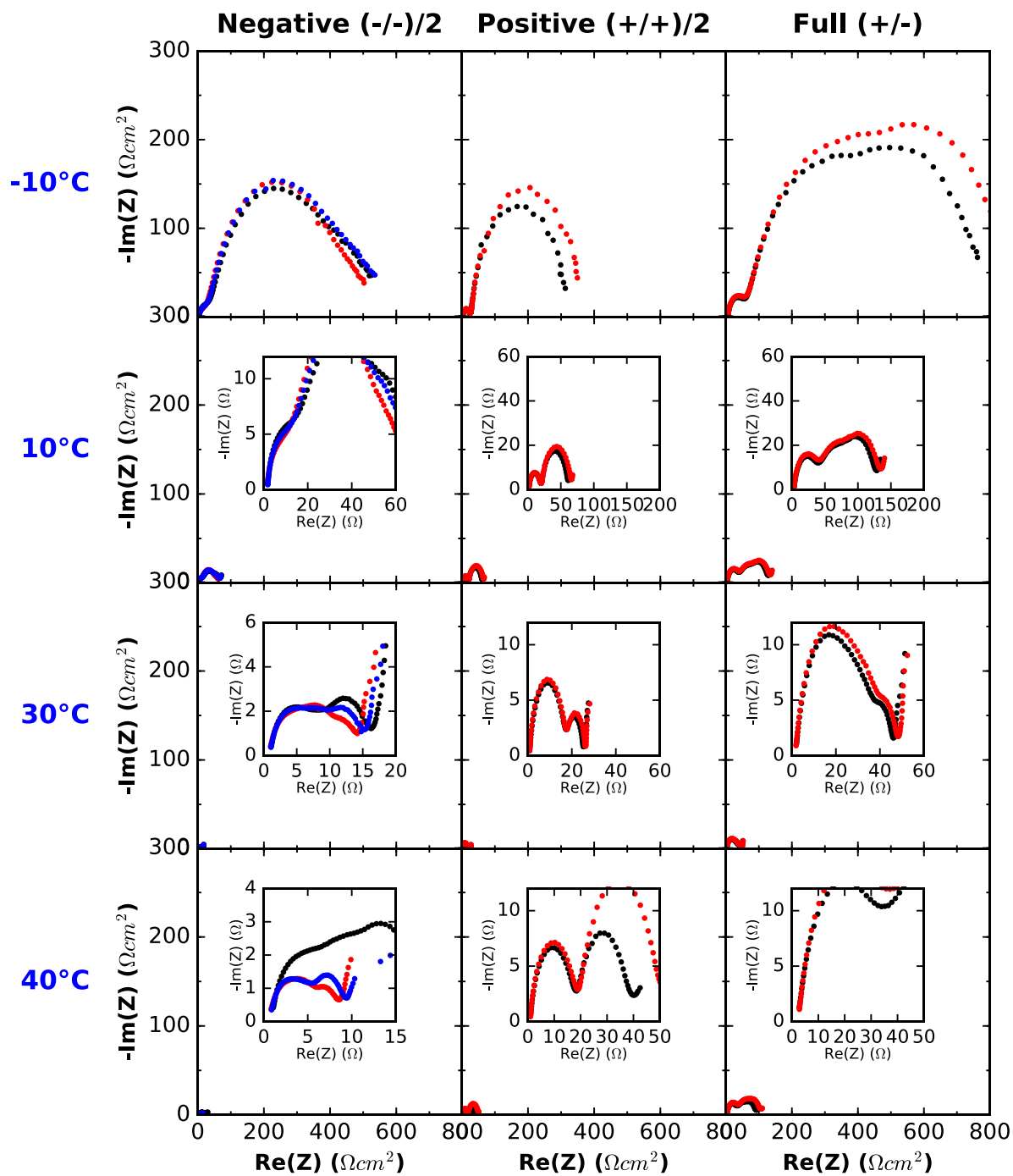
Figure B.27: Control + 2% VC electrolyte; disassembled after 392 cycles; formed to 4.2 V and measured at 3.8 V. (Note: temperature box was not at 40ºC for all cells in the last row.)

150

Figure B.28: Control + 2% VC electrolyte; disassembled after 677 cycles; formed to 4.2 V and measured at 3.8 V.

Figure B.29: Control + 2% VC electrolyte; disassembled after 385 cycles; formed to 4.4 V and measured at 3.8 V.

Figure B.30: Control + 1% LFO electrolyte; disassembled after 383 cycles; formed to 4.2 V and measured at 3.8 V.

Figure B.31: Control + 1% LFO electrolyte; disassembled after 683 cycles; formed to 4.2 V and measured at 3.8 V.
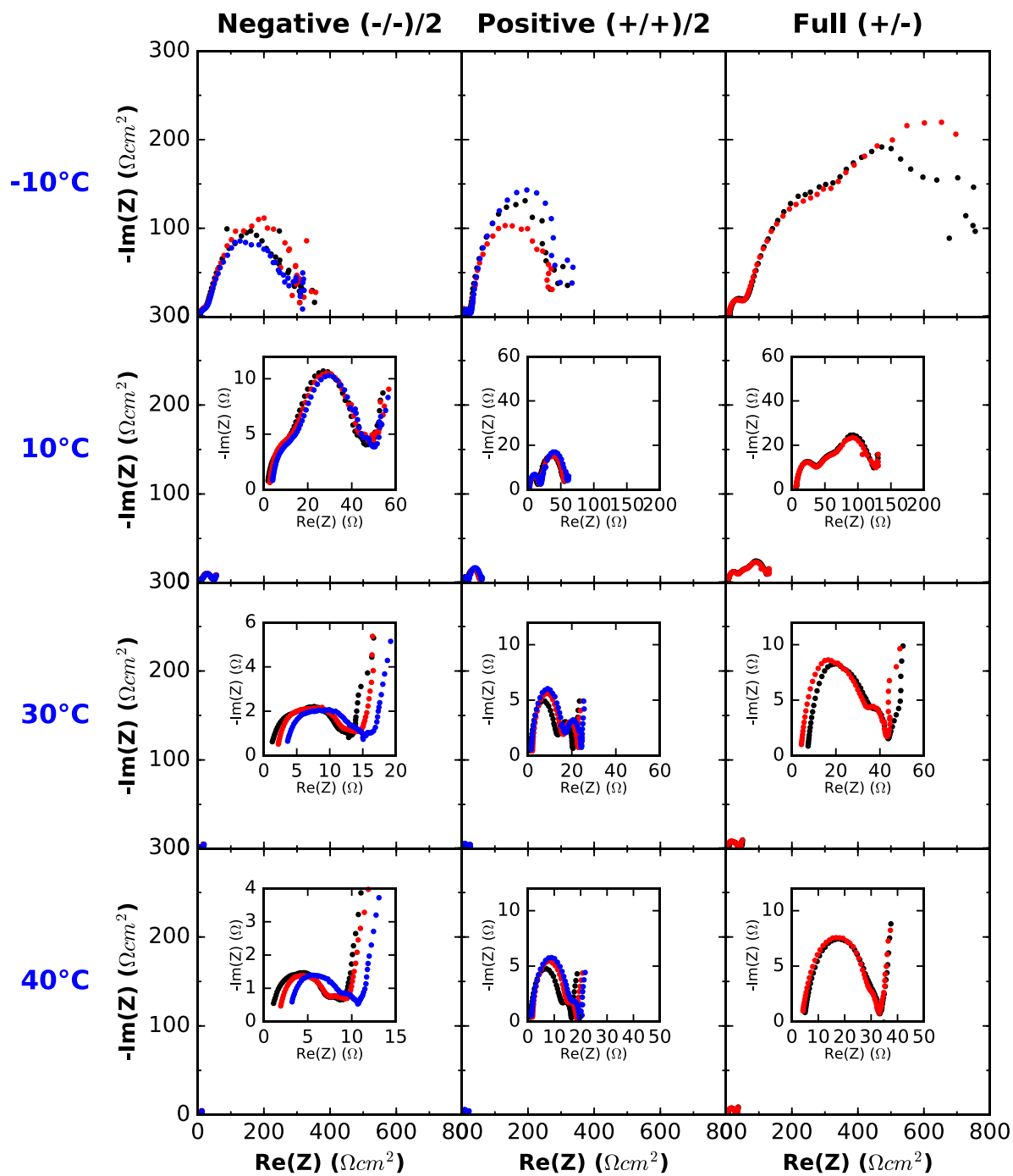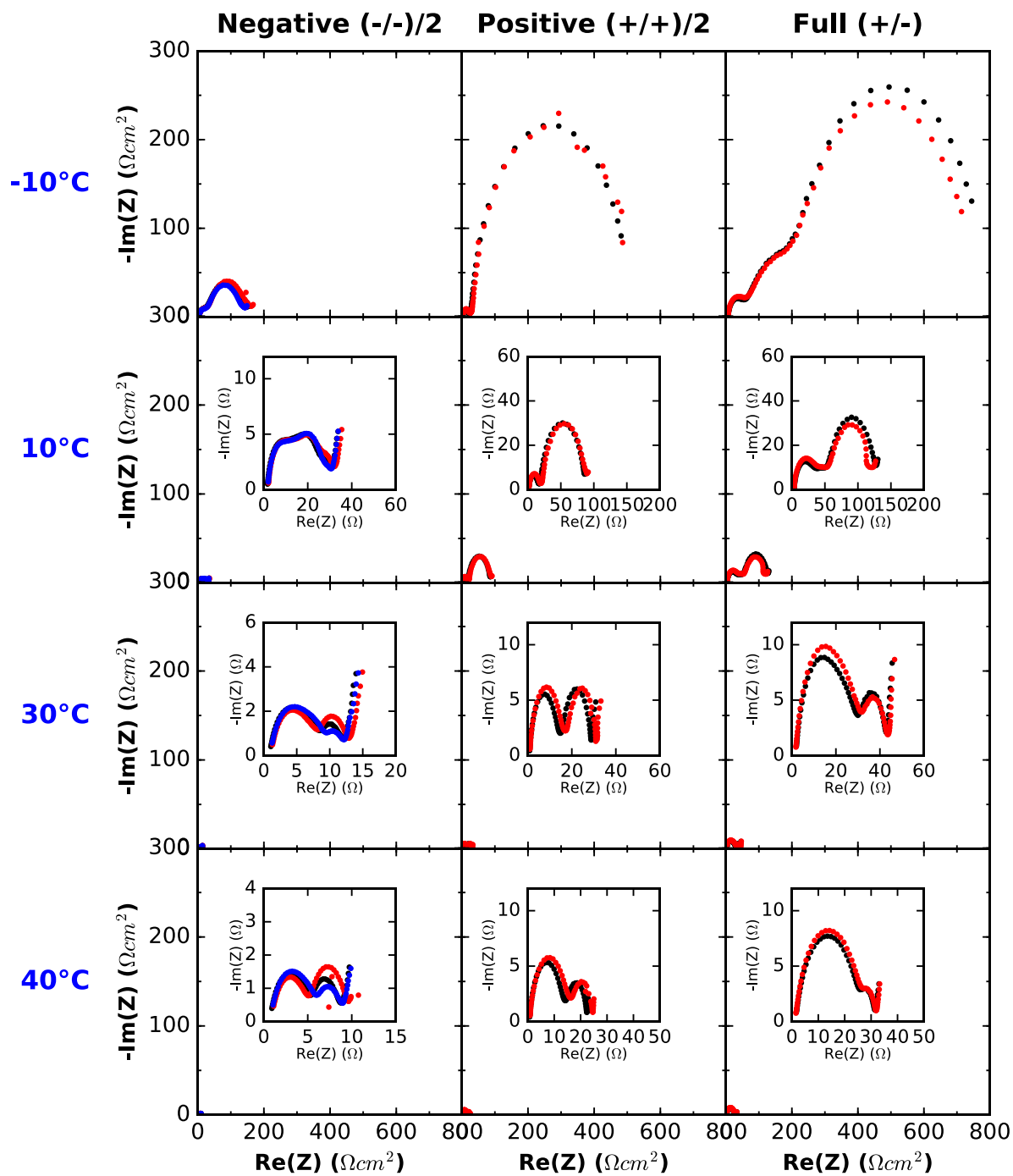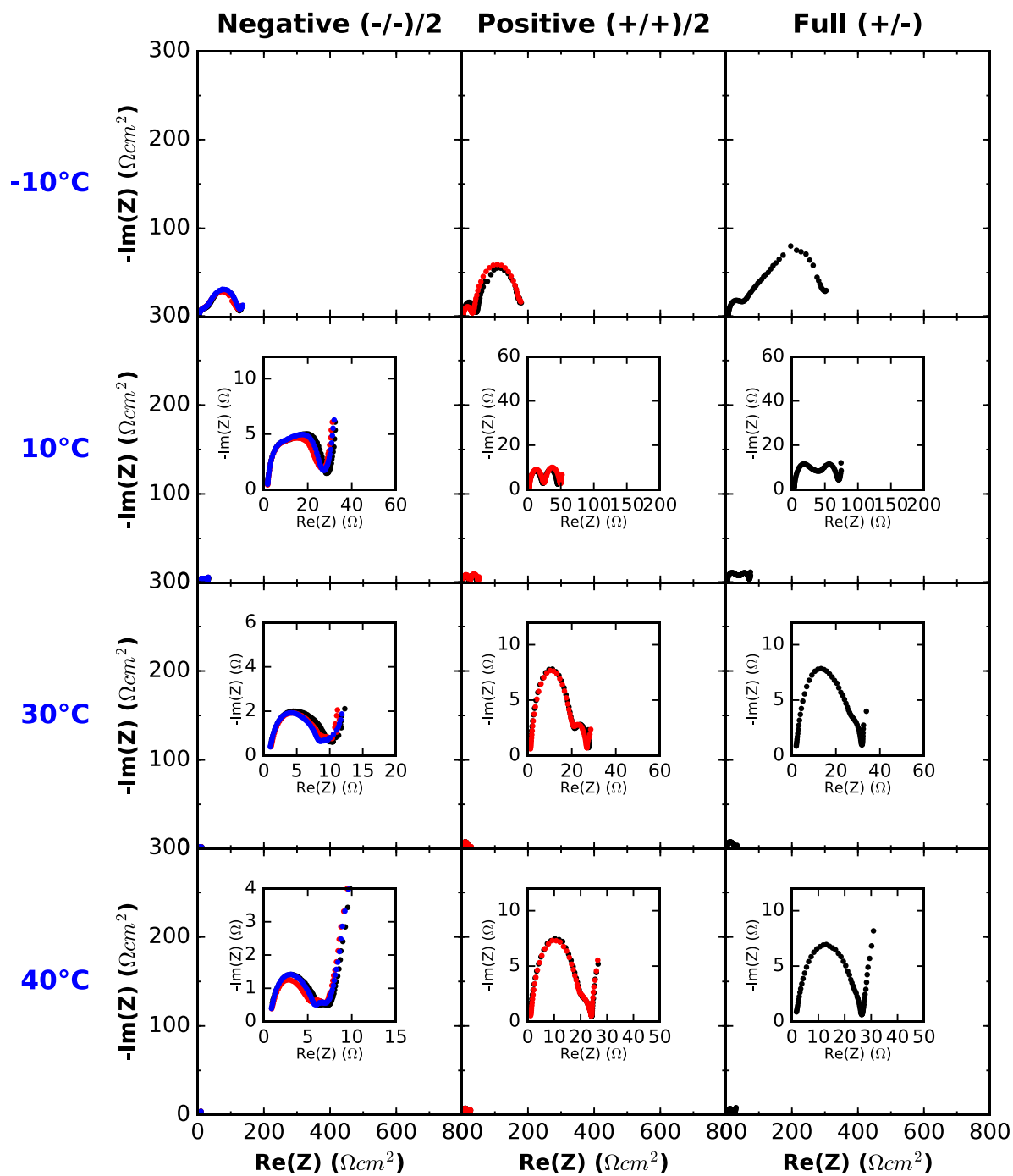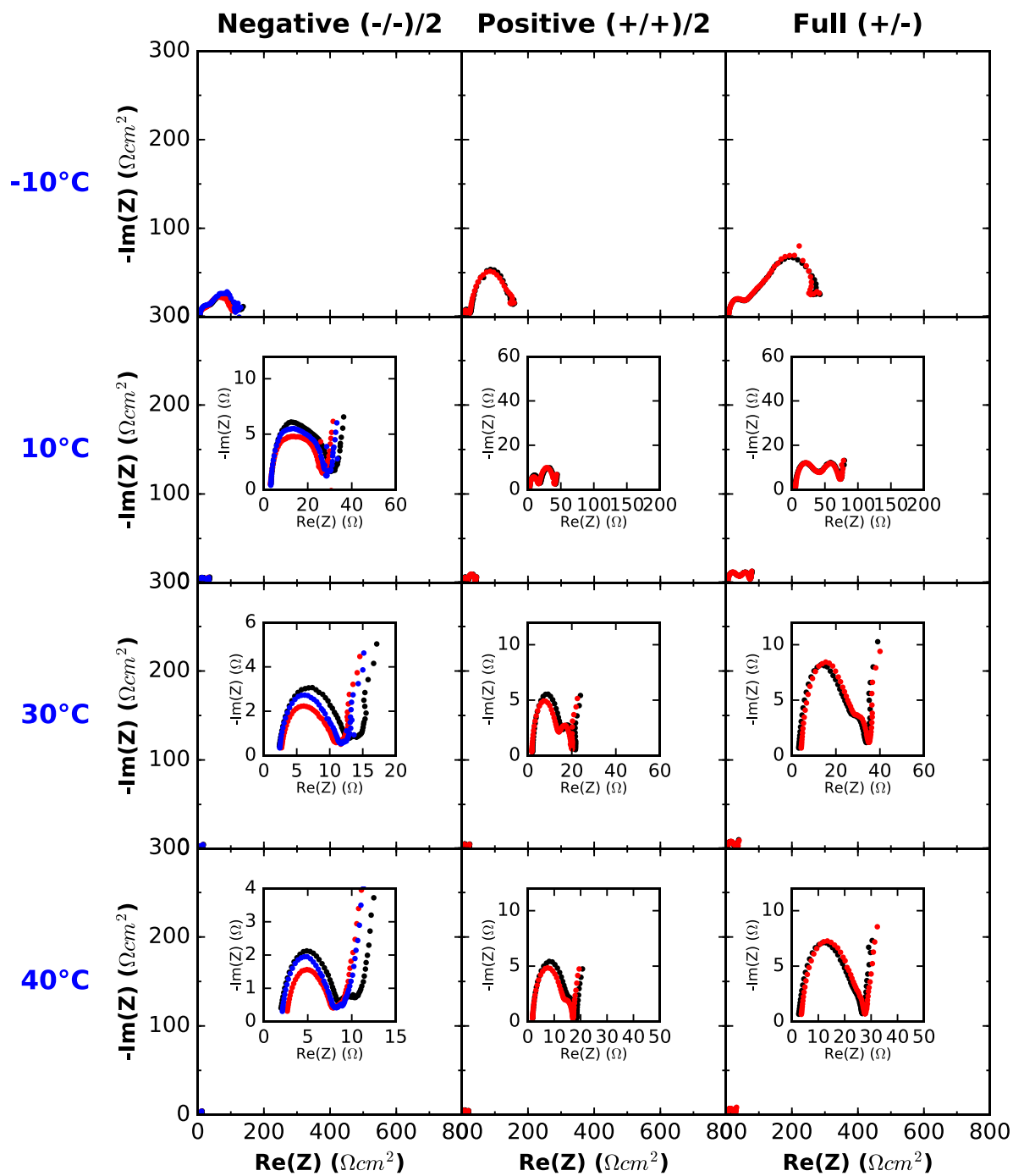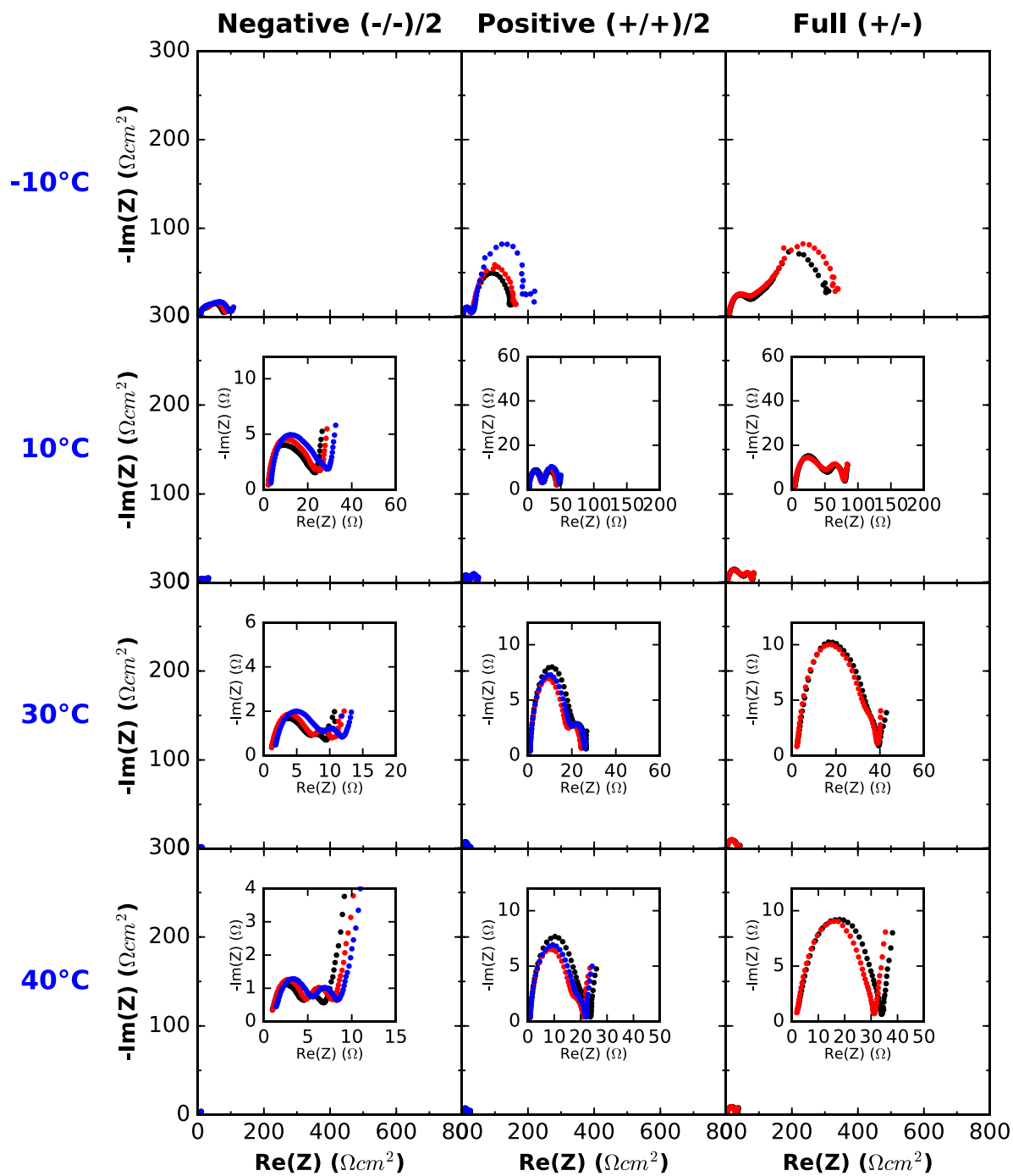
Figure B.32: Control + 1% LFO electrolyte; disassembled after 384 cycles; formed to 4.4 V and measured at 3.8 V.
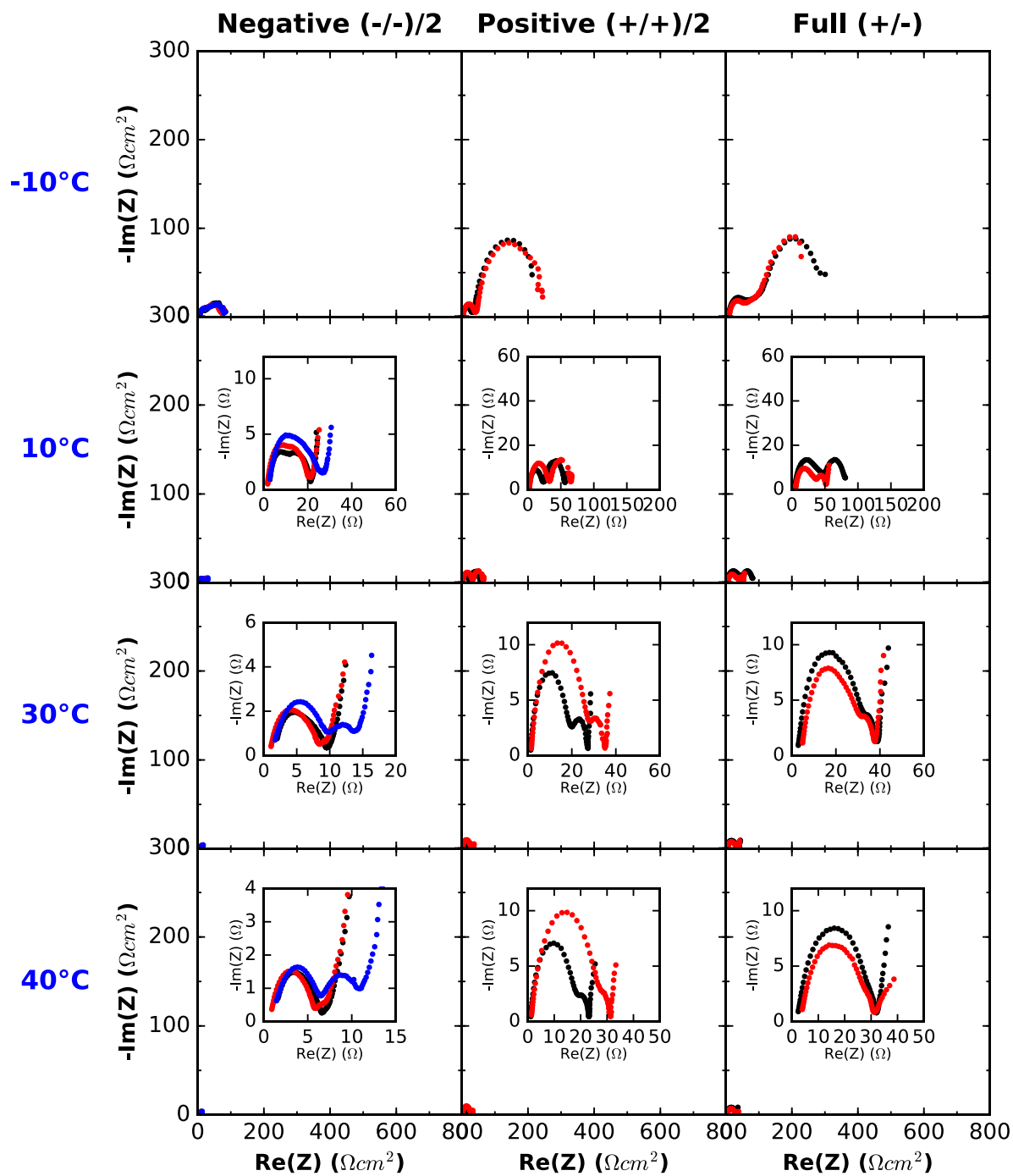
Figure B.33: Control + 1% LFO electrolyte; disassembled after 678 cycles; formed to 4.4 V and measured at 3.8 V.

References

1. Z. Chen and J. R. Dahn, *Electrochimica Acta*, **49**, 1079–1090 (2004).

2. T. Osaka, S. Nakade, M. Rajamäki, and T. Momma, *Journal of Power Sources*, **119–121**, 929–933 (2003).

3. S. F. Schuster, M. J. Brand, C. Campestrini, M. Gleissenberger, and A. Jossen, *Journal of Power Sources*, **305**, 191–199 (2016).

4. R. Spotnitz, *Journal of Power Sources*, **113**, 72–80 (2003).

5. I. Bloom et al., *Journal of Power Sources*, **124**, 538–550 (2003).

6. J. Dahn, G. M. Ehrlich, and D. Dought, in *Linden's Handbook of Batteries*, McGraw-Hill Publishing, New York, USA (2019).

7. S. S. Zhang, K. Xu, and T. R. Jow, *Journal of The Electrochemical Society*, **149**, A1521 (2002).

8. A. Wang, S. Kadam, H. Li, S. Shi, and Y. Qi, *npj Computational Materials*, **4**, 15 (2018).

9. L. Madec et al., *The Journal of Physical Chemistry C*, **118**, 29608–29622 (2014).

10. L. Madec et al., *J. Electrochem. Soc.*, **162**, A2635–A2645 (2015).

11. J. Xia, K. J. Nelson, Z. Lu, and J. R. Dahn, *Journal of Power Sources*, **329**, 387–397 (2016).

12. R. Wang, X. Li, Z. Wang, and H. Zhang, *Nano Energy*, **34**, 131–140 (2017).

13. Q. Q. Liu, R. Petibon, C. Y. Du, and J. R. Dahn, *Journal of The Electrochemical Society*, **164**, A1173–A1183 (2017).

14. K. J. Nelson, J. Xia, and J. R. Dahn, *J. Electrochem. Soc.*, **161**, A1884–A1889 (2014).

15. R. Petibon, E. C. Henry, J. C. Burns, N. N. Sinha, and J. R. Dahn, *J. Electrochem. Soc.*, **161**, A66–A74 (2014).

16. G. Yang et al., *RSC Advances*, **7**, 26052–26059 (2017).

17. S. J. An et al., *Carbon*, **105**, 52–76 (2016).

18. P. Verma, P. Maire, and P. Novák, *Electrochimica Acta*, **55**, 6332–6341 (2010).

19. K. Xu, *Chemical Reviews*, **104**, 4303–4418 (2004).

20. S. S. Zhang, K. Xu, and T. R. Jow, *Electrochimica Acta*, **51**, 1636–1640 (2006).

21. M. S. Whittingham, *Chemical Reviews*, **104**, 4271–4302 (2004).

22. J. R. Dahn, *J. Electrochem. Soc.*, **138**, 5 (1991).

23. J. Li et al., *Journal of The Electrochemical Society*, **164**, A1534–A1544 (2017).

24. J. E. Harlow et al., *J. Electrochem. Soc.*, **166**, A3031–A3044 (2019).

25. R. Amin and Y.-M. Chiang, *Journal of The Electrochemical Society*, **163**, A1512–A1517 (2016).

26. K. A. Seid et al., *Phys. Chem. Chem. Phys.*, **15**, 19790–19798 (2013).

27. K. Xu, *Chem. Rev.*, **114**, 11503–11618 (2014).

28. J. Li, H. Li, W. Stone, S. Glazier, and J. R. Dahn, *J. Electrochem. Soc.*, **165**, A626–A635 (2018).

29. J. C. Burns et al., *Journal of The Electrochemical Society*, **160**, A1451–A1456 (2013).

30. J. C. Burns et al., *J. Electrochem. Soc.*, **159**, A1105–A1113 (2012).

31. J. C. Burns et al., *J. Electrochem. Soc.*, **160**, A1668–A1674 (2013).

32. D. Aurbach et al., *Electrochimica Acta*, **47**, 1423–1439 (2002).

33. A. L. Michan et al., *Chem. Mater.*, **28**, 8149–8159 (2016).

34. M. Nie et al., *J. Electrochem. Soc.*, **162**, A7008–A7014 (2015).

35. Y. Qian et al., *Energy Storage Materials*, **20**, 208–215 (2019).

36. L. Ma et al., *J. Electrochem. Soc.*, **165**, A891–A899 (2018).

37. E. Peled, *J. Electrochem. Soc.*, **126**, 2047–2051 (1979).

38. M. Nie et al., *The Journal of Physical Chemistry C*, **117**, 1257–1267 (2013).

39. E. Peled and S. Menkin, *Journal of The Electrochemical Society*, **164**, A1703–A1719 (2017).

40. R. Fong, U. von Sacken, and J. R. Dahn, *J. Electrochem. Soc.*, **137**, 2009–2013 (1990).

41. Y. Qian et al., *Journal of Power Sources*, **329**, 31–40 (2016).

42. L. E. Ouatani et al., *J. Electrochem. Soc.*, **156**, A103–A113 (2009).

43. H. Ota, Y. Sakata, A. Inoue, and S. Yamaguchi, *J. Electrochem. Soc.*, **151**, A1659–A1669 (2004).

44. R. I. R. Blyth et al., *Applied Surface Science*, **167**, 99–106 (2000).

45. S. Malmgren et al., *Electrochimica Acta*, **97**, 23–32 (2013).

46. J. C. Burns et al., *Journal of The Electrochemical Society*, **158**, A1417 (2011).

47. J. Landesfeind, J. Hattendorff, A. Ehrl, W. A. Wall, and H. A. Gasteiger, *Journal of The Electrochemical Society*, **163**, A1373–A1387 (2016).

48. N. N. Sinha, J. C. Burns, R. J. Sanderson, and J. Dahn, *J. Electrochem. Soc.*, **158**, A1400–A1403 (2011).

49. J. R. MacDonald, *Impedance Spectroscopy: Emphasizing Solid Materials and Systems*, John Wiley & Sons, (1987).

50. M. E. Orazem and B. Tribollet, *Electrochemical Impedance Spectroscopy*, John Wiley & Sons, Hoboken, N.J., (2008).

51. A. Lasia, *Electrochemical impedance spectroscopy and its applications*, p. 367, Springer, New York, (2014).

52. C. Ho, I. D. Raistrick, and R. A. Huggins, *J. Electrochem. Soc.*, **127**, 343–350 (1980).

53. J.-M. Atebamba, J. Moskon, S. Pejovnik, and M. Gaberscek, *J. Electrochem. Soc.*, **157**, A1218–A1228 (2010).

54. S. Buteau, D. C. Dahn, and J. R. Dahn, *Journal of The Electrochemical Society*, **165**, A228–A234 (2018).

55. M. Gaberscek, J. Moskon, B. Erjavec, R. Dominko, and J. Jamnik, *Electrochemical and Solid-State Letters*, **11**, A170 (2008).

56. Q.-C. Zhuang, X.-Y. Qiu, S.-D. Xu, Y.-H. Qiang, and S.-G. Su, in *Lithium Ion Batteries - New Developments*, I. Belharouak, Editor, InTech (2012).

57. B. Yann Liaw, *Solid State Ionics*, **175**, 835–839 (2004).

58. J. E. B. Randles, *Discussions of the Faraday Society*, **1**, 11 (1947).

59. N. Ogihara, Y. Itou, T. Sasaki, and Y. Takeuchi, *The Journal of Physical Chemistry C*, **119**, 4612–4619 (2015).

60. H. Nara, D. Mukoyama, R. Shimizu, T. Momma, and T. Osaka, *Journal of Power Sources*, **409**, 139–147 (2019).

61. J. Landesfeind, D. Pritzl, and H. A. Gasteiger, *Journal of The Electrochemical Society*, **164**, A1773–A1783 (2017).

62. R. Petibon et al., *J. Electrochem. Soc.*, **160**, A117–A124 (2013).

63. W. Waag, S. Käbitz, and D. U. Sauer, *Applied Energy*, **102**, 885–897 (2013).

64. K. J. Laidler, *Journal of Chemical Education*, **61**, 494 (1984).

65. C. H. Hsu and F. Mansfeld, *CORROSION*, **57**, 747–748 (2001).

66. D. Halliday, R. Resnick, and J. Walker, *Fundamentals of Physics*, 9th ed., Wiley, Hoboken, N.J., (2010).

67. V. J. Ovejas and A. Cuadras, *Batteries*, **4**, 43 (2018).

68. J. C. Vickerman and I. S. Gilmore, Eds., *Surface analysis: the principal techniques*, 2nd ed., p. 666, Wiley, Chichester, U.K, (2009).

69. R. Smart, S. McIntyre, and I. Bello, 86.

70. J. Xia et al., *Journal of Power Sources*, **295**, 203–211 (2015).

71. R. Crowe and J. P. S. Badyal, 2.

72. S. Zhang et al., *Chinese Physics B*, **24**, 078201 (2015).

73. L. Ellis, thesis, Dalhousie University, Halifax, Nova Scotia (2018).

74. https://srdata.nist.gov/xps/main_search_menu.aspx.

75. https://xpssimplified.com/.

76. H. M. Dahn, A. J. Smith, J. C. Burns, D. A. Stevens, and J. R. Dahn, *J. Electrochem. Soc.*, **159**, A1405–A1409 (2012).

77. J. A. Gilbert et al., *J. Electrochem. Soc.*, **164**, A6054–A6065 (2017).

78. J. Hong, C. Wang, and U. Kasavajjula, *Journal of Power Sources*, **162**, 1289–1296 (2006).

79. H. C. Shin, W. I. Cho, and H. Jang, *Journal of Power Sources*, **159**, 1383–1388 (2006).

80. M. Itagaki et al., *Electrochimica Acta*, **51**, 1629–1635 (2006).

81. D. Andre et al., *Journal of Power Sources*, **196**, 5334–5341 (2011).

82. J. Illig et al., *J. Electrochem. Soc.*, **159**, A952–A960 (2012).

83. N. Ogihara et al., *Journal of The Electrochemical Society*, **159**, A1034–A1039 (2012).

84. D. J. Xiong, T. Hynes, and J. R. Dahn, *J. Electrochem. Soc.*, **164**, A2089–A2100 (2017).

85. Q. Q. Liu, L. Ma, C. Y. Du, and J. R. Dahn, *Electrochimica Acta*, **263**, 237–248 (2018).

86. G. V. Zhuang, K. Xu, H. Yang, T. R. Jow, and P. N. Ross, *The Journal of Physical Chemistry B*, **109**, 17567–17573 (2005).

87. Z.-M. Dang, Y.-H. Lin, and C.-W. Nan, *Advanced Materials*, **15**, 1625–1629 (2003).

88. R. Gregorio and E. M. Ueno, *Journal of Materials Science*, **34**, 4489–4500 (1999).

89. A. J. Smith, J. C. Burns, D. Xiong, and J. R. Dahn, *J. Electrochem. Soc.*, **158**, A1136–A1142 (2011).

90. K. J. Nelson, D. W. Abarbanel, J. Xia, Z. Lu, and J. R. Dahn, *J. Electrochem. Soc.*, **163**, A272–A280 (2016).

91. L. M. Thompson et al., *J. Electrochem. Soc.*, **165**, A2732–A2740 (2018).

92. L. Ma, J. Xia, and J. R. Dahn, *Journal of The Electrochemical Society*, **161**, A2250–A2254 (2014).

93. K. Nelson, thesis, Dalhousie University, Halifax, Nova Scotia (2017).

94. S. Komaba, T. Ozeki, and K. Okushi, *Journal of Power Sources*, **189**, 197–203 (2009).

95. S. Xiong, K. Xie, Y. Diao, and X. Hong, *Journal of Power Sources*, **246**, 840–845 (2014).

96. S.-H. Lee et al., *Journal of Power Sources*, **247**, 307–313 (2014).

97. S. Komaba et al., *J. Electrochem. Soc.*, **152**, A937–A946 (2005).

98. N. Dupré et al., *J. Electrochem. Soc.*, **156**, C180–C185 (2009).

99. K. U. Schwenke, S. Solchenbach, J. Demeaux, B. L. Lucht, and H. A. Gasteiger, *J. Electrochem. Soc.*, **166**, A2035–A2047 (2019).

100. D. J. Xiong et al., *Journal of The Electrochemical Society*, **163**, A3069–A3077 (2016).